RESEARCH ON EFFECTIVE LENGTH FACTOR OF TOWER COLUMN LENGTHWISE BUCKLING IN STEEL TRUSS BRIDGE STIFFENED WITH RIGID CABLES

* S.Z. Liu[1,2], Y.J. Liu[1], J.G. Zhang[1] and W.Q. Yao[1]

[1] Key Laboratory for Bridge and Tunnel of Shanxi Province, Chang'an University, Nan Er Huan Zhong Duan, Xi'an, 710064, China

[2] School of Transportation and Logistics Engineering, Taiyuan University of Science and Technology, Taiyuan, 030024, China

* Email: lszll888@sina.com

KEYWORDS

Bridge engineering, tower column, theoretical analysis, effective length factor, steel truss bridge stiffened with rigid cables, stability, finite element method.

ABSTRACT

According to mechanical characters of tower column of steel truss bridge stiffened with rigid cables, simplified calculation model of tower column lengthwise buckling was set up by introducing equivalent springs, then stability characteristic equation for tower column was derived by using neutral equilibrium method. Based on a steel truss bridge stiffened with rigid cables-Dongjiang Bridge, 3-D and 2-D (single truss structure) finite element models of Dongjiang Bridge were established by FEM software. Stiffness coefficients of equivalent springs were obtained, and effective length factor μ of tower column lengthwise buckling was determined. The influences of different stiffness coefficient values of equivalent springs on μ were compared, and the reasonable range of effective length factor μ of tower column lengthwise buckling as found. The result shows that the influences of lateral bracing and the spatial effect on tower column can be ignored when analyzing lengthwise stability of tower column in finished stage. Change of lateral restraint stiffness (k_{TH}) at the upper end of tower column in wide range has little influence on μ. The rotating restraint stiffness (k_{BZ}) at the bottom end of tower column has great influence on μ, and μ is decreased with the increase of k_{BZ}. The rotating restraint stiffness (k_{TZ}) at the upper end of tower column has significant influence on μ, and μ is reduced most effectively with the increase of k_{TZ}. In addition, the rational ranges for effective length factor μ of tower column in this kind of steel truss bridge are found to be 0.65～0.8.

INTRODUCTION

With rapid development of analysis and construction technology for bridges at home and abroad, all kinds of new bridge structure are constantly emerging. Steel truss bridge stiffened with rigid cables, which has the mechanical characters of self-anchored suspension bridge and variable cross-section continuous steel truss bridge, not only overcomes the shortcomings of traditional suspension bridge with low stiffness and

poor stability, but also inherited the advantage of steel truss suspension bridge with low building height, being suitable for multi-layer lane layout and graceful shape[1]. Therefore, this kind of bridge has broad application prospects in city bridge construction of our country.

Steel truss bridge stiffened with rigid cables, which is the spatial stress system made up of steel main truss, rigid cables (stiffening string) and tower columns (portal frame), is novel in structural type and complicated in mechanical behaviour, and tower columns are significant load-bearing members. Under the dead load and live load, tower column can bear great pressure. When the pressure reaches a certain value, tower columns may produce buckling deformation and lose stability, which is directly related to bridge safety. At present, most of researcher focus their attention on stability of the tower column and main girder of suspension bridge and cable-stayed bridge all the world, and have put forward some simplified calculation formulas[2-6]. However, steel truss bridge stiffened with rigid cables is different from traditional suspension bridge or cable-stayed bridge, there is no basis about the calculation of tower column stability. In practical design, tower column is conservatively designed by tow-end articulated member or one-end cantilevered member, which will result in large length value and poor economy. Consequently, it's of great engineering significances to study effective length factor of tower column lengthwise buckling in steel truss bridge stiffened with rigid cables.

In this paper, taking a double-deck three main trusses steel bridge stiffened with rigid cables-Dongjiang Bridge, a simplified calculation model of tower column lengthwise buckling was set up by introducing equivalent springs, and effective length factor μ of tower column lengthwise buckling was determined jointly adopting analytical method and numerical simulation. The influence of related parameters (stiffness coefficients of equivalent springs) on effective length factor of tower column lengthwise buckling was analyzed and compared, and the rational ranges for effective length factor are found, which could provide reference for design and analysis of similar bridge.

OVERVIEW OF BRIDGE ENGINEERING

Dongjiang Bridge, the first double-deck highway bridge, which is a super large bridge across the south branch of the East River located at Dongguan-Shenzhen Expressway and Dongguan Ring Road, is a three main trusses continuous steel bridge stiffened with rigid cables[7-10]. The length of whole bridge is 432 m, which is composed of 112 + 208 + 112 m, and height of truss is 10 m. The height of tower is 28 m, and segment length of truss is 8 m. There are fourteen lanes in the whole bridge. The upstairs Dongguan to Shenzhen Expressway with 100 km/h design driving speed, highway-I grade load, and 2% tow-way transverse slope has bidirectional and six lanes; The downstairs Dongguan Ring Road with 80 km/h design driving speed, city-A grade load, and 1% tow-way transverse slope has bidirectional eight lanes. Moreover, on both sides of the lower layer there are also sidewalks. Dongjiang Bridge is composed of twin bridges, and width of each bridge is 16.25 m. The main trusses adopt warren trusses with vertical members, and top chords and rigid cables are connected by suspenders. Rigid cable presents a shape of suspension. The height between the centre of top chord and rigid cable is 28 m at middle bearings. Dongjiang Bridge sets three main trusses in lateral direction, with trusses spacing 2×18 m, and sway bracing is only set up on the upper part of the tower column among three trusses. The general layout of Dongjiang Bridge is as shown in Figure 1. In practical design, tower column is designed in accordance with tow-end articulated member, and the effective length of tower column lengthwise buckling is 28 m.

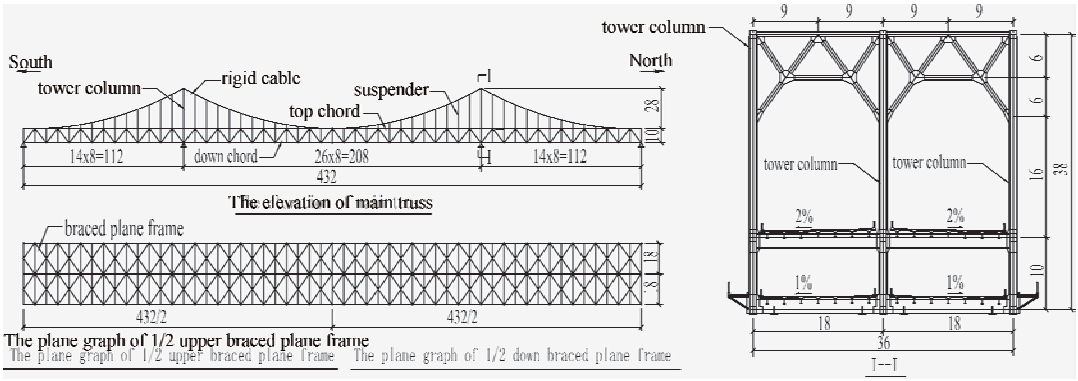

Figure 1 Total bridge layout of Dongjiang Bridge (unit: m)

MECHANICAL MODEL AND CHARACTERISTIC EQUATION FOR TOWER COLUMN LENGTHWISE BUCKLING

Simplified Calculation Model of Tower Column Lengthwise Buckling

Because towers of suspension bridge are restrained by main cables, the upper end of tower is between fully free and simply supported. The equivalent spring with level constraint can be utilized to simplify the main cable constraint to the main tower, and stiffness coefficient value of equivalent spring can be determined by stiffness of main cables and stiffening girders[3]. For steel truss bridge stiffened with rigid cables, the longitudinal horizontal displacement and rotation of the upper end of tower column are constrained by the support system provided by the stiffening strings (rigid cables) and suspenders. Similarly, by introducing the equivalent level spring with lateral restraint stiffness k_{TH} and rotating spring with rotating restraint stiffness k_{TZ}, boundary condition at the upper end of tower column can be simulated. As the spatial effect of integral structure's mechanical behaviour is significant, which make the main truss constraint to the tower column so strong that the bottom end of tower column can not produce the linear displacement, an equivalent rotating spring with rotating restraint stiffness k_{BZ} can be used to simulate boundary condition of the bottom end of tower column. The simplified calculation model of tower column lengthwise bulking can be seen in Figure 2.

Characteristic Equation of Tower Column Lengthwise Buckling

Suppose that a tower column subjected to a compressive axial load P has already buckled (Figure 3), in Figure 3 we introduce a coordinate system with its origin at the tower column's bottom end.

The terms m_T, m_B are the couples exerted on the upper and the bottom end of tower column by equivalent rotating spring:

Eqn. 1

$$m_T = k_{TZ}\theta_T,\ m_B = k_{BZ}\theta_B, \tag{1}$$

where: k_{TZ}, k_{BZ} — stiffness coefficients of equivalent rotating spring on the upper and bottom end of tower column; θ_T, θ_T — torsion angle on the upper end and bottom end of tower column.

The horizontal reaction exerted on the upper end of tower column by equivalent level spring is

Eqn. 2

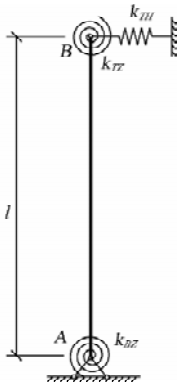

Figure 2 Simplified calculation model of tower column

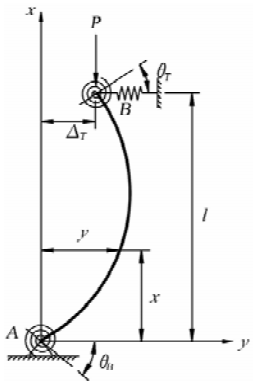

Figure 3 Lengthwise buckling of tower column lengthwise buckling

$$H = k_{TH}\Delta_T, \tag{2}$$

where: k_{TH}— stiffness coefficients of equivalent level spring on the upper end of tower column; Δ_T— horizontal displacement on the upper end of tower column.

From the equilibrium equation

Eqn. 3

$$\sum M_{p\text{ int }A} = k_{BZ}\theta_B - (P - k_{TH}l)\Delta_T - k_{TZ}\theta_T = 0, \tag{3}$$

so we can solve for torsion angle on the bottom end of tower column:

Eqn. 4

$$\theta_B = \frac{(P - k_{TH}l)\Delta_T + k_{TZ}\theta_T}{k_{BZ}}. \tag{4}$$

From the equilibrium equation, the bending moment M at arbitrary position x is

Eqn. 5

$$M = -P(\Delta_T - y) - k_{TZ}\theta_T + k_{TH}\Delta_T(l - x), \tag{5}$$

we substitute Eqn. 5 into deflection differential equation of beam $M = -EI\dfrac{\mathrm{d}^2y}{\mathrm{d}x^2}$:

Eqn. 6

$$y'' + k^2 y = \frac{1}{EI}(P\Delta_T + k_{TZ}\theta_T - k_{TH}\Delta_T l + k_{TH}\Delta_T x), \tag{6}$$

where: $k^2 = \dfrac{P}{EI}$; E— elastic modulus; I— moment of inertial.

The general solution of the second-order differential Eqn. 6 is

Eqn. 7

$$y = C\sin kx + D\cos kx + \frac{1}{k^2 EI}(P\Delta_T + k_{TZ}\theta_T - k_{TH}\Delta_T l + k_{TH}\Delta_T x), \tag{7}$$

where C and D are constants we must determine from the boundary conditions.

The boundary conditions at $x = 0$ and $x = l$ are

Eqn. 8

$$y\,|_{x=0}=0,\ y'|_{x=0}=\theta_B=\frac{(P-k_{TH}l)\Delta_T+k_{TZ}\theta_T}{k_{BZ}}, \tag{8}$$

Eqn. 9

$$y\,|_{x=l}=\Delta_T,\ y'|_{x=l}=-\theta_T. \tag{9}$$

Substituting the boundary conditions (Eqn. 8 and Eqn. 9) into Eqn. 7, we can obtain homogeneous linear equations system:

Eqn. 10

$$\begin{bmatrix} 1 & 0 & \left(1-\frac{k_{TH}l}{P}\right) & \frac{k_{TZ}}{P} \\ \cos kl & \sin kl & 0 & \frac{k_{TZ}}{P} \\ 0 & k & \left(\frac{k_{TH}}{P}+\frac{k_{TH}}{k_{BZ}}l-\frac{P}{k_{BZ}}\right) & -\frac{k_{TZ}}{k_{BZ}} \\ -k\sin kl & k\cos kl & \frac{k_{TH}}{P} & 1 \end{bmatrix} \begin{bmatrix} D \\ C \\ \Delta_T \\ \theta_T \end{bmatrix} = \begin{bmatrix} 0 \\ 0 \\ 0 \\ 0 \end{bmatrix}. \tag{10}$$

From the necessary and sufficient condition of homogeneous linear equations system (Eqn. 10) with non-zero solution, the characteristic equation of tower column buckling is

Eqn. 11

$$\begin{aligned} &k_{TH}k_{BZ}(\cos kl-1)[P\sin kl-k_{TZ}k(\cos kl-1)]-k_{TH}(\sin kl)[P(k_{BZ}\cos kl+k_{TZ})+k_{BZ}k_{TZ}k\sin kl)] \\ &+[Pk(\cos kl)(k_{BZ}+k_{TZ})+(\sin kl)(k_{BZ}k_{TZ}k^2-P^2)](lk_{TH}-P)=0 \end{aligned} \tag{11}$$

Substituting k_{TZ}, k_{BZ} and k_{TH} into Eqn. 11, we can obtain the Euler buckling load P_{cr}. Finally, the effective length factor μ of tower column lengthwise buckling can be obtained by the Euler formula.

EFFECTIVE LENGTH FACTOR OF TOWER COLUMN

Finite Element Model

The 3-D (three main trusses) and 2-D (single truss structure) finite element models of Dongjiang Bridge in finished stage are established by FEM software-midas Civil using spatial beam element with six degrees of freedom at each node. Because of the structural type of tower-girder fixed and tower-girder and Pier separated, boundary constraint conditions are applied to models instead of piers and foundation. The spatial finite element model of Dongjiang Bridge is shown in Figure 4.

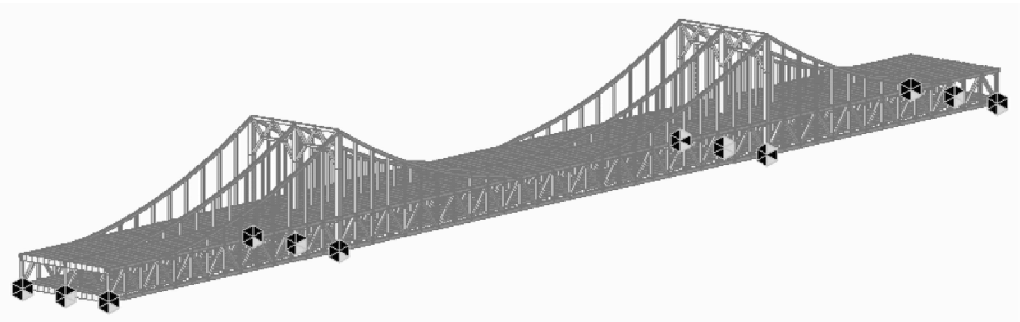

Figure 4 Spatial finite element model of Dongjiang Bridge

Stiffness Coefficients Value of Equivalent Springs

Combing physical meaning of spring stiffness and calculation process of stiffness coefficient values of equivalent springs at the end of bridge tower for the suspension bridge in the reference[3], a method, which can accurately determine the stiffness coefficient values of equivalent springs at the ends of tower column, is proposed. It includes three steps: Firstly, the generalized displacement at the end of tower column can be calculated by applying a generalized force at the end of tower column along equivalent spring direction in tow kinds of finite element models respectively, then an equivalent stiffness value k_{e1} can be obtained with dividing the generalized force by the generalized displacement. Secondly, removing the constraint between the ends of tower column and stiffened strings or main trusses, and the generalized displacement at the end of tower column can be calculated by applying a generalized force at the end of tower column along equivalent spring direction in tow kinds of finite element models respectively, then the generalized force divided by generalized displacement equals to an equivalent stiffness value k_{e2}. Finally, Stiffness coefficients values of equivalent springs at the ends of tower column can be obtained by k_{e1} subtracting k_{e2}.

TABLE 1 STIFFNESS COEFFICIENT VALUES OF EQUIVALENT SPRINGS IN TOW MODELS

Stiffness coefficient values of equivalent springs	Tower column in spatial model		Tower column in planar model
	Side truss	Middle truss	
k_{TH}	285 933.2 kN/m	342 687.6 kN/m	245 858.0 kN/m
k_{TZ}	2 439 024.3 kN·m/rad	2 439 024.3 kN·m/rad	2 380 952.1 kN·m/rad
k_{BZ}	10 000 000.5 kN·m/rad	11 111 111.3 kN·m/rad	9 090 909.4 kN·m/rad

Stiffness coefficients values of equivalent springs at the ends of tower column in spatial model and planar model are listed in Table 1. From Table 1, we can find that k_{TH} and k_{BZ} of the middle truss are somewhat bigger than that of side truss in the spatial model, which is mainly due to the constraint of sway bracing at the end of tower column and spatial effect of three main trusses, and the stiffness values of equivalent spring in the planar model are smaller than that in spatial model, which indicates that the spatial effect of three-truss can improve the integral rigidity of structure.

Effective Length Factor

Substituting stiffness values of equivalent spring shown in Table 1 into Eqn. 11, we can solve the critical load P_{cr}, then obtain the effective length factor μ of tower column by the Euler formula. Because Eqn. 11 is a transcendental equation, it is not solved by analytic method. In order to obtain more accurate numerical solution, the author programed M files by Matlab software with strong function-handling ability to solve Eqn. 11. The effective length factors of tower column in special model and planar model are shown in Table 2.

TABLE 2 THE EFFECTIVE LENGTH FACTOR OF TOWER COLUMN IN 2-D AND 3-D MODELS

The effective length factor	Spatial model		Planar model
	Tower column of side truss	Tower column of middle truss	
μ	0.620	0.617	0.624

From Table 2, we can find that the effective length factor of tower column of middle truss in tow models

are slightly smaller than that of side truss, and the effective length factor of tower column in spatial model are smaller than that in planar model. This phenomenon was attributed to improvement of constraint stiffness of tower column by sway bracing and spatial effect of three main trusses. But, the maximum difference of the effective length factor is only 0.007, and the relative error is merely 1.13%. It indicates that when calculating the lengthwise buckling of tower column in finished stage, the influences of lateral bracing and the spatial effect on tower column can be ignored, and we can directly analyze the planar model without considering those influences.

ANALYSIS OF INFLUENCE FACTOR ON TOWER COLUMN LENGTHWISE BUCKLING

Lateral Restraining Stiffness at the Upper End of Tower Column

Changing k_{TH} from 0.1 to 20 times of original value in 0.3 interval, the corresponding effective length factor of tower column is calculated, and the changing curve of the effective length factor of tower column with k_{TH} is drawn.

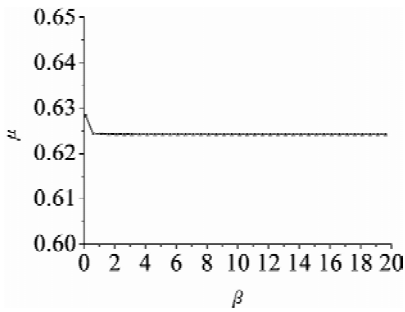

Figure 5 Change of the effective length factor of tower column with β

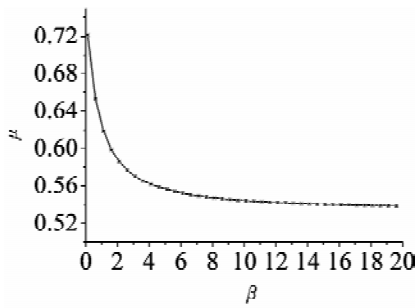

Figure 6 Change of the effective length factor of tower column with β

From Figure 5, It can be seen that lateral restraining stiffness at the upper end of tower column has little influence on μ.

Rotating Restraint Stiffness at the Upper End of Tower Column

Taking the same method, the changing curve of the effective length factor of tower column with k_{TZ} is drawn. From Figure 6, It can be seen, when $0.1<\beta<8$, μ decreases rapidly from 0.721 to 0.547, which indicates that the rotating restraint stiffness k_{TZ} at the upper end of tower column has significant influence on μ.

Rotating Restraint Stiffness at the Bottom of Tower Column

In Figure7, when $0.1<\beta<4$, μ changes from 0.746 to 0.600. Comparing Figure 6 with Figure 7, it can be found that the reduced amount of the effective length factor is larger by increasing k_{TZ} than increasing k_{BZ}, which means that the effect of increasing the rotating restraint stiffness at the upper end of tower column to improve μ is better than increasing the rotating restraint stiffness at the bottom end of tower column.

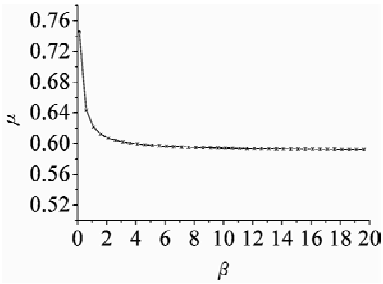

Figure 7 Change of the effective length factor of tower column with β

CONCLUSIONS

(1) For steel truss bridge stiffened with rigid cables, the influences of lateral bracing and the structural spatial effect on tower column can be ignored when analyzing lengthwise stability of tower column in finished stage.

(2) Change of lateral restraint stiffness at the upper end of tower column in wide range has little influence on μ. The rotating restraint stiffness at the bottom end of tower column has great influence on μ, and μ is decreased with the increase of k_{BZ}. The rotating restraint stiffness at the upper end of tower column has significant influence on μ, and μ can be reduced most effectively with the increase of k_{TZ}. Therefore, in design of bridge, the effective length factor can be improved by enforcing the rigidity of rigid cables system.

(3) By calculating and taking into account of certain safety margin, the effective length factor of tower in Dongjiang Bridge can be set as 0.68, which is lower than design value 1.0. In practical design, the effective length factor of tower column is conservative. Considering the change of rigidity of members and the type of joints for actual bridge, the rational ranges for effective length factor of tower column are found to be 0.65-0.8.

ACKNOWLAGEMENTS

This research was supported by Research Fund for the Doctoral Program of Higher Education of China (Grant No. 20090205110002) and the Youth Foundation of Taiyuan University of Science and Technology (Grant No. 20113018).

REFERENCES

[1] Zhang, J.G., Liu, Y.J. and Yao, X.R., et al. "Parameters sensitivity analysis of steel truss bridge stiffened with rigid cable", Journal of Zhengzhou University:Engineering Science, 2010, 31(5), pp.55-59. (in Chinese)

[2] Xie, T., Tian, Y. and He, Y., et al. "Analysis of lateral buckling stability of pylons of Fumin Bridge in Shenyang", Bridge Construction, 2004, 34(s1), pp.24-27. (in Chinese)

[3] Liu, E.J., "Analysis of longitudinal stability of tower of suspension bridge", World Bridges, 2009,(2), pp.45-47. (in Chinese)

[4] Xiong, W., Jin J. and Xiao, R.C., "Calculation method for ultimate state of load-carrying capacity of concrete

pylons of cable-stayed bridge", Bridge Construction, 2008, 38(6), pp.37-40. (in Chinese)

[5] Zeng, Q.Y. and Zhu, H.H., "An introduce to the stability problem and the calculation of the effective length of tower and main girder for cable-stayed bridge", Journal of Changsha Railway University, 1991, 9(3), pp.16-28. (in Chinese)

[6] Chen, X., "Analysis of stability of pylon of the second Yangtze river bridge in Wanzhou", Railway Engineering, 2007, (12), pp.04-06. (in Chinese)

[7] Liu, Y.J., Liu, J. and Zhu, M., et al. "Static and dynamic model design of total bridge of double-deck and three main trusses steel bridge with rigid cable", Journal of Architecture and Civil Engineering, 2008, 25(1), pp.84-87. (in Chinese)

[8] Liu, Y.J., Liu, J. and Zhong, G.X., et al. "Mechanical behavior of steel truss bridge stiffened with rigid cables in construction stage", Journal of Traffic and Transportation Engineering, 2009, 9(3), pp.1-10. (in Chinese)

[9] Liu, Y.J., Liu, J. and Huang, J.C., "Test model of whole bridge of double-deck and three main trusses steel bridge with rigid cable", Journal of Architecture and Civil Engineering, 2008, 25(3), pp.61-65. (in Chinese)

[10] Liu, Y.J., Liu, S.Z. and Zhang, J.G., et al. "Internal force adjustment of three main trusses and its influencing parameters in steel truss bridge with three main trusses and double decks", Journal of Guangxi University: Natural Science Edition, 2011, 36(1), pp.75-82. (in Chinese)

EXPERIMENTAL VERIFICATION AND ANALYSIS OF TEMPORARY BRIDGE STRUCTURE ACTUAL BEHAVIOUR

* M. Karmazínová, J.J. Melcher, M. Pilgr and M. Štrba

Faculty of Civil Engineering, Brno University of Technology
Veveří St. 331/95, 602 00 Brno, Czech Republic
* Email: karmazinova.m@fce.vutbr.cz

KEYWORDS

Temporary bridge, provisional purpose, actual behaviour, experimental verification, loading test, test set-up, loading mode, loading method, analysis, deflection, stress, gauge.

ABSTRACT

The paper deals with the problems of the analysis and experimental verification of the actual behaviour of the structural system used for the provisional bridging purposes. This paper presents the brief information on the results of the full-scale loading test of the particular type of the temporary bridge. The subject of the loading test is the special railway bridge of the structural system of "ŽBM 30", i. e. military demountable bridge developed by the railway military and used as a temporary bridge for the bridging with the span up to 30 m. This system with plate main girders and upper deck is usable for the temporary reconstruction of single-track railway bridges. The loading test has been oriented to the verification of the actual behaviour of this structural system during the loading process, with the accent to the objective load-carrying capacity and rigidity. Mainly the loading test was aimed to obtain the information and data on the actual loading of the main load-carrying structural system members, their stress states and deflections within the usual service loading actions. The loading procedure and corresponding principle of the test equipment used for the realization of the full-scale loading test have been developed and elaborated to the form of the specific loading test set-up by the paper authors. For the evaluation and generalization of the test results the analytical methods including the numerical modelling have been used.

The authors workplace deals with the experimental verification in the long term and the authors have many experiences and large set of the realized works oriented to the experimental verification, both loading tests in laboratory and also full-scale tests in the exterior (see references from [1] to [7]).

OBJECT OF INVESTIGATION

The object of the theoretical and experimental investigation is the special railway bridge, so called "ŽBM 30", developed by railway army in the past and utilizable as the temporary bridge structure for the substitution of bridge structures with the spans up to 30 m. The system of "ŽBM 30" with web-plate main girders and upper bridge deck is available for the reconstruction or temporary substitution of single-track

railway bridges. The basic structural system of the bridge is composed of the following main structural parts: main girders, transverse bracings, horizontal bracings, bearings, bridge deck or pavement, respectively (in the case of the possible usage for road bridges). Basic structural members of main girders and the variability of the structure disposition together with the possible change of the bearing location give the spans L in the range from 12 to 30 m.

The test specimen for loading tests and for subsequent theoretical analysis was represented by the particular structural composition of the railway temporary bridge system of "ŽBM 30" for two main girders of the span of L = 18 m. The main girder consists of three segments — two trapezoidal ended segments with the length of 6 m and one rectangular middle segment with the length of 6 m, too. The welded I-cross-section of the main girder has the height of 1 800 mm in the span middle, the height of the main girder in the supports makes 900 mm, the axis distance of main girders is 1 512 mm. The transverse stiffness of both girders is given by eight (in common) transverse bracings — four web-plate bracings displaced around the girder ends and four truss ones displaced in the girder middle part. The illustrations of the actual composition of the test specimen are depicted in Figure 1.

(a) view to the main girders and supports created by members of "PIŽMO" system

(b) truss transverse bracings

Figure 1 Set-up of the "ŽBM" temporary bridge for the span of 18 m

The necessity of the verification of actual behaviour, stresses and stiffness of the railway bridge "ŽBM 30" was caused by previous experiences with its usage in civil engineering practice, which indicate, its actual behaviour and static parameters during operating loading actions not quite correspond with the data and parameters given in producing and assembly sources.

LOADING TESTS REALIZATION

Loading Method Principle

For the loading tests realization the general loading principle without the need of any fixedly anchored loading frame, i. e. without the necessity of the testing equipment anchorage, has been utilized. The system is composed of the tested girder and seating girder, that the tested girder is supported by the seating girder in the end supports. Across the upper edge of the tested girder and across the lower edge of the seating girders the cross-girders are lead; to the cross-girders the ties rods going besides of the tested girder are anchored. The ties are lead through the hollow hydraulic cylinders, by them the loading actions are generated; due to this effect the ties rods are tighten and they introduce the load through the cross-section to the tested girder. The general loading principle is evident from the scheme in Figure 2.

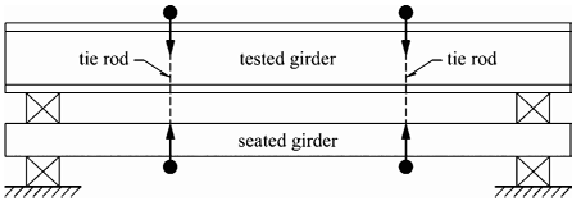

Figure 2 Scheme of general loading principle

The loading system is in the equilibrium state. The seating girder must have the sufficient flexural stiffness and load-carrying capacity to be able to resist the introduced loading actions and not to have oversize deformations. The seating girder is supported by the end supports put on the ground to obtain the space enough under the seating girder for the cross-girders. Between the tested and seating girder the height space for the free deformation of both main components of the testing system.

Loading Test Arrangement

In the areal of the FIRESTA Inc. Company in the city of Brno — Mǒdrice the load-carrying structure of "ŽBM" bridge for the span of 18 m has been assembled. Because of large proportions and weights of the test specimens the portal crane of load-bearing capacity of 60 tons has been utilized for the erection.

The arrangement of the loading equipment based on the loading principle described above is shown in Figures 3 and 4. For the structure of the loading equipment (seating girders, cross-girders, tie rods) the members of various bridge systems for provisional purposes have been utilized. The test specimen has been supported by seating girders consisting of two pairs of the beams IP100, which have been together utilized for the loading ties anchorage. Main girders of the test specimen have been beard through steel bearings on the supports representing by members of the "PIŽMO" structure. In the location of the hollow transverse web stiffness two introducing cross-girders consisting of members R4 have been transferred across upper flanges. Longitudinal introducing girders (one above each main girder) representing by members R28 have been put on these ones. Helping two other cross-girders of the members R2 and R4 leading across upper flanges of longitudinal introducing girders, outside test specimen the tie rods have been lead. Ties rods have been lead through the holes in hollow loading cylinders put on the upper cross-girders and have been anchored to the lower cross-girders (also R2 members) leaned from below to supporting girders IP100. In the place of test specimens supports the supporting girders have been beard on the support cross-girders of the same members R2, which have been put on the ground.

The test specimen has been loaded introducing the loading actions together to both main girders (Test T1) and also introducing the loading actions through one main girder only (Test T2) aimed to investigate the degree of interaction of both main girders and to verify the effect of transverse bracings from the viewpoint of the transverse distribution of loading.

Loading Mode and Procedure

The maximum load of one main girder has been defined according to requirements of the co-operating company, for which the tests have been performed. The test load has been derived from the values of the operating loading actions actual in the practice usage for provisional purposes and it has been limited by the condition, that no failure or damage should not occurred, because of the ability to use the temporary

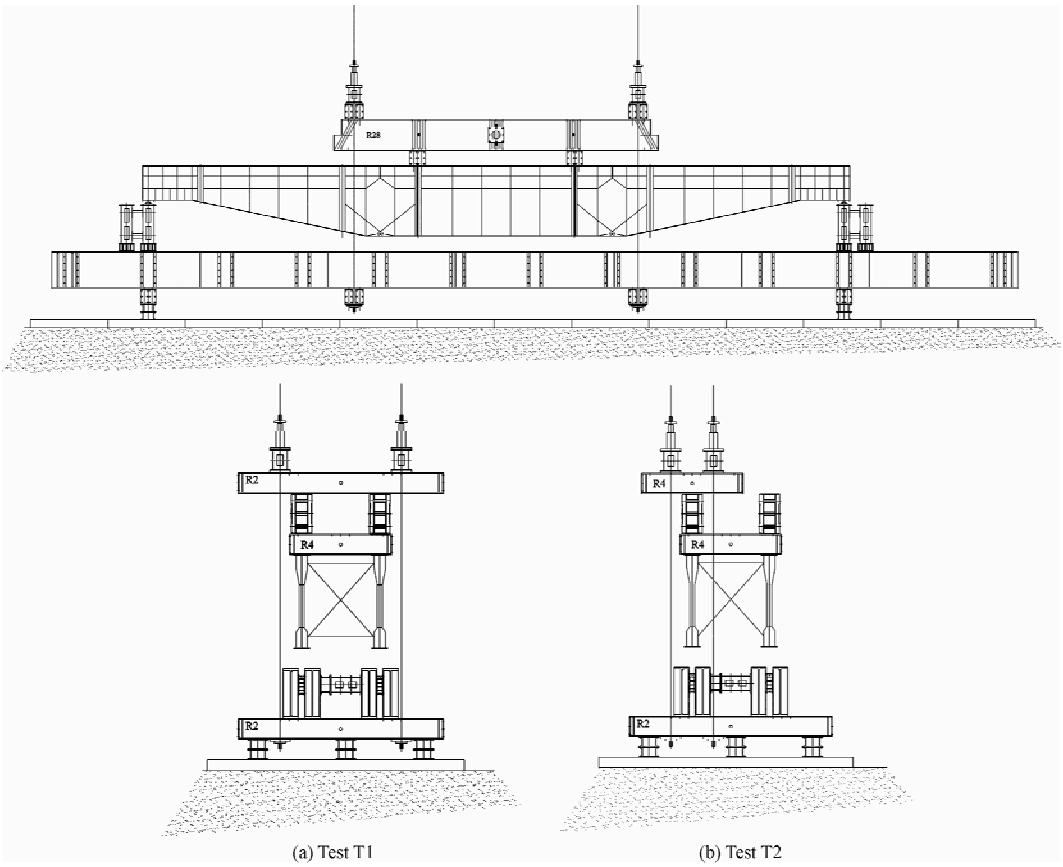

Figure 3 Test arrangement: scheme of the testing equipment set-up

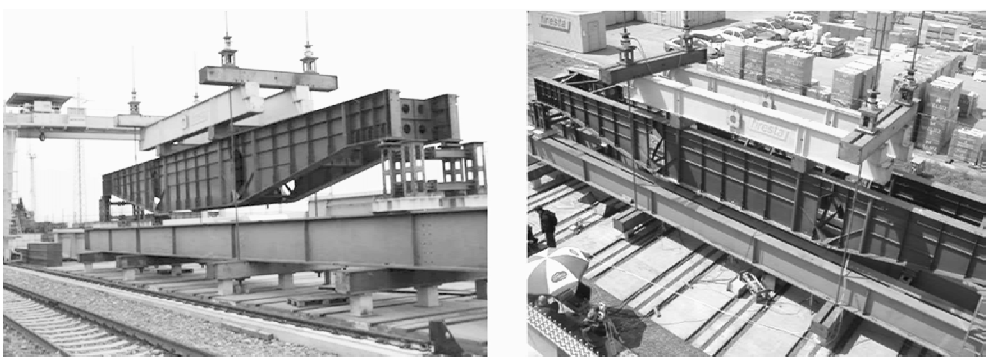

Figure 4 Test arrangement: actual testing equipment set-up — overall views

bridge in the next time. On the base of that, the test loading has been determined as continuous uniform load of 50 kNm^{-1} for one main girder. Because the loading method utilized in given conditions does not allow the uniform load application, the loading actions have been realized applying two forces introduced to the main girders in the hollow transverse stiffness positions. The forces values have been derived from the given uniform load based on the equivalent maximum bending moments in the beam. For derived testing load, the forces in the loading cylinders have been determined for Test T1 and Test T2 separately.

In the case of Test T1 the tie rods have been lead outsides the whole loading system to introduce the load together to both main girders. In Test T2 the ties rods have been lead outsides one main girder to introduce the load to this one girder only. The load has been introduced as the forces generating by hydraulic jacks: in the case of Test T1 (load introduced to both girders together) the cylinder forces V_1 have been applied to the girder N_1 and the cylinder forces V_2 have been applied to the girder N_2 (see Figure 5a); in the case of Test T2 (load introduced to one girder only) the cylinder forces V_1 have been applied to the girder N_1, while the girder N_2 has not been directly loaded (see Figure 5b).

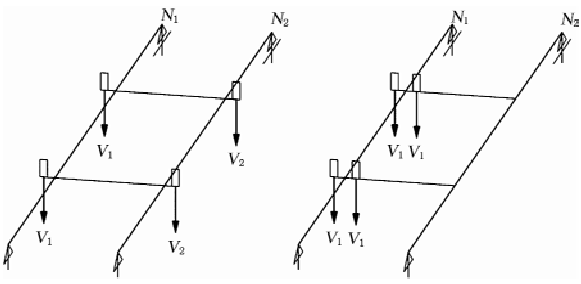

Figure 5 Forces in cylinders: Test T1 (left); Test T2 (right)

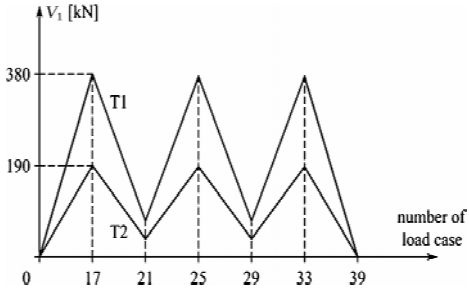

Figure 6 Loading mode scheme

The loading mode has been specified considering that to obtain the loading effects for the maximum assumed load value of 50 kNm^{-1} loading to one main girder; for this maximum load the corresponding maximum loading force for one main girder has been calculated. It is possible to expect, that during the initial load cases when the load values are low, at first the displacement of supports and connections occur, so that the loading process has been performed by 3 loading cycles including in common 39 load cases. The first loading cycle started by zero force values (load case No. 1) and the load has been increased step by step up to the maximum force value corresponding to the load case No. 17. In the second (decreasing) phase of the first cycle the sequential offloading has been applied to the force value of 75 kN (load case No. 21). The second loading cycle also included two phases, increasing phase in the range of the load cases from No. 21 up to No. 25 and decreasing one in the range from No. 25 to No. 29. The third loading cycle included the increasing phase from the load cases No. 33 up to No. 39 and the decreasing one from the cases No. 33 to No. 39 that means to quite offload of the structure. The graphic scheme of the loading mode is drawn in Figure 6.

LOADING TEST RESULTS

The methodology of the measurement and the selection of observed quantities have been subordinated to the requirements of the co-operating company. Considering these requirements, the measuring points have been selected on the tested structure; during the loading tests the vertical deflections and stresses of main girders have been monitored in these points. These measuring points have been located to the cross-sections with extreme expected deflections and stresses.

Structure Deflections

Potentiometer sensors measuring deflections have been located in the span middle, in the connections of the segments and closed to the supports. On each girder five deflection sensors have been located (see Figure 7) in the same points to be evidently seen the comparison of the deflections of both girders.

In the case of loading both girders (Test T1) the deflections of both girders in the corresponding points were nearly the same. Then it is evident, that the load introduced to both girders practically identically, so both girders have been loaded equally. For the illustration the measured deflection values are drawn in the graphs in Figure 8: the deflections of the girder N_1 in the points P1–P5 for Test T1 are drawn in Figure 8a) (the values of the deflections of the girder N_2 in corresponding points P6–P10 have been very similar); the deflections of both girders N_1 and N_2 in the points P1–P10 for Test T2 are drawn in Figure 8b).

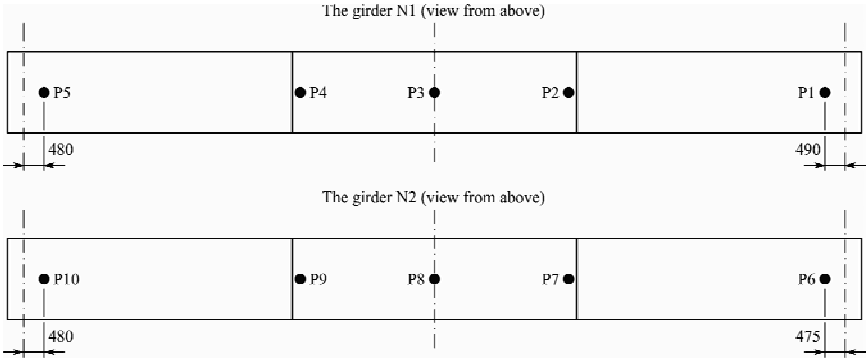

Figure 7 Location of potentiometer sensors of the deflections on the surface of the lower flange

In the case of loading both girders (Test T1) the deflections of girders in the corresponding points were nearly the same. Then it is evident, that the load introduced to both girders practically identically, so girders have been loaded equally. For the illustration the measured deflections are drawn in the graphs in Figure 8: the deflections of the girder N_1 in the points P1–P5 for Test T1 in Figure 8a) (the values of the deflections of the girder N_2 in corresponding points P6–P10 have been very similar); the deflections of both girders N_1 and N_2 in the points P1–P10 for Test T2 in Figure 8b). From graphs in Figure 8 it is obvious, that the deflections of the girders N_1, N_2 have been significantly different in the case of load introducing to one girder only, even the signs of the deflections of the girders N_1, N_2 were inverse, i.e. the girder N_2 moved up, no down. The maximum deflections of the girder N_1 in the case of Test T2 were by less than 10% smaller than the deflections of the girders in the case of Test T1. It indicates the fact, that the degree of the interaction of both girders from the viewpoint of the load transfer by transverse bracings is practically negligible. If the load has been introduced through one girder only, the loading effect to next girder does not show almost at all and the girder directly loaded introduces the significant load part.

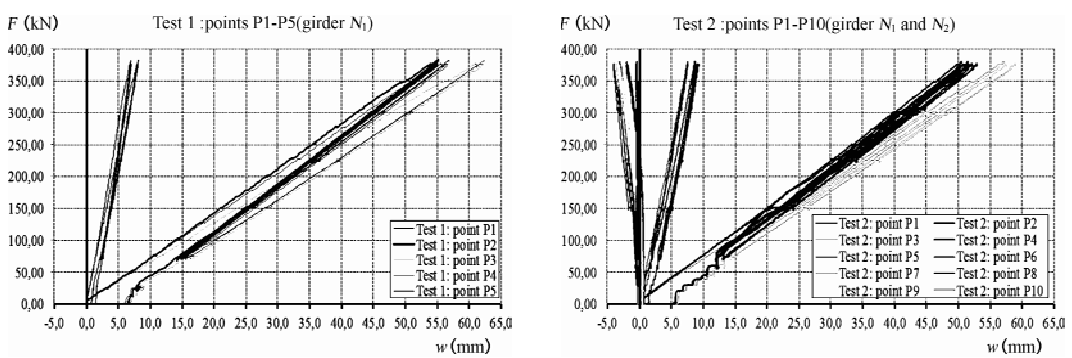

a) b)

Figure 8 Deflections: a) Test T1 — girder N_1; b) Test T2 — girders N_1, N_2

Structure Stresses

The stresses of the structure have been determined helping the strain gauges and recalculating the strains to the stresses. The gauges have been located in the point with expected extreme stresses, i. e. in the middle of the girder span, in the connections of the segments and in the place of the cross-section change on the beginning of the haunch. The strain gauges have been located on the lower surface of the bottom flange, in the middle section three gauges across the flange width, in other sections one gauge on the flange surface. The scheme of the location of the gauges T1-T16 on both girders is drawn in Figure 9.

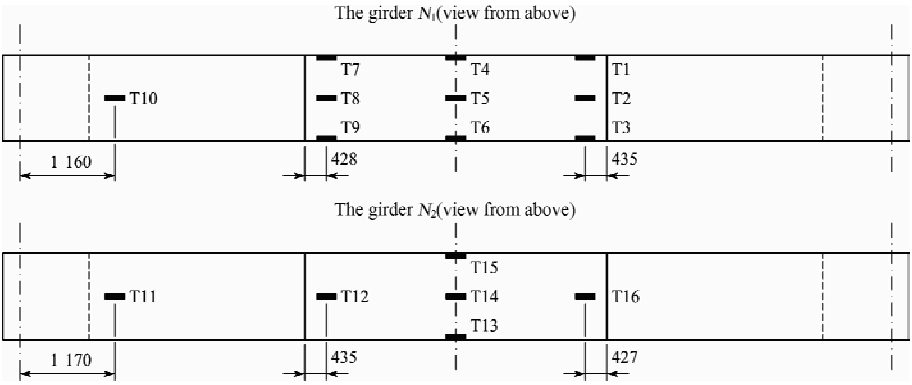

Figure 9 Location of strain gauges on the surface of the lower flange

In the graphs in Figure 10 the normal stresses in the girders N_1 and N_2 are drawn for Test T2, for the illustration. The stress distribution is drawn in the measured points along the span for the selected load levels. As expected, from the graphs it is evident, that the stresses in the connections are considerably larger than the stresses in the span middle, which is caused by the significantly smaller cross-section in the connection of the middle and support structural segments. Also from the figures it is evident, that in the case of the load introducing to one girder only, the load effect to the next girder does not show practically at all and the significant load part is introduced by directly loaded girder. It again confirms the obtained fact, that the degree of the interaction of both girders through the transverse bracing is minimal, so the transverse introduction of the load is not practically employed.

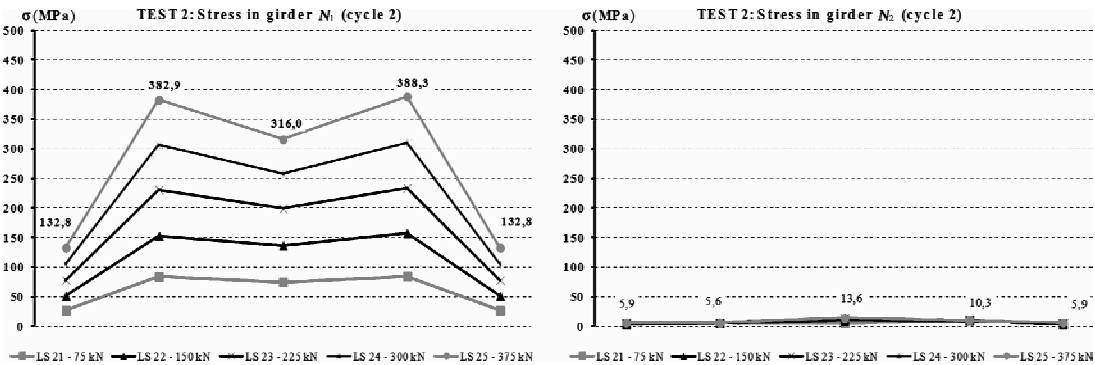

Figure 10 Normal stresses: Test T2 — girders N_1, N_2

RESULTS EVALUATION AND CONCLUSIONS

The stiffness of the main girder is going from the structure deflections, which do not exceed the value given of L / 300 as the basic value for the deflection limit of the usual structural members. Considering the fact, that the investigated structure is determined for the provisional and temporary bridges, it is possible to take the value of L / 300 as satisfied from the viewpoint of the structure stiffness and that means also from the viewpoint of the serviceability.

The stresses in any measured points of the main girder do not exceed the yield strength of applied steel given in the producer sources. The maximum stresses for the maximum loads reach about 76% of the yield strength and the structure has the sufficient load-carrying capacity reserve. As expected, the larger normal stresses occur in the connections of the end parts and middle part, which is influenced by the smaller cross-sections. But nor here the stresses are not larger than 76% of the yield strength.

The results mentioned above show the quite significant fact, that the degree of the interaction of the girders and by this also the load transfer to both girders is negligible if the load is introduced through one girder only. It indicates that it is practically impossible to take into account the effect of transverse bracings to the load transfer to both girders. If the load is introduced directly to one girder only it is necessary to consider, that almost the complete loading effect is introduced by this directly loaded girder, what fact shall be consistently respected in the practical usage.

ACKNOWLEDGEMENT

The paper has been elaborated within the solution of the projects MSM 0021630519 and TAČR No. 01030849.

REFERENCES

[1] Karmazínová, M., Melcher, J. J., "Methods of the design assisted by testing — applicable tools for the design resistance evaluation using test results", In Proceedings of the 2nd Intl. Conf. on Mathematical Models for Engineering Science, WSEAS Press: Puerto de la Cruz, 2011, pp.31-36. ISBN 978-1-61804-055-8.

[2] Karmazínová, M., Melcher, J. J., "Design assisted by testing applied to the determination of the design resistance of steel-concrete composite columns", In Proc. of the 13th WSEAS International Conference on Mathematical and Computational Methods in Science and Engineering, WSEAS, Catania, 2011, pp.420-425. ISBN 978-1-61804-046-6.

[3] Karmazínová, M., Melcher, J. and Kala, Z., "Design of expansion anchors to concrete based on the results of experimental verification", Advanced Steel Construction, an International Journal, Vol. 5, No. 4, Hong Kong Institute for Steel Construction, December 2009, pp.390-405. ISSN 1816-112X.

[4] Karmazínová, M., Melcher, J., Štrba, M., "Fastening of steel structural members to concrete using post-installed mechanical fasteners", In Proc. of the 9th Intl. Conference on Steel-Concrete Composite and Hybrid Structures, Singapore: Research Publishing Services: 2009, pp.549-554. ISBN 78-981-08-3068-7.

[5] M. Karmazínová, M. Štrba, V. Kvočák, "Steel-concrete composite members using high-strength materials in building constructions — structural design, actual behaviour, application", In Proceedings of the 2nd European Conf. on Civil Eng., WSEAS Press: Puerto de la Cruz, Tenerife, 2011, pp.47-52. ISBN 978-1-61804-057-2.

[6] Melcher, J., "Full-Scale Testing of Steel and Timber Structures: Examples and Experience", In Proceedings of

Structure Assessment — The Role of Large and Full Scale Testing, E&FN SPON, London, 1997.

[7] Melcher, J., Karmazínová, M., Pozdíšek, J. "Experimental verification of behaviour of composite steel and glass-fibre-concrete beam", In Proceedings of the 9th International Conf. on Steel-Concrete Composite and Hybrid Structures, Singapore: Research Publishing Services, 2009, pp. 390-395. ISBN 978-981-08-3068-7.

POST-EVALUATION OF THE FIRED CONCRETE BRIDGES REPAIRED BY STEEL PLATE AND CONCRETE COMPOSITE STRENGTHENING TECHNIQUE

* C.S. Wang[1], L.P. Liu[1], L.J. Feng[1], Z.Y. Yuan[2]

[1] Engineering Research Center for Large Highway Structure Safety of Ministry of Education, Chang'an University, Xi'an, 710064, China
[2] Xi'an Highway Research Institute, Xi'an, 710064, China
* Email: wcs2000wcs@163.com

KEYWORDS

Steel plate and concrete composite strengthening method, prestressed concrete bridge, dynamic strain monitoring, the bridge stiffness, ultimate bearing capacity.

ABSTRACT

TheYao Zhou Uplink Viaduct damaged in a fire accident was repaired using steel plate and concrete composite strengthening (SPCCS) technique. After strengthening and servicing normally for 1.5 years, two loading tests, meanwhile, a three-day traffic information observation and dynamic strain monitoring were carried out. The static loading test and monitoring results all showed that the Yao Zhou Uplink Viaduct had good service condition since reinforcement, which satisfying the safety requirement. In order to evaluate the effectiveness of the SPCCS technique in-depth, structural behaviour under the ultimate limit state (ULS) and the serviceability limit state (SLS) were analyzed. The SLS and ULC of the key sections before and after reinforcement were calculated using the simplified formula and the finite element models calibrated by filed test results. The post-evaluation results showed that the behaviour of the spans damaged in fire accident could be improved obviously under the SLS using SPCCS technique, as well as the bridge stiffness enlarged than the original bridge structure. What's more, the ultimate bearing capacity (UBC) of the key sections was improved about 75% using SPCCS technique, which was two times as the most disadvantageous load effect combinations.

INTRODUCTION

Steel plate and concrete composite strengthening (SPCCS) is a new reinforcement technology on the basis of the steel plate-concrete composite reinforced beam, is an effective combination of the section enlargement method and the steel pasting method, and is an innovation and development to the structure-strengthening technology. Steel plate-concrete composite reinforcement is that reinforced part and original structure work together as a whole by welding studs on the steel plate, planting steel bars on the surface of the original concrete, casting concrete in the original structure and the reinforcing steel plate, etc[1]. Steel plate-concrete composite reinforcement technique can effectively reinforce existing damaged and unsafe bridge. Some experimental results show that the reinforcement technology can greatly improve

the bearing capacity of the concrete beams[1-4]. J.G. Nie in Qinghua University carried out experimental research in the steel-concrete composite reinforced concrete beam[2]. C.S. Wang in Chang'an University once experiment on the flexural performance of the steel-concrete composite reinforced concrete T beam and got some theories[3-4]. On account of the existing research work, steel plate-concrete composite reinforcement technique was applied in the maintenance and strengthening of the Yao Zhou Uplink Viaduct, a prestressed concrete (PC) box girder bridge built in 1997, which were damaged by fire accident in 2009. Reinforcement effect was then evaluated. All these work in this paper motivate the popularization and application of the strengthening technology in bridge engineering.

GENERAL INFORMATION OF ACTUAL BRIDGE REINFORCEMENT

The highway from Xi'an to Tong Chuan is the important sections in Shaanxi province of the national highway from Baotou, Inner Mongolia, to Mao Ming, Guangdong. Yao Zhou Viaducts contain long bridges in the uplink and down link on the highway located at Yao Zhou City from Xi'an to Tong Chuan. The viaduct in uplink is a prestressed concrete (PC) continuous box girder bridge. The substructure of uplink bridge is the u-shaped abutment, double cylindrical piers, the single column pier and bored pile foundation. Bridge deck width contains 0.5 m fence, 9.75 m carriageway and 0.5 m fence.

At about 3:00 AM on May 27, 2009, a tank truck loaded with gasoline passed Yao Zhou Uplink Viaduct. Because of slippery road in rainy day, the truck turned over onto the fence of the overpass, leading to gasoline tank cracking. A lot of gas was flowing to the river through the weep hole and, at the same time, fire accident was caused. Shaanxi Freeway Engineering Consultant Company made detection for Yao Zhou Uplink Viaduct in June 2009. The upper structure of this burned bridge is 4×29.6 m continuous PC continuous box girder. The beam is 1.6 m in height. The substructure is single column piers and pile foundation. The specific strengthening scheme is determined according to structural damage degree of uplink viaduct. On one hand, the SPCCS method is used for the seriously damaged beams (beam 1～3 in the 85th span, beam1 in the 86th span). Second, sticking steel board reinforcement method is used for the generally damaged beams (beam 4 in the 85th span, beam 2 in the 86th span).

FINITE ELEMENT MODEL ESTABLISHMENT AND OPTIMIZATION

Basic Assumption of Finite Element Model

The large universal finite element software ANSYS was used to accurately simulate the effect of fire to integral rigidity of Yao Zhou Uplink Viaduct, and the bridge behavior after strengthening. In order to guarantee finite element model to simulate mechanics behaviors of real bridge effectively, the following assumptions were made. First, it was considered neither the stress redistribution of bridge before and after fire, and assumed the material mechanic of prestressed reinforcement and non-prestressed reinforcement is unchanged. Second, material property of burned concrete should be considered by multiplying reduction factor to consider the effect of fire to stiffness of the whole bridge. After the strain calculation of key positions, the strain should be multiplied by nominal elastic modulus to obtain nominal stress to express stress change of burned concrete. Third, whether using the steel plate and concrete composite reinforcement or plate sticking reinforcement for the injured girder, it was assumed both reinforcement method could obtain ideal effect. There was no relative displacement between original girder and new added concrete, between steel plate and new added concrete, and between plate sticking

and original girder.

Establishment and Optimization of Finite Element Model

In the numerical analysis model, common nodes were used to simulate connection between strengthening steel plate and new added concrete. By generating constraint equation for the interfaces, girder, diaphragm, strengthening concrete, plate sticking, main reinforcement and pre-stressed tendons a whole structure was formed.

Due to the complexity of Yao Zhou Uplink Viaduct after reinforcement, every components of the bridge was meshed respectively, such as pre-stressed reinforcement, added concrete and so on. By generating constraint equation between the interfaces, components were assembled together and work as a whole. Figure 1 shows the whole bridge model with imposing nodal load on real loading position. Considering fire effect for bridge integral rigidity, elastic modulus reduction was considered for severe injured concrete. According to monitoring and evaluation report, the area and material character of injured concrete were determined, and the elastic modulus reduction factor was determined for injured concrete, shown in Figure 2.

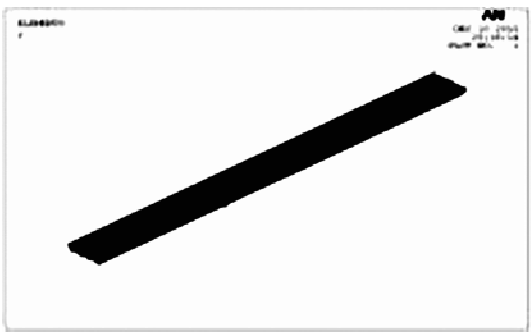

Figure 1 Whole bridge model.

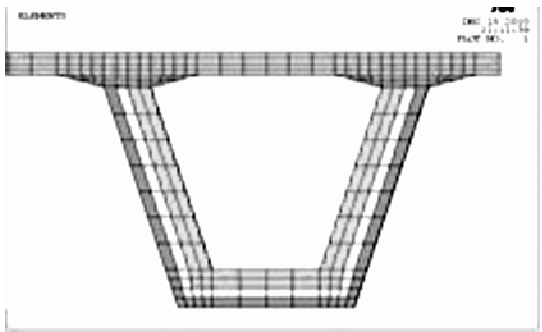

Figure 2 FE details model of burned section.

The cross section of severe injury concrete was divided into four layers from outside to inside. According to detection report, reduction factors were provided at different depth of concrete. The outer layer concrete was damaged severely in fire accident and relatively smaller factor were used in elastic modulus reduction. For the secondary outer layer, relatively greater reduction factor was adopted. For the internal two layers, no reduction was considered. Compared the calculated result with measured value, reduction factor at different locations was constantly adjusted.

LOAD EXPERIMENTAL STUDY OFREAL BRIDGE

Two load tests were carried out for Yao Zhou Uplink Viaduct after reinforcement and one year later after reinforcement, respectively. Only the first load test is introduced in following section considering the similarity of these two load tests.

Basic Situation of Load Test

For guaranteeeffectiveness and rationality of loading test, the most disadvantageous loading situation was

considered. Loading was divided into central loading and eccentric loading. In central loading, actual vehicle wheel distance of 1.3 m was adopted. In eccentric loading, the vehicle wheel was 0.5 m away from parapet and the wheel distance was 1.3 m.

Static load test of bridge was carried out according to the following loading condition. In load condition 1 and 2, central and eccentric loading were conducted for the most disadvantageous section in the 86th span. In load condition 3 and 4, central and eccentric loading were conducted for negative region at interior pier in the 85th span. In load condition 5 and 6, central and eccentric loading were conducted at the most disadvantageous section in positive region in the 85th span. Loading position and test point arrangement of all loading conditions are shown in Figure 3 and 4.

Loading Test Result Analysis

Deflection test loads were carried 8 times totally. In each load condition, loading was conducted twice, and the average deflection of two times loading was used. The average value of checking coefficient for load condition 1, 2, 5 and 6 was between 0.88 to 0.96 and the structural rigidity met the requirement. Stress test loaded 12 times totally, and each load condition loaded twice. The average checking coefficient of load condition1 to 6 was respectively 0.78, 0.84, 0.94, 0.96, 0.79 and 0.72. Time-domain and frequency domain curve of bridge vibration were measured by accelerometer installed bridge. According to testing results, the structure vibration curve was accord with vibration regularity of continuous beam bridge. It showed that integral rigidity of Yao Zhou Uplink Viaduct after strengthening was improved greatly.

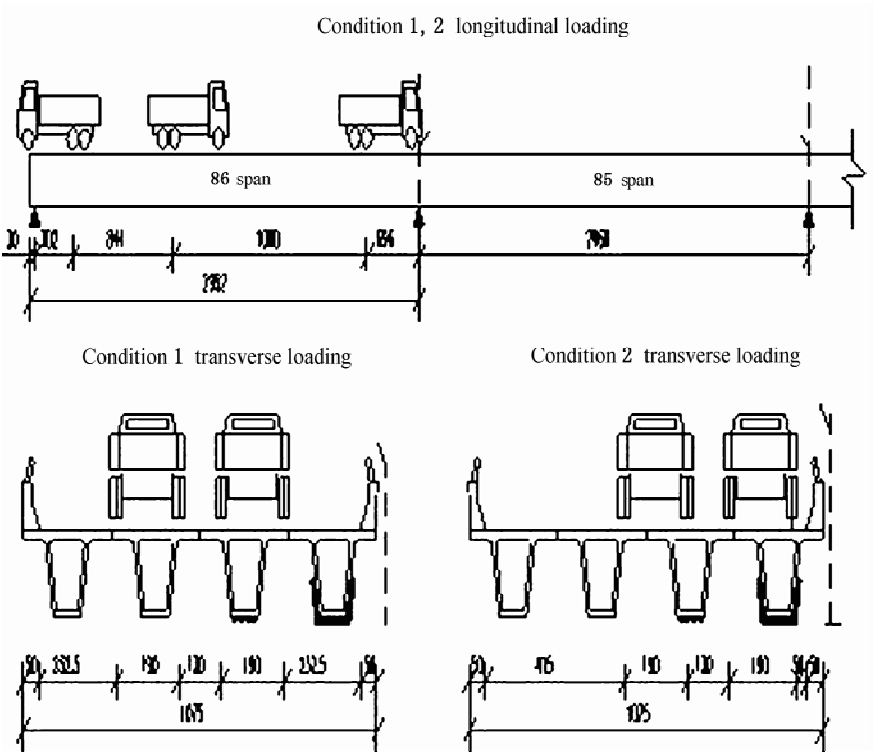

Figure 3 Details of loading position.

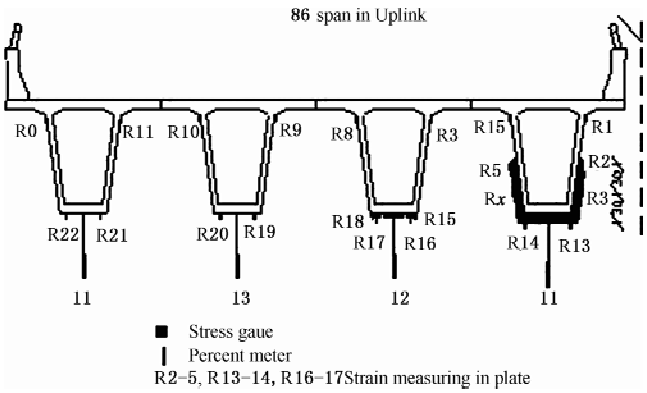

Figure 4 Arrangement of measuring points.

MONITORING OF TRAFFIC FLOW AND DYNAMIC STRAIN

Dynamic strain monitoring was conducted for three days on Yao Zhou Uplink Viaduct to evaluate the performance of bridge after reinforcement combined with static-dynamic load test.

Traffic-flow on Site

The two and half days traffic survey was carried out for Yao Zhou Uplink Viaduct from February 23rd, 2011 to February 26th, 2011. The total traffic flow was 15 271 vehicles for uplink viaduc. The passing vehicle-type consisted of two-ax truck, three-ax truck, four-ax truck, five-ax truck, six-ax truck, bus and car. The peak of passing vehicles was between 10:00 to 11:00 AM. The traffic flow was relatively larger in daytime. Another peak appeared at 10:00 PM on February 24th, and there were more cars.

Dynamic-strain Monitoring

The dynamic strain monitoring for Yao Zhou Uplink Viaduct is shown in Figure 4. Sections at 0.4 L of the 86th span and mid-span of the 85th span in uplink were selected for dynamic-strain monitoring, to compare dynamic-strain response of the maximum load-effect section under real vehicles load and under design truck load in China specification. Most measuring dynamic-strains did not exceed the strains produced by corrected design truck load on related sections, which showed the bridge behaviors well in normal operation stage.

BRIDGE EVALUATION UNDER SERVICEABILITY LIMIT STATES

For better evaluating the mechanical behavior of strengthened bridge and reflecting stiffness changed in three stages (before fire, after fire and after strengthening), the bridge key-positions were carried out for stress and deflection comparison before and after reinforcement under SLS.

Stress Assessment Under SLS

The most adverse load combinations include load combination 1 (dead weight of girder + pre-stressing

effect + secondary loads + secondary contraction + secondary creep), load combination2 (dead weight of girder + pre-stressing effect + secondary loads + secondary contraction + secondary creep + the most adverse vehicle load), and load combination 3 (dead weight of girder + pre-stressing effect + secondary loads + dead weight of reinforced concrete etc. + secondary contraction + secondary creep + the most adverse vehicle load). In these three load combinations, the first class vehicle load is used and coefficient of other load effect is 1.

To better evaluate the load carrying ability enhancement of Yao Zhou Uplink Viaduct before and after reinforcement, several sections were selected for checking, including 4 sections in side-span (0.25 L, 0.4 L, 0.5 L, 0.75 L), middle-supporting section and three sections in mid-span (0.25 L, 0.5 L, 0.5 L). Considering the asymmetry of cross-section reinforcement, different transverse loading-position were took into account, including left offset-load, mid-load and right offset-load. Longitudinal load-position of moving-load was the most adverse load-position of each checking-section relevantly. From Figure 5, it can be seen that steel plate and concrete composite strengthening can better improve force condition under the state of serviceability, as is plate sticking reinforcement.

Deflection Assessment Under SLS

In evaluating deflection-effect of Yao Zhou Uplink Viaduct using the most adverse load-combination under SLS, the selected load-combination was the same as that used in stress assessment. Checking-section is taken as 0.4 L of side-span and the middle of mid-span. From Figure 5, it shows that the integral rigidity of bridge is decreased after fire. And composite strengthening and plate sticking reinforcement can effectively improve the integral rigidity of bridge. The integral rigidity of bridge reinforced is greater than the original bridge.

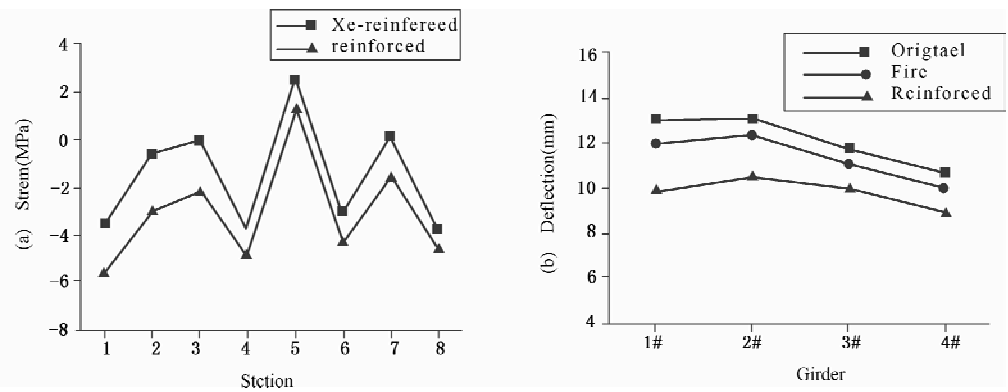

Figure 5 Stress and displacement comparison of the key sections before and after reinforcement.

BRIDGE EVALUATION UNDER ULTIMATE LIMIT STATE

Numerical Calculation of Resistance on Key-section

Ultimate-resistance of 0.4 L-section in side-span and middle-section in mid-span before and after fire was calculated by ANSYS software. Two-point loading was used to prevent early local deformation failure. And supporting way was simply-supported form. According to results of the UBC of the key sections, it

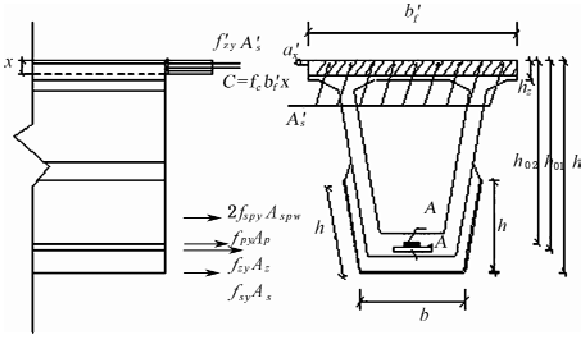

Figure 6 Calculation diagram for the UBC of normal section of SPCCS beams.

could find that ultimate flexural resistance on 0.4 L-section of side-span and middle-section of mid-span respectively was improved by 72.7% and 83% after steel plate and concrete composite strengthening, respectively. It shows that the reinforcement method effectively increases ultimate flexural resistance of section.

Theoretical Calculation of Key-section Resistance After Composite Reinforcement

Figure 6 shows calculation graphic expressions of ultimate flexural resistance of PC box girder after steel plate and concrete composite reinforcement. The calculation of ultimate flexural resistance is shown in Eqn. 1 and Eqn. 2.

Eqn. 1.

$$\alpha_1 f_c b'_f x + f'_{sy}A'_s = f_{spy}A_{spb} + 2f_{spy}A_{spw} + f_{py}A_p + f_{sy}A_s \tag{1}$$

Eqn. 2.

$$\begin{aligned} M_u = {} & f_{sy}A_s\left(h_{01} - \frac{x}{2}\right) + \psi_{sp} f_{spy}A_{spb}\left(h - \frac{t_{sp}}{2} - \frac{x}{2}\right) + 2\psi_{sp} f_{spy}A_{spw} + \left(h - \frac{h_{spv}}{2} - \frac{x}{2}\right) \\ & + f'_{sy}A'_s\left(\frac{x}{2} - a'_s\right) + f_{py}A_p\left(h_{02} - \frac{x}{2}\right) \end{aligned} \tag{2}$$

In Eqn. 1 and 2, α_1 is ratio of rectangular stress on compressive concrete and axial compressive strength design value. When concrete strength grade lower than C50, $\alpha_1 = 1.0$. When concrete strength grade is C80, $\alpha_1 = 0.94$. Linear interpolation is used between C50 and C80. What's more, A_s and A'_s are, respectively, section area of longitudinal tensile bar tensile area and compression area in original structure. A_p is section area of prestressed reinforcement. A_{spw} and A_{spb} are respectively section areas of lateral and bottom plate reinforced. f_c is axial compressive strength design value of concrete. f_{sy} and f'_{sy} are tensile strength and compressive strength design value of longitudinal bar in original structure. f_{spy} is tensile strength design value of plate reinforced. x is height of compressive concrete. h is section height of structure reinforced. h_{01} and h_{02} are respectively distant from the centre of tensile main reinforcement and prestressed reinforcement to the compressive upper-flange top in structure before reinforced. h_{spv} is real width of lateral plate reinforced. t_{sp} is the thickness of plate reinforced. b'_f is effective compressive width of lower-flange of box girder. ψ_{sp} is considered the effect of secondary load, tensile plate may not reach tensile strength design value lead to introduce reduction factor. When $\psi_{sp} \geqslant 1$, $\psi_{sp} = 1$.

The UBC of the key sections using the simplified formula is close to the finite element method.

Bearing Capacity Evaluation

Using software MIDAS, under ULS and considered partial coefficient of each load, effect of the most adverse load on 0.4 L-section of side-span and middle-section of mid-span is respectively 5 747 kN • m and 5 364 kN • m before reinforced in uplink viaduct, and is 6 899 kN • m and 5 776 kN • m after reinforcement. γ_0, the importance factor of structure, is 1.0. It can be seen that ultimate resistance on 0.4 L-section of side-span and middle-section of mid-span is far more than effect of the most adverse load under ULS. Especially, the girders adopted composite reinforced can greatly improve the safety margin of section. The girders can meet demand for section-resistance under ULS.

CONLUSIONS

To effectively simulating mechanical behavior of fire injured Yao Zhou Uplink Viaduct by ANSYS, it was to use respectively different reduction-factor of elastic modulus for concrete according to different burned degree. The load test results from each load condition showed that the measured-deflections of most measuring-points were less than the calculated value in main girder. Measured time-domain curves of structural vibration conformed vibration regularity of PC continuous girder bridge. It showed that structural stiffness and strength were improved efficiently after reinforcement, which satisfied the demand of design and operation safety. The statistics to monitoring date showed most vehicles load-effects monitored were less than design load-effects, and the partial measuring-points exceeded design value, which coincided with the theory of probability design. After using steel plate and concrete composite reinforcement and plate sticking reinforcement, force condition of girder was to get greatly improved. According to three stages of before fire, after fire, reinforced, it was analyzed deflection response of injury bridge under the most adverse moving-load. It could be seen that integral rigidity of the bridge after composite reinforced met the demand of code. Ultimate flexural resistances got by plastic finite element analysis and theoretical formulae showed that resistance on section after composite reinforced was far more than design-load effect and safety margin of bridge reinforced was obviously improved.

ACKNOWLEDGEMENTS

The writers would like to acknowledge the financial support provided by the Shaanxi Province Transportation Technology Research Projects (Grant No. 07-03k, 07-04k), the Special Fund for Basic Scientific Research of Central Colleges of the P. R. China, Chang'an University (Grant No. CHD2010JC003 and No. CHD2012ZD008), and China West Transportation Development Research Projects (Grant No. 200831849404, 20113185191410).

REFERENCES

[1] Nie, J. G., Zhao, J. and Tang, L., "Application of steel plate and concrete composite to strengthenning of reinforced concrete girder", Journal of Bridge Construction, 2007, (3), pp. 76-79. (in Chinese)

[2] Nie, J. G. and Zhao, J., "Experimental study on simply supported RC beams strengthened by steel plate-concrete technique", Journal of Building Structures, 2008, 29(5), pp. 50-56. (in Chinese)

[3] Wang, C. S., Yuan, Z. Y., Guo, X. Y., Gao, S. and Ren, T. X., "Flexural behavior experiment of reinforced concrete T-beams with steel plate-concrete composite strengthening", Journal of Traffic and Transportation

Engineering, 2010, 9 (6), pp. 21-29. (in Chinese)

[4] Wang, C.S., Gao, S., Ren, T.X. and Xu, Y., "Bending behavior experiment of damaged RC T-beams with steel plate and concrete composite strengthening", Journal of Architecture and Civil Engineering, 2010, 27(3), pp. 94-101. (in Chinese)

Proceedings of Seventh International Conference on Advances in Steel Structures, 2012, Nanjing, China

DUCTILITY EVALUATION OF STIFFENED STEEL PIPE-SECTION BRIDGE PIERS UNDER CYCLIC LOADING

* S. B. Gao[1] and Y. Li[1]

[1] Department of Civil Engineering, Shanghai Jiao Tong University, Shanghai, 200240, China
* Email: gao_sb@sjtu.edu.cn

KEYWORDS

Steel pipe-section bridge pier, cyclic lateral loads, longitudinal stiffeners, ductility capacity, hysteretic behavior, stiffeners' slenderness ratio.

ABSTRACT

This paper aims to investigate the ductility behaviour of the stiffened steel pipe-section bridge piers subjected to a constant vertical load and cyclic lateral loads. Different number of longitudinal stiffeners (four, six, and eight stiffeners) is set around the internal pipe section of the piers. The accuracy of the proposed finite element formulation is first verified by comparing the analytical results with two test results. Then, a series of parametrical studies are carried out to investigate the effects of radius-thickness ratio, different number of longitudinal stiffeners, and stiffeners' slenderness ratio on ductility behaviour of the stiffened bridge piers. It is found that compared with the un-stiffened bridge piers, the longitudinal stiffeners put a great effect on the ductility behaviour of the piers. The ductility is improved with the decrease in stiffeners' slenderness ratio and radius-thickness ratio of pipe section. Designing the bridge piers with high energy-absorption capacity can be achieved by setting eight longitudinal stiffeners.

INTRODUCTION

Modern seismic design philosophies require that the ultimate strength and ductility of steel bridge piers should be greater than the corresponding demands imposed by design earthquake motions. Steel bridge piers have been widely used in highway construction due to its light self-weight, high strength, fast and convenient construction, and so on. In the past decades, a few researches are carried out to un-stiffened steel pipe-section bridge piers (Gao et al.[1-2]; Goto et al.[3-4]). Gao et al.[1] proposed some formulas to predict the ultimate strength and ductility of un-stiffened piers. Goto et al.[3-4] compared the numerical analytical results with the test results of the un-stiffened steel pipe-section bridge piers to verify modified 3-surface plasticity model under bi-directional cyclic loading as well as seismic accelerations. As it is well known, steel pipe-section bridge piers are liable to locally buckle near the pier base under severe earthquake. To improve the seismic behavior of such steel bridge piers, Susantha et al.[5] placed a special compression member in the middle of the pier to take the axial load from the superstructure. Consequently, the influence of axial load on the inelastic buckling deformation of plates was well controlled. The ultimate strength, ductility and energy absorption capacities could be greatly improved.

Iura, et al.[6] proposed to set 3 and 4 longitudinal stiffeners inside the pipe section to strengthen the piers. The experimental studies showed that the ultimate strength was improved a little, while the ductility did not changed so much. Bao et al.[7] carried out a series of numerical analyses to the steel pipe-section piers stiffened by T-shaped stiffeners. They set the T-shaped stiffeners through the whole column height and evaluated the improved seismic performance efficiency based on the total weight of steel.

This paper aims to investigate the ductility behavior of steel pipe-section bridge piers stiffened by different number of longitudinal stiffeners. The piers are subjected to a constant vertical load and cyclic lateral loads. The accuracy of the proposed finite element formulation is verified by test results first. Then, a series of parametrical studies are carried out to investigate the effects of radius-thickness ratio, different number of longitudinal stiffeners, and stiffeners' slenderness ratio on ductility behaviour of the stiffened piers.

NUMERICAL ANALYTICAL METHOD

The analytical model of a cantilever steel bridge pier is shown in Figure 1. For thin-walled steel pipe-section columns subjected to a constant vertical load and cyclic lateral loads, local buckling usually occurs near the column base. To make an efficient model with least computing time, shell elements that can account for local buckling are employed to model the lower part of the column, while the upper part of the column is modeled with beam-column elements. As shown in Figure 1, four types of pipe-section piers with different number of longitudinal stiffeners are taken into consideration, and the longitudinal stiffeners are uniformly distributed around the pipe section. By try and error analysis, the length of the longitudinal stiffeners is assumed to be the diameter of pipe section from the column base because local buckling does not take place beyond it. It is not necessary to set the longitudinal stiffeners through the whole height of the column.

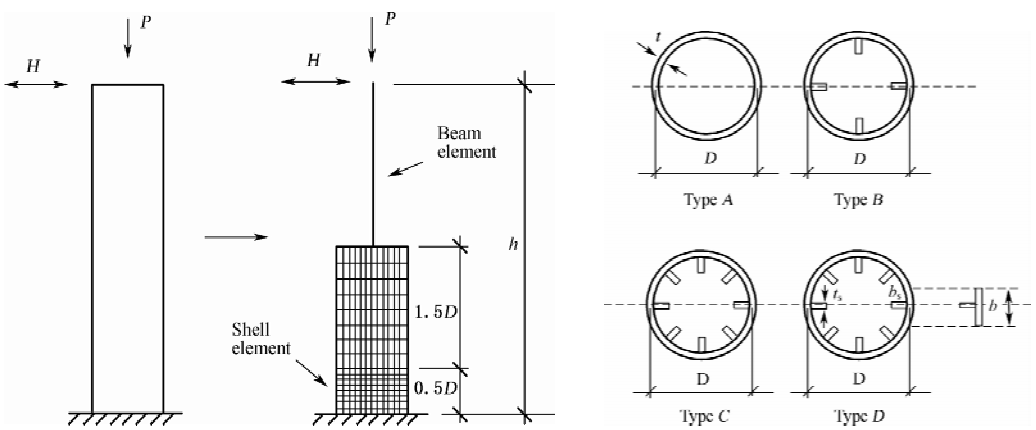

Figure 1 Stell pipe-section bridge pier

For the un-stiffened pipe-section piers, half of the column is modeled due to the symmetry of both geometry and loading (Gao et al.[1]). However, for the stiffened pipe-section piers, total analytical model is required because the longitudinal stiffeners located in the symmetry plane always result in non-symmetrical local buckling modes. Three meshes are divided along the width direction of longitudinal stiffeners in order to consider their local buckling behaviour. The same mesh division as the steel plate is adopted along the column height. In addition, a stiff plate with infinite bending stiffness is assumed in the

interface between the beam-column elements and shell elements.

The modified Newton iteration technique coupled with the lateral displacement control method is used in the analysis. The energy convergence criterion is adopted and the convergence tolerance is taken as 10^{-5}. The initial geometrical deflections and residual stresses are not taken into consideration.

Bi-linear stress-strain relationship is employed to consider the effect of strain hardening. The hardening modulus is assumed to be 1% of Young's modulus. The kinematic hardening model is employed as the steel constitutive law.

EXPERIMENTAL VERIFICATION

In order to verify the accuracy of the proposed numerical analytical method, two specimens named as No. 5 and No. 19 in Iura, et al.[6] are analyzed. The tested specimen No. 5 has 3 longitudinal stiffeners, while No. 19 with 4 longitudinal stiffeners. Figure 2 shows comparison of lateral load-lateral displacement curves obtained from both numerical analyses and tests. Figure 3 shows comparison of buckling modes of specimen No. 5 between analysis and test. It can be concluded that the analytical results of both lateral load-lateral displacement hysteretic curves and local buckling mode coincide well with the test results.

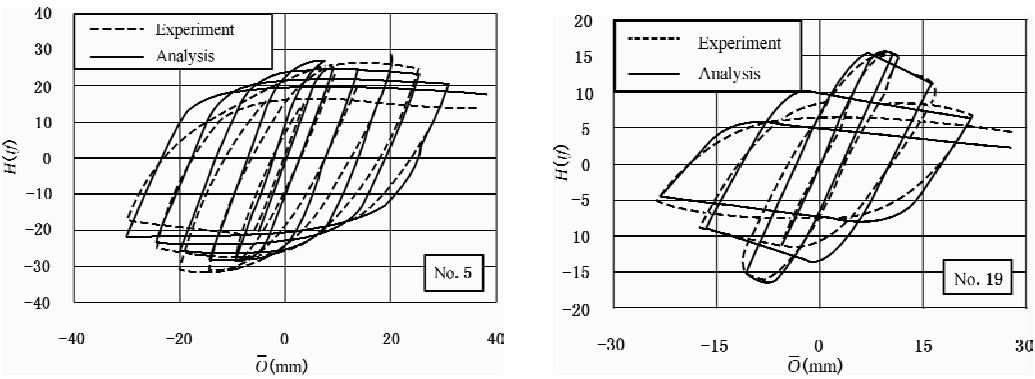

Figure 2 Comparison of lateral load-lateral displacement curves between analysis and test

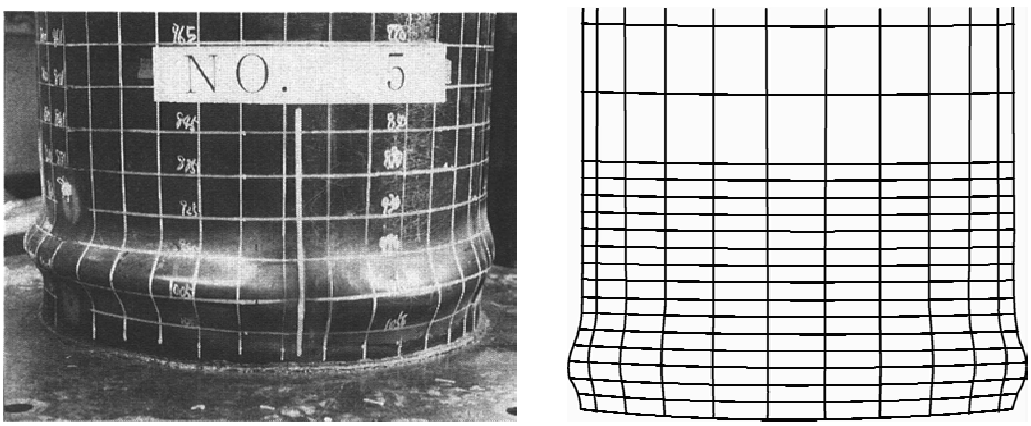

(a) Test (b) Analysis

Figure 3 Comparison of local buckling mode between analysis and test

PARAMETRICAL STUDIES

Radius-thickness ratio R_t, longitudinal stiffener's slenderness ratio $\bar{\lambda}_s$, and the number of longitudinal stiffeners around the pipe section are adopted as the main parameters in this section. Here, R_t is defined as follows.

$$R_t = \sqrt{3(1-\nu^2)}\,\frac{\sigma_y}{E}\cdot\frac{D}{2t} \tag{1}$$

in which, D = diameter of pipe section, t = plate thickness. The longitudinal stiffener's slenderness ratio $\bar{\lambda}_s$ is defined as follows.

$$\bar{\lambda}_s = \frac{1}{\sqrt{Q}}\frac{L_d}{r_s}\frac{1}{\pi}\sqrt{\frac{\sigma_y}{E}} \tag{2}$$

$$Q = \frac{1}{2R_f}[\beta - \sqrt{\beta^2 - 4R_f}] \leqslant 1.0 \tag{3}$$

$$R_f = \frac{b}{t}\sqrt{\frac{\sigma_y}{E}\,\frac{12(1-\nu^2)}{4\pi^2}} \tag{4}$$

$$b = 1.266\sqrt[4]{R_t l_x^2} \leqslant b_y \tag{5}$$

$$l_x/D = 0.585/R_t^{0.08} - 0.58 \tag{6}$$

in which, L_d = D = distance between two adjacent diaphragms, r_s = radius of gyration of a T-shaped cross section centered on one longitudinal stiffener, Q = local buckling strength of a plate enclosed by two adjacent diaphragms and stiffeners, $\beta = 1.33\ R_f + 0.868$, R_f = width-thickness ratio of steel plate, b = effective width of a T-shaped cross section (Chen[8]), b_y = distance between adjacent longitudinal stiffeners, l_x = elastic critical wavelength (Gao et al[9]).

Specimens P1, P2 and P3 are the un-stiffened steel piers, while the other 36 specimens are stiffened piers with different number of longitudinal stiffeners. These specimens are divided into 3 groups based on the value of R_t, where R_t is equal to 0.011 5, 0.085, and 0.06, respectively. In each group, four types of cross section, that is, no stiffeners, 4 stiffeners, 6 stiffeners, and 8 stiffeners, as shown in Figure 1, is considered. In order to investigate the effect of stiffeners' slenderness ratio, four kinds of stiffeners (i. e., 60×6 mm, 70×7 mm, 80×8 mm, 90×9 mm) for each type of stiffened cross section are taken into consideration. During the analysis, the specimens are subjected to a constant vertical load of $0.12P_y$ and prescribed lateral displacement history which consists of sequence of fully reversed displacement cycles, i. e., the displacement amplitude is increased stepwise after one cycle at each displacement level. The displacement increment adopted is the yield displacement, δ_y, corresponding to the applied constant axial load.

Effect of Radius-thickness Ratio

Figure 4 shows the envelope curves of lateral load versus lateral displacement obtained from the analyses with different radius-thickness ratio. The envelope curves are plotted by using the average value of lateral loads at both compressive and tension sides corresponding to each displacement amplitude. It is observed that the ductility capacity is improved with the decrease in radius-thickness ratio, no matter 4 or 8 longitudinal stiffeners are accounted for.

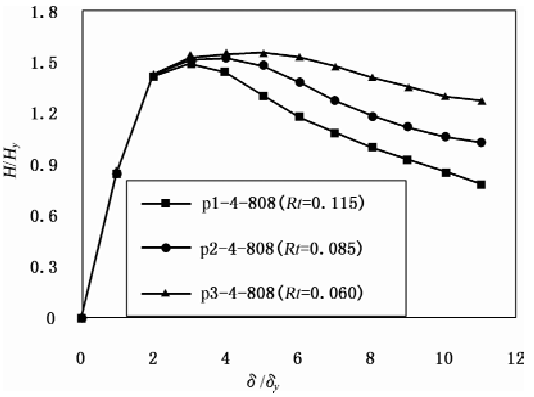

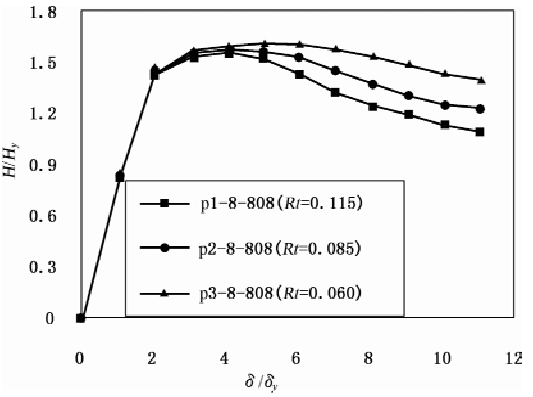

Figure 4 Effect of radius-thickness ratio

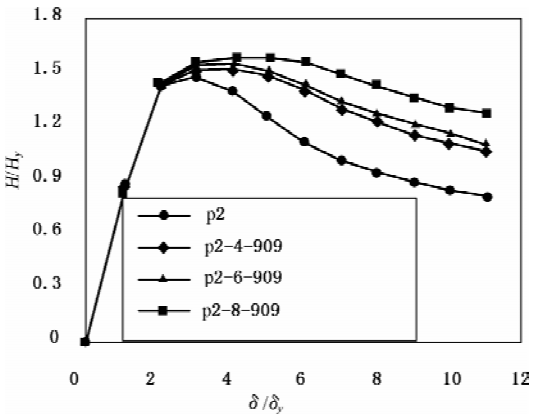

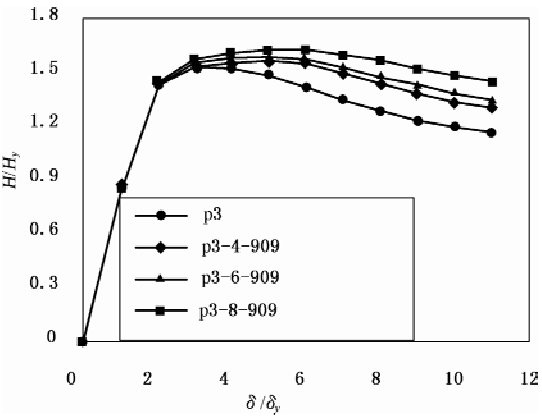

Figure 5 Effect of number of longitudinal stiffeners

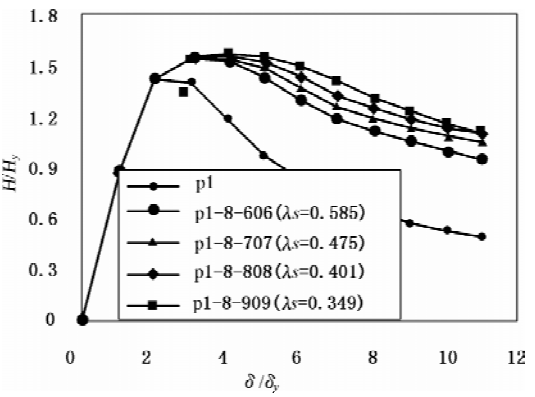

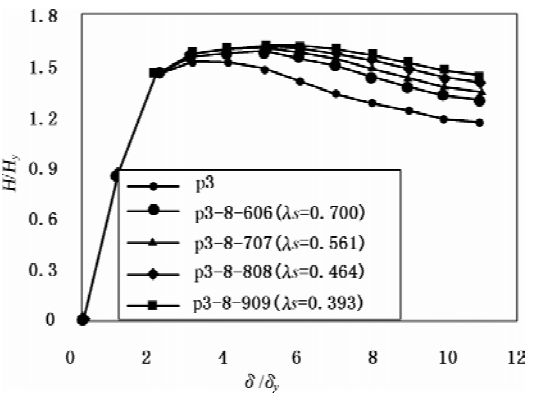

Figure 6 Effect of stiffeners' slenderness ratio

Effect of Number of Longitudinal Stiffeners

The envelope curves of lateral load versus lateral displacement with different number of longitudinal stiffeners are given in Figure 5. Compared with the un-stiffened bridge piers, the longitudinal stiffeners put a great effect on the ductility behaviour of the piers. However, almost the same load-displacement curves are observed in the case of 4 and 6 longitudinal stiffeners. The ductility capacity is obviously improved in the case of 8 longitudinal stiffeners.

Effect of Stiffeners' Slenderness Ratio

Figure 6 shows the envelope curves of lateral load versus lateral displacement curves with different stiffeners' slenderness ratio. It is observed that with the increase in stiffeners' slenderness ratio, the ductility capacity is reduced. Moreover, compared with P1 Series, the improvement of ductility capacity between P3 and P3 Series is not so obvious. The possible reason is that the pipe section of P3 is relatively thick, in which the bending stiffness provided by the stiffeners becomes relatively small.

CONCLUSIONS

The effect of longitudinal stiffeners on steel pipe-section bridge piers under a constant vertical load as well as cyclic lateral loads is investigated in this paper. Firstly, the accuracy of the proposed finite element formulation is verified by comparing the analytical results with two test results. Then, a series of parametrical studies are carried out to investigate the effects of radius-thickness ratio, different number of longitudinal stiffeners, and stiffeners' slenderness ratio on ductility behaviour of the stiffened piers. The main conclusions are summarized as follows.

(1) Compared with the un-stiffened bridge piers, the longitudinal stiffeners put a great effect on the ductility behaviour of the piers.

(2) The proposed formula to define the stiffeners' slenderness ratio is reasonable in evaluating the effect of longitudinal stiffeners on the ductility of the piers.

(3) With the increase in stiffeners' slenderness ratio, the ductility capacity is reduced.

(4) The longitudinal stiffeners can greatly improve the ductility behaviour of steel bridge piers. Therefore, designing the bridge piers with high energy-absorption capacity can be achieved by adopting longitudinal stiffeners. Moreover, 8 longitudinal stiffeners are recommended as a better choice compared with 4 or 6 longitudinal stiffeners.

Further parametrical studies are still needed in order to propose some useful formulas to predict the ultimate strength and ductility capacity of the stiffened pipe-section bridge piers.

ACKNOWLEDGEMENTS

The research work presented here is sponsored by research grants made available by Science and Technology Commission of Shanghai Municipality (No. 08PJ1406400), and by SRF for ROCS, SEM.

REFERENCES

[1] Gao, S.B., Usami, T. and Ge, H.B., "Ductility evaluation of steel bridge piers with pipe sections", Journal of Engineering Mechanics, ASCE, 1998, 124(3), pp.260-267.

[2] Gao, S.B. and Ge, H.B., "Numerical simulation of hollow and concrete-filled steel columns", An International Journal of Advanced Steel Construction, 2007, 3(3), pp.668-678.

[3] Goto, Y., Jiang, K. and Obata, M., "Stability and ductility of thin-walled circular steel columns under cyclic bidirectional loading", Journal of Structural Engineering, ASCE, 2006, 132(10), pp.1621-1631.

[4] Goto, Y., Muraki, M. and Obata, M., "Ultimate state of thin-walled circular steel columns under bidirectional seismic accelerations", Journal of Structural Engineering, ASCE, 2009, 135(12), pp.1481-1490.

[5] Susantha, K., Aoki, T. and Hattori, M., "Seismic performance improvement of circular steel columns using precompressed concrete-filled steel tube", Journal of Constructional Steel Research, 2008, 64, pp.30-36.

[6] Iura, M., Kumagai, Y. and Komaki, O., "Ultimate strength of stiffened cylindrical shells subjected to axial and lateral forces", Journal of Structural Mechanics and Earthquake Engineering, JSCE, 556/I-38, 1997, pp. 107-118.

[7] Bao, L., Liao, J. and Wang, Z., "Study on seismic performance of circular steel bridge piers with T-reinforcing rib", Journal of Shenyang Jianzhu University, 2010, 26(4), pp.665-669.

[8] Chen, S.F., "Guide to stability design of steel structures", China Architecture & Building Press, 2004, pp.332.

[9] Gao, S.B., Usami, T. and Ge, H.B., "Ductility of steel short cylinders in compression and bending", Journal of Engineering Mechanics, ASCE, 1998, 124(2), pp.176-183.

INNOVATIVE DESIGN AND APPLICATIONS OF U-SHAPED GIRDER IN BRIDGE ENGINEERING

* C.S. Wang, H.T. Li and G.F. Ren

Engineering Research Center for Large Highway Structure Safety of Ministry of Education, College of Highways, Chang'an University, Xi'an, Shaanxi Province, 710064, China
Key Laboratory for Bridge and Tunnel of Shaanxi Province, College of Highways, Chang'an University, Xi'an, Shaanxi Province, 710064, China
* Email: wcs2000wcs@163.com

KEYWORDS

Sustainable bridge, innovative design, U-shaped girder, railway bridges, light rail viaducts, urban viaducts.

ABSTRACT

U-shaped girder is a new type of through bridge suitable for railway bridges, light rail viaducts and urban viaducts for it has a slender deck slab and profiled edge beams result in both an economic and aesthetically pleasing structure. The application of U-shaped girder has more overseas applications and the domestic applications in China are not extensive. Compared with the traditional deck bridges, U-shaped girder bridges can greatly reduce the building height. Besides, when the bridge clearance is limited, especially in the interchanges, the usage of U-shaped girder can effectively reduce the height of the lines, thereby can reduce the use of land and to achieve better economic efficiency. Compared with the steel through bridges, using U-shaped girder has savings in steel along with noise reducing and easy maintenance. With the Low-cabin energy requirements and the promotion of human oriented design, U-shaped girder whose longitudinal top surface can be used as an emergency evacuation routes and prevent vehicles rushed off the bridge gets more and more attention as well as gradually received new applications. This paper aimed at extending the usage of U-shaped girder to railway bridges, light rail viaducts, urban viaducts and other modern urban transport infrastructure through the innovative conceptual design in order to promote the sustainable development of the modern transportation.

INTRODUCTION

U-shaped girder is a new type of through bridge suitable for railway bridges, light rail viaducts and urban viaducts. This new type of girder has more overseas applications such as Dubai Metro light rail viaducts, Paris Metro Line 13, Santiago Metro Line 5 in Chile, New Delhi Metro Line 3 in India and the Carpenter overpass in Britain while the domestic applications in China are not extensive[1-5].

At present, the metro lines usually are underground lines at downtown while often use elevated lines in urban functional area or suburbs and traditional elevated line has lots of difficulties in construction at urban sound sensitive zone. However, U-shaped girder itself forms a good noise canceling system and is suitable for elevated line in such zones for noise in the U-shaped girder will multiple reflected within the profiled edge beams and in this way, the amount of noise barrier is greatly reduced or even do not need to be added to the structure. Besides, sharing the approximately same construction and operating cost, using U-shaped girder in urban viaducts can melt into the environment and form an aesthetically pleasing structure. Recently, U-shaped girders are used in several cases in China.

The first application of U-shaped girder in China was along with the building of Shanghai Metro Line 8 which was designed with the help of the French company SYSTRA. Afterwards, Nanjing Metro Line 2 as seen in Figure 1 and Figure 2 used single line U-shaped girders design by BUEDRI in the elevated line part[3-4]. In May 6, 2010, the first piece of U-shaped girder design by BUEDRI was successfully hoisted in the construction of Chongqing Rail Transit Line 1 which marked that the U-shaped girder is gradually applying to bridge construction in China.

Figure 1 Application of U-shaped girder in Nanjing Metro

Figure 2 A close shot of U-shaped girder

The present U-shaped girder used in China is a kind of complex spatial beam-deck composite structure which shows apparent three-dimensional effect as well as complex coupling action in the biaxial bending and torsion of the deck slab under load action. The deck slab also participate in taking load together with the profiled edge beams which are designed with profiled vertical webs and top flanges to accommodate the emergency walkway and parapet arrangement on each side.

However, although there were applications in rail transit lines of China and several researches were made in aspects such as static analysis, train-track-bridge coupling vibration and fatigue performance[3-5], there was no mature design experience of this new kind of structure and there was no application in railway bridges and urban viaducts in the past decade. In order to promote the application of this new structure, the innovative conceptual design is necessary and urgent.

THE STRUCTURE CHARACTERISTIC OF U-SHAPED GIRDER

U-shaped girder is suitable for railway bridges, urban rail transit and urban viaducts. Compared with commonly used bridges such as PC-box girder bridges, U-shaped girder has many advantages. The structure characteristic of U-shaped girder can be summarized as follows:

(1) Compared with traditional deck bridges (i.e., box girder bridges and T-beam bridges), U-shaped girder bridge is a new type of through bridge and can significantly reduce the height of the line's elevation along with engineering volume reducing and investment decreasing.
(2) U-shaped girder itself forms a good noise canceling system for noise in the U-shaped girder will multiple reflected within the profiled edge beams and in this way, energy will be attenuated.
(3) The top flanges of the profiled edge beams which are designed at the same height of the deck of light rail train can be used as the emergency walkway. Meanwhile, thanks to the profiled vertical webs in both sides of the U-shaped girder, vehicles are protected and the structure can be designed without or with less consideration of setting traditional anti-collision components.
(4) For vehicles are running in the U-shaped girder, the amount of noise barrier of urban viaduct is greatly reduced or even do not need to be added to the structure.
(5) The deck slab of U-shaped girder possesses of advantages of low building's height which is only about one-sixth of a box girder at the same span. Besides, the slender deck slab and the profiled edge beams result in both an economic and aesthetically pleasing structure.

INNOVATIVE DESIGN OF THE U-SHAPED GIRDER

Single-Line and Simply-Supported U-Shaped Girder Bridge

Single-line (also known as single-track) U-shaped girder as shown in Figure 3 and Figure 4 is a kind of bridge that only allows one vehicle (i.e., automobile, train and metro vehicle) running in the U-shaped girder at one time and it is especially suitable for railway bridges. As compared with truck load, train load is much larger and using single-line bridges would cause no action of bias load and leads to less partial load problem. Besides, owing to the single-line bridge, the width of the deck is reduced which cutting the usage of earthwork quality and provides the basis of the application of full-span precast and launching construction method. In addition, as is known to all, mechanical devices such as bearings, expansion joints, etc. require regular maintenance and need partial or full replacement several times during the bridge service life and this may cut the railway line as well as the train was delayed. However, the bearings or expansion joints of the two lines can be maintained or replaced separately by using single-line girder bridges and in this way, trains can go through the bridge while the other line is under maintenance or replacement.

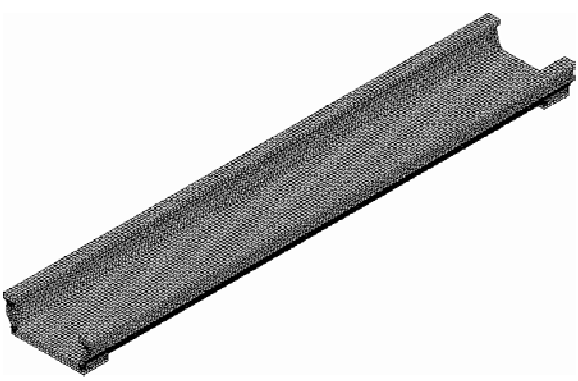

Figure 3 Finite-element model of a single-line girder.

Figure 4 Cross section of U-shaped girder.

Using full-span precast and launching construction method for Single-line U-shaped railway girder bridges was perhaps an obvious choice to achieve rapid construction with minimum noise pollution and environmental disruption. Forms a good noise canceling system for noise, the U-shaped girder can reduce noise disruption and it is suggested that using U-shaped girder in urban railway viaduct bridges can lead an aesthetically pleasing alone with less visual impact view of the structure.

Double-Line Simply-Supported U-Shaped Girder Bridge

Double-line U-shaped girder bridges can be used widely in urban viaduct and light rail viaducts and so on. Similar as single-line U-shaped girder bridges, the double-line ones share the same merits of noise reducing and investment decreasing. Moreover, as the vehicle flow-rate of some major interchanges is usually very large, approach bridges of overpasses are often designed as double-line or more. Thus, double-line U-shaped girder bridges can satisfy its needs as well as reduce noise pollution, cut or eliminate the use of sound barriers and protect the automobile from dropping off. Figure 5 and Figure 6 show a view of double-line U-shaped girder bridges.

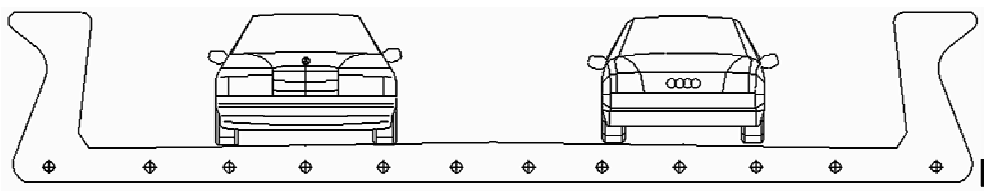

Figure 5 Typical section for urban viaducts

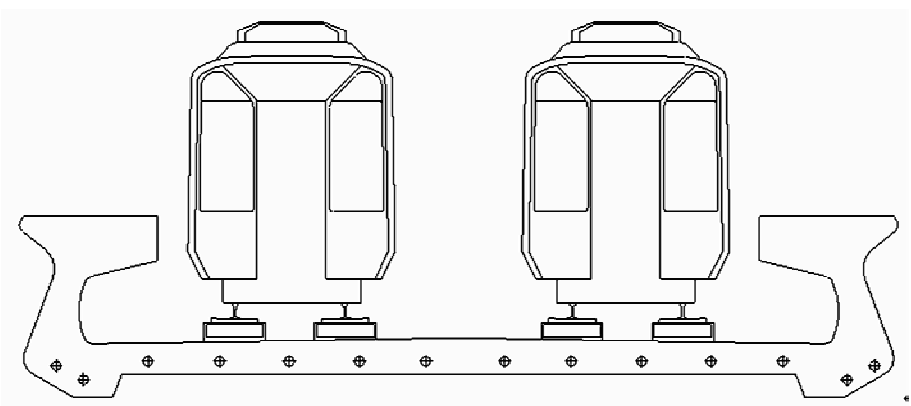

Figure 6 Typical section for light rail viaducts.

This kind of U-shaped girder bridges which often with deck slabs about 10 meters wide were usually constructed by the precast segmental construction method. However, the greater width of the deck slab leads to a greater weight per meter of the structure than the single-line bridges, in this way the full-span precast and launching construction method is no longer available for this type of bridge. However, in order to achieve rapid construction with less interference with the traffic, precast segmental construction method with the help of overhead gantries to erect the segments as indicated schematically in Figure 7 is the suitable choice[1-2].

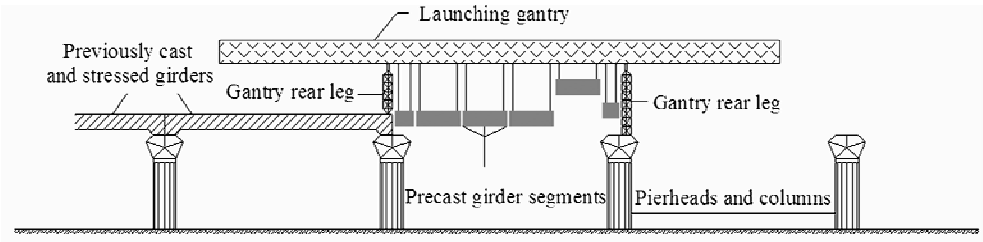

Figure 7 Precast segmental construction method.

Steel and Concrete Composite U-Shaped Girder Bridge

As indicated in Figure 8, this type of U-shaped girder bridges has concrete casted at the interior of the steel-concrete U-shaped section's steel parts prefabricated from steel plates. Besides, the steel plates and the concrete are integrated through shearing connectors and work together with each other.

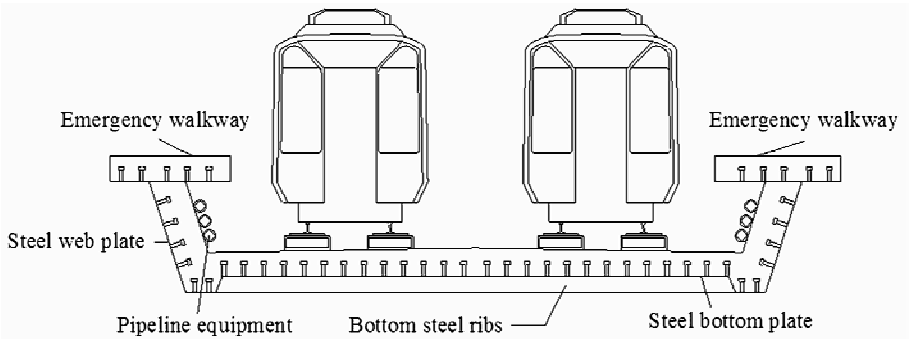

Figure 8 Typical section of composite U-shaped girder.

While inheriting the characteristics of traditional U-shaped girder, this type of structure possesses its unique advantage as steel plates may substitute the formwork, the construction may proceed with few or no formwork. Besides, the tensile strength of the steel bottom plate can be made full use of both in the transversal and the longitudinal directions. In this way, the fabrication of the structure, including make the assembling, welding of reinforcement, and the transversal tension of the prestressing tendon can be greatly simplified.

In addition, nowadays, as the construction of High Speed Railway is booming up in China with the train's speed growing up to 200 km/h, the safety issue of derailment should be much more concerned. Just on July 23, 2011, four carriages of D3115 and D301 derailed and drop off the bridge. However, as the profiled vertical webs which wrapped with steel plates of the U-shaped girder can protect vehicles from dropping off and provides protection from impact, the consequence of the accident would not been that hurts if had used this kind of structure. Figure 9 gives a finite-element model segment of a steel and concrete composite U-shaped girder bridge and a kind of stiffener of the bottom plate is shown as well.

Through a preliminary finite element analysis, Tsinghua University indicated that the parameters of the section have different impacts on the performance of the structure. Comparing with others, the width of

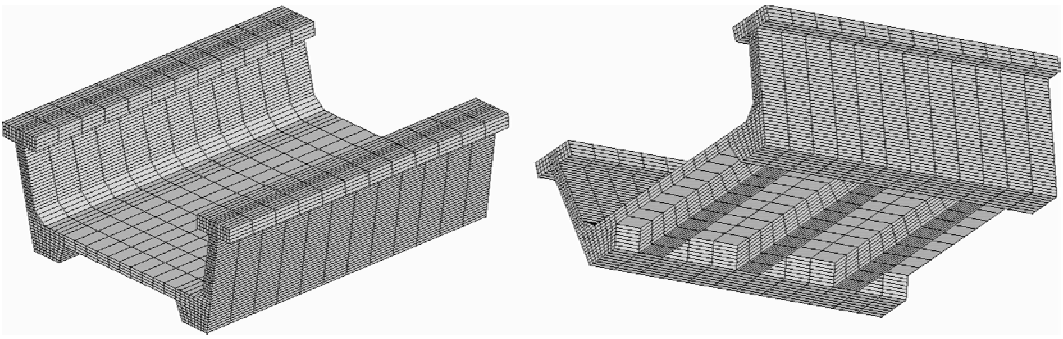

Figure 9 Finite-element model segment of a typical steel and concrete composite U-shaped girder.

the longitudinal rib of the bottom concrete, the flange thickness and the web height of the concrete are relatively more sensitive factors. In addition, temperature and contraction, creep of the concrete also have much influence on the structural behavior and shear lag is exhibited to some extent for the longitudinal middle-plane stress distribution along the direction of width of the bottom panel of the steel girder and concrete under the vertical loads[6]. In addition, a static test of a two-point symmetric loading was conducted on a simply supported single-line steel-concrete composite U-shaped girder model of 1∶3 sectional scale and 1∶4 length scale and experimental results reveals that steel plates work together well with the concrete integrated through shear stud connectors. The U-shaped girder model exhibited a bending failure mode. The lateral transversal displacements of the upper beam flange near the supports were outwards against the section center. On the contrary, the middle part of the girder went inwards, and the transversal displacements were much smaller than the vertical deflections at the mid-span, which revealed the section type of the model performs well in torsion[7].

Continuous U-Shaped Girder Bridge

For situations where longer spans (say, 50 m) are required, the U-shaped girder can be made continuously by stitching together individual spans after erecting them as simply supported. In the meanwhile, balanced cantilever construction method or the conventional falsework type construction method can also be used in building this type of U-shaped girder bridges. Figure 10 gives a view of double-line continuous U-shaped girder bridge.

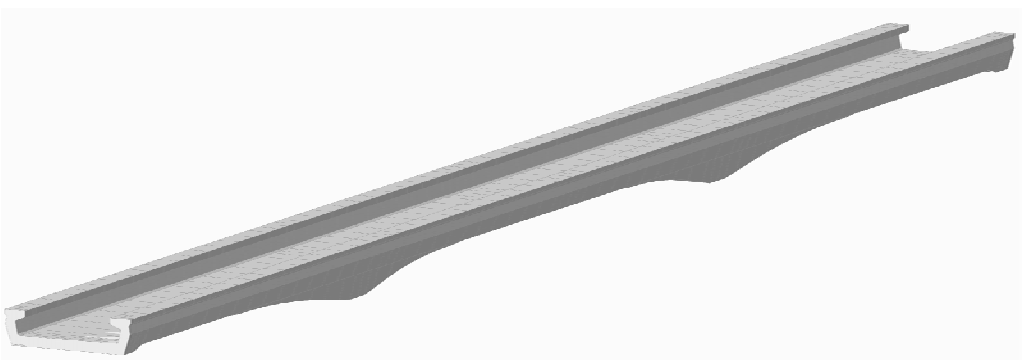

Figure 10 A case of continuous U-shaped girder bridge.

SUMMARY

Compared with commonly used bridge structures say PC-box section girder, U-shaped girder, which is a new type of through bridge that has merits of noise reducing, impact protection, building height lowing, aesthetically pleasing, Low-carbon energy using as well as environmental friendly is suitable for railway bridges, light rail viaducts and urban viaduct. This paper has provided a brief innovative conceptual design of different kinds of U-Shaped girder bridges and showed a glimpse of applications both in China and overseas. Most importantly, the author hopes to inspire engineers to apply this innovative type of structure in railway bridges and urban viaducts construction along with urban rail transit.

ACKNOWLEDGEMENTS

This work was financially supported by the Program for New Century Excellent Talents in University of the Ministry of Education of the P. R. China (Grant No. NCET－07－0121), the China West Transportation Development Research Projects (Grant No. 20113184901030) and the Special Fund for Basic Scientific Research of Central Colleges, Chang'an University (No. CHD2009JC166).

REFERENCES

[1] Smith, D.A., Hewson, N.R. and Hendy, C.R., "Design of the Dubai Metro light rail viaducts-superstructure", Proceedings of the Institution of Civil Engineers—Bridge Engineering, 2009, 162(2), pp.55-62.

[2] Smith, D.A. and Hendy, C.R., "Design of the Dubai Metro light rail viaducts -substructure", Proceedings of the Institution of Civil Engineers—Bridge Engineering, 2009, 162(2), pp.63-74.

[3] Li, Q., "Structural Calculation and Experiment of U-beam in Nanjing Metro Line 2", Urban Mass Transit, 2009, 8, pp.8-12.

[4] Wang, C.S., "Fatigue test of the full size U-Shaped girder for Nanjing Metro Line 2", Chang'an University, 2008.

[5] Zhang, X., Li, X.Z. and Li, Y.D., "Dynamic Characteristics Study of U-beam Applied in Rail Transit", Advanced in Civil Engineering and Architecture, 2011, 243-249, pp.2021-2026.

[6] Nie, J.G., Wu, L.L., Fan, J.S. and Lv, J.F., "Preliminary study of channel steel-concrete composite beam and application", China Civil Engineering Journal, 2008, 41(11), pp.78-85.

[7] Wu, L.L., Nie, J.G., Lv, J.F. and Fan, J.S., "Experimental study of simply supported channel steel-concrete composite beams", China Civil Engineering Journal, 2011, 44(3), pp.39-48.

THE EXPERIMENTS ON BOND LENGTH OF CFRP LAMINA UNDER THE EFFECT OF HIGH TEMPERATURE ENVIRONMENT

B.T. Huang[1], *X. Yuan[2,3], S.T. Song[2]

[1] College of Civil Engineering & Architecture, Jiang Su University of Science and Technology, Zhenjiang, 212003, China
[2] College of Civil Engineering, Southeast University, Nanjing, 210096, China
[3] College of Civil Engineering, Panzhihua University, Panzhihua, 617000, China
* Email: yuanxin9988@163.com

KEYWORDS

High temperature effect, CFRP, concrete, SMA, bond length.

ABSTRACT

In the influence of the frequent drought and tropical cyclone such as various climate disaster in Bangladesh, as the surface temperature stress which lead to the Bangabandhu bridge deck appear longitudinal crack. Epoxy resin on the Bangabandhu bridge is made after the restoration. The cracks have been in bridge roof, slab, the box beam webs, which is adjustable seam (hinge) in the early part of the project. The preliminary design for the bridge deck crack is to coat carbon board in transverse in order to constraint the longitudinal cracks development. The level up layer, waterproofing, insulating layer and 5 cm thick Matrix Asphalt (SMA), a wear protection layer and providing corrosion resistant layer. It is the first time so large area CFRP lamina is pasted on bridge panel and the construction of Matrix Asphalt layer in the world. In order to research the rationality of the design scheme and durability of new part after reinforcement of CFRP lamina on multi-function box girder-bridge under the environment of high temperature. The effective simulating test is necessary made to study the bond length of CFRP lamina reinforcement on multi-function box girder-bridge under the environment of high temperature according to the design scheme. According to the test the factors affecting CFRP bond length is analysed. The rational length of CFRP is suggested under high temperature effect. The study on reasonable and effective bond length of CFRP is made under the environment of high temperature CFRP reinforcement multi-function box girder-bridge.

OVERVIEW

With CFRP reinforced concrete structure of the widely used, it will involve CFRP and concrete bonding problem, bond section holds transfer load. Because of there is greater stress concentration in bonded paragraph, the reliability of the phenomenon which ensure the overall structure of normal use of

premise. The CFRP reinforced concrete structure sheet repair technical specification CECS146 provisions of CFRP sheet bond length should be not less than 100 mm[1]. At present our country of CFRP board binding test little study on asphalt high temperature effect of the CFRP successfully after placing board and concrete bonding research, this paper first study Bangabandhu bridge reinforcement design as the background, the experimental research on CFRP plate and concrete in different bond length under the high temperature function of asphalt paving.

In the influence of the frequent drought and tropical cyclone such as various climate disaster in Bangladesh, as the surface temperature stress which lead to the Bangabandhu bridge deck appear longitudinal crack. Epoxy resin on the Bangabandhu bridge is made after the restoration. The cracks have been in bridge roof, slab, the box beam webs, which is adjustable seam (hinge) in the early part of the project. The preliminary design for the bridge deck crack is to coat carbon board in transverse in order to constraint the longitudinal cracks development. The level up layer, waterproofing, insulating layer and 5cm thick Matrix Asphalt (SMA), a wear protection layer and providing corrosion resistant layer. It is the first time so large area CFRP lamina is pasted on bridge panel and the construction of Matrix Asphalt layer in the world. In order to research the rationality of the design scheme and durability of new part after reinforcement of CFRP lamina on multi-function box girder-bridge under the environment of high temperature. The effective simulating test is necessary made to study the bond length of CFRP lamina reinforcement on multi-function box girder-bridge under the environment of high temperature according to the design scheme. According to the test the factors affecting CFRP bond length is analysed. The rational length of CFRP is suggested under high temperature effect. The study on reasonable and effective bond length of CFRP is made under the environment of high temperature CFRP reinforcement multi-function box girder-bridge.

Test Materials and Devices

CFRP thickness is compared commonly thin, which can ignore the fillet normal stress. From the circle turn from the shear rubber τ-gamma curve found that there exist certain adhesive plastic zone can be approximately think fillet, elastic and plastic materials for ideal[2].

CFRP sheet come form Nanjing extension of the production of the company the board, adhesive is used in CFRP successfully into production building structure adhesive, CFRP plate and structure adhesive basic mechanical properties are shown in Table 1 and Table 2.

TABLE 1 MAIN PERFORMANCE INDEX CFRP

thickness(mm)	Longitudinal strength (MPa)	Tensile modulus (GPa)	Elongation at break (%)
1.4	≥2 300	≥150	≥1.4

TABLE 2 MAIN PERFORMANCE INDEX OF CFRP ADHESIVE

model	Tensile strength (MPa)	Tensile elastic modulus (MPa)	Bending strength (MPa)
K－801	≥25	≥2 500	≥30

The use of a single specimen because of concrete structure binding rules has no corresponding test standards, specimen design and production according to the tensile shear strength test method of adhesive GB 7124-86 and[3, 4], CFRP plate and concrete bonding between respectively for 100 mm width, 200 mm

and 300 mm. Strain acquisition instrument TDS-the 530 strain test system, specimens form is shown in Figure 2.

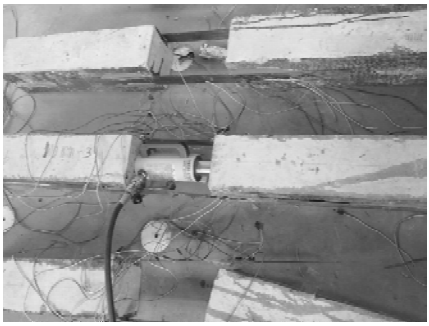

Figure 1 Test device figure

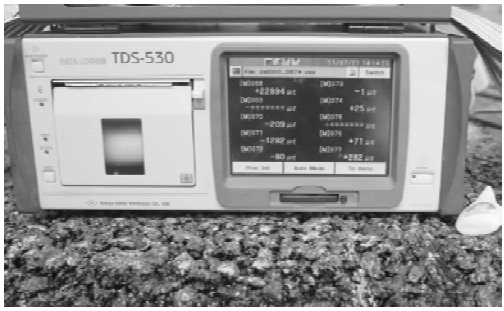

Figure 2 TDS strain acquisition system

TEST RESULTS AND THE ANALYSIS

Damage Loads and Damage Form

CFRP and concrete binding destructive load value in Figure 3, from the destructive form, it can be seen classified as three typical failure modes: the bonded FRP tensile, this kind of near mainly due to the damage of the materials tensile strength is insufficient; dissection of the destruction of this kind of destruction, mainly because of lack of shear stress, including the interface of the fillet cohesion damage and CFRP and fillet interface destruction; interface stripped after a break, CFRP of this kind of destruction in interface stripping destruction and materials tensile failure of a critical interval. CFRP specimens with concrete binding the damage form of the three kinds also belong to.

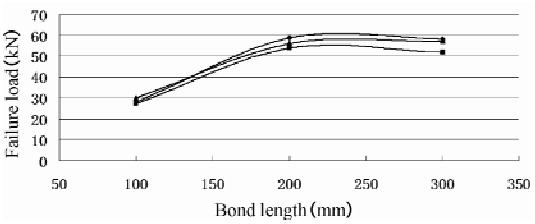

Figure 3 Failure load with bond length for CFRP SLAB

It is given the same kind of CFRP board load ratio (the bond length load value than the last 100 mm load value) and the bond length relationship after high temperature effect of the asphalt in Figure 4. 100 mm to the concrete short bond with CFRP specimens, destroy major damage, destroy stripping because interface, with low load the increase of the bond length, damage was improved, and the load mainly due to the damage caused by insufficient strength of materials CFRP tensile failure. In Figure 4 can see, the bond length 200 mm of the bond length is 100 mm bond specimen improve more than two times, the bond length 200 mm in the destruction of the maximum load when, compared with 100 mm bond specimen increased by 211%, more than 200 mm in the tendency of increase after no load, in 200 mm and 300 mm when the bond length fluctuation, that more than smaller load must be the bond length, length increases

cannot be effectively improve the bearing capacity, namely over a certain bond length by CFRP board tensile control load basic unchanged.

More than 200 mm in the bond length damage down a bit due to load is construction technology, test environment, CFRP board materials and adhesives factors such as performance. At the same time to illustrate the CFRP plate and concrete the bond length and adhesives, CFRP material performance and construction technology and so on.

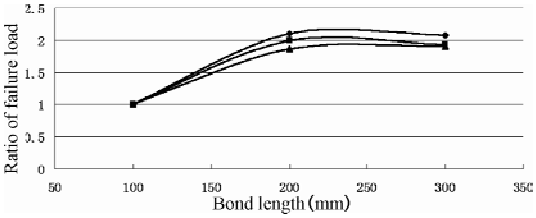

Figure 4 Ratio of failure load with bond length for CFRP SLAB

Interface Shear Stress

Because of the thickness of the CFRP is small, it can be seen the upper plate and the lower plate only transfer between shear stress[5]. According to the determination of the load at all levels CFRP panel by CFRP tensile strain, the stress of the balance sheet get near I short distances interface shear stress average[6]:

$$\tau_i = \mathrm{E}_F t_F \frac{(\varepsilon_i - \varepsilon_{i-1})}{\Delta x}$$

formula: ε_i and ε_{i-1} for CFRP panel i and $i-1$ point of strain; Δx for point i and $i-1$ the distance between them; E_F and t_F respectively for CFRP panel modulus of elasticity and thickness; τ_i for i point of shear stress.

According to the calculation of the bond length in different load shear stress, CFRP specimens of bonding shear stress distribution is shown in Figure 5 to Figure 7. By tests by the shear stress distribution in the bond length are nonlinear, the bond between the distributions of regional shear stress larger regional shear stress, edge is smaller. CFRP plate with concrete the bond length is hours at the end of destruction, stripping happened with the increase of the bond length, when the bond length of more than 200 mm,

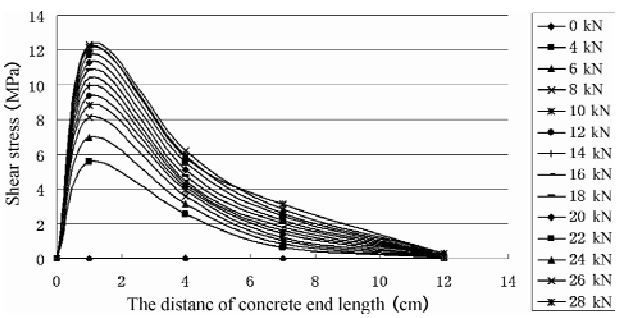

Figure 5 CFRP and concrete binding length is 100 mm

edge regions must length of shear stress in gradient is very small. According to the concrete bonding between the CFRP and stress distribution, CFRP specimens of effective bonding bond length about 200 mm or so.

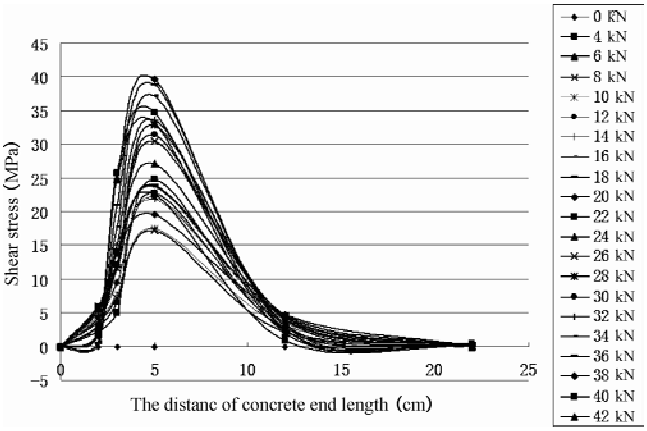

Figure 6 CFRP and concrete binding length is 200 mm

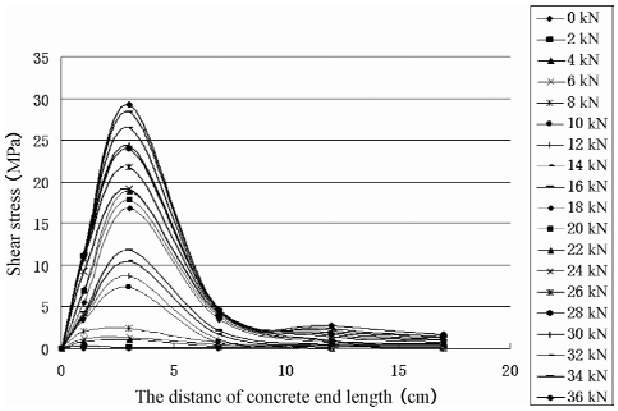

Figure 7 CFRP and concrete binding length is 300 mm

CONCLUSION

From the CFRP and concrete binding test, it can reach the following conclusion:
It can be seen that the CFRP and concrete binding ability and bond colloid parameters, CFRP material parameters and construction process parameters. Through the test of the interface stress of CFRP transfer can see, paving asphalt concrete under high temperature effect with CFRP can effectively the bond length about 200 mm or so.

It can be seen that in high temperature under the role of CFRP plate with concrete binding length, the maximum shear stress area seen in the area at the end of the binding, and the bond length corresponding to a critical area, more than the critical regions, CFRP plate and concrete after the bond length of the increase will no longer improve the bearing capacity of the bond.

REFERENCES

[1] China Engineering Construction Standardization Association. CECS146, 2003, Technical specification for strengthening concrete structures with carbon fiber reinforced polymer laminate, Beijing, China Planning Press, 2003.

[2] Wang, Y. B. and Zhang, Q. C., "Constructure joints of composites materials", Beijing: National Defence Industry Press, 1992. (in Chinese)

[3] Parvathy, U., "Behaviour of FRP-to-FRP and FRP-to-concrete bond", Canada, University of Toronto, 2003.

[4] Homam, S. M., "Fibre reinforced polymers (FRP) and FRP-concrete composites subjected to various loads and environmental exposures", Canada, University of Toronto, 2005.

[5] Her, S. C., "Stress analysis of adhesively-bonded lap joints", Composite Structure, 1999, 47 (1), pp.673-678.

[6] Li, G. and Sullivan, P. L., "Finite element and experimental studies on single-lap balanced joints in tension", International Journal of Adhesion and Adhesives, 2001, 21(3), pp.211-220.

SEISMIC ANALYSIS ON EXTRA-DOSED CABLE-STAYED BRIDGE WITH CORRUGATED STEEL WEB PC COMBINED BOX GIRDER

* Y.R. An[1], S. Zeng[2], G. Zheng[3]

[1, 3] Chongqing Communications Research & Design Institute Co. Ltd, China Merchants Bureau, Chongqing, China

[2] School of Civil Engineering & Architecture, Chongqing Jiaotong University, Chongqing, China

* Email: anyongri@cmhk.com

KEYWORDS

Corrugated steel web, extra-dosed cable-stayed bridge, seismic analysis.

ABSTRACT

Although the impact of changing of bridge pier' stiffness for girder inner force of corrugated steel web PC combined box girder extra-dosed cable-stayed bridge is little. But the seismic response characteristics of the bridge is different. For the aims of finding the seismic response characteristics of the bridge. Firstly, used the software of Midas to analyse two kinds of corrugated steel web PC combined box girder extra-dosed cable-stayed bridge, in which, the one's pier is rigid and the other is flexible as the forms of pier are hollow and double thin-wall pier to study the force changes on the pier and girder of the bridge. Secondly, through analysing the double thin pier wall corrugated steel web PC combined box girder extra-dosed cable-stayed bridge as the tower height changed from 31.4 m to 44 m under the force of earthquake, we can find it is remarkable that the impact on the bridge pier, girder and tower as the system of bridge changed from extradosed cable-stayed bridge to cable-stayed bridge. Finally, compared with the results of analysis, can we confirm the most appropriate structure system parameters for the bridge. The study of the paper provide reference for bridge engineers in China when they design the corrugated steel web PC combined box girder extra-dosed cable-stayed bridge in the earthquake area.

INTRODUCTION

Compared with traditional box girder structure, corrugated steel web PC-concrete composite box girder has a series of advantages such as light weight, cross ability, convenient construction, pre-stressed transfer high efficiency etc. This combination structure originated in France, and has been widely used in Japan[1-4].

In China, By the beginning of 1998 the study on the mechanics characteristics with the design and construction work of the corrugated steel web PC combined box girder had been carried off. In 2005, the

first domestic corrugated steel web composite PC continuous box girder pedestrian bridge had been completed which named long march bridge. By 2010, China has built 13 bridges, including 22 bridges under construction[5-7].

However, these bridges are simply supported beam, continuous rigid frame, while the span reaches to a certain extent they will be uneconomical. The corrugated steel web PC combined box girder extra-dosed cable-stayed bridge has a greater across capacity at the same height of the girder, especially those bridges which span are between 130 m and 200 m will be more competitive in mountain area. In China, no relevant researches on corrugated steel box girder webs PC extra-dosed cable-stayed bridge have been done, a lot of stress situations are uncertain. Therefore, basing on the corrugated steel box girder webs PC extra-dosed cable-stayed bridges has this paper analyzed the structure changing pier and tower height by the method of Time History Analysis. This paper compared with the internal force distribution in the structure, the longitudinal and transverse displacement at the tower top, and analyzed the structure stress characteristics.

CALCULATION MODEL

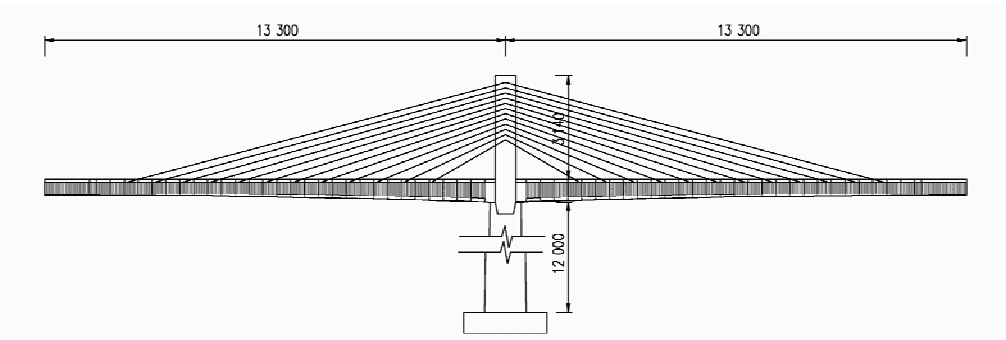

Figure 1 Layout of bridge

As Figure 1 and Figure 2 showed, bridge span is 133 m + 133 m. The stay cable is fan-shaped single cable plane. The cable distance is 8 m on girder and 1.5 m on tower. The girder which at the pier top used PC, and the other used corrugated steel web PC combined box girder. The height of girder changes from 4.5 m at closure to 6.5 m at pier top according to the rule of second-degree parabola. Pier's height is 120 m, and the pier's section size is showed in Figure 3. Longitudinal section length changes from 1 210 cm at the pier bottom to 900 cm at the pier top according to the rule of second-degree parabola, and transverse section width is 900 cm.

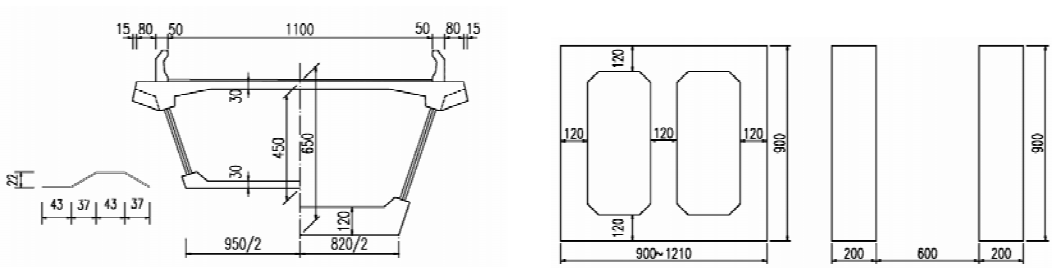

(a) Girder and corrugated steel webs section (b) Pier section

Figure 2 Section form and sizes

The paper adopts Midas to calculate. Pier, tower and girder all adopt girder element, while stay cables adopt truss element. Material parameter and boundary conditions are respectively showed in Table 1 and Table 2.

TABLE 1 BOUNDARY CONDITIONS

Position	*Dx*	*Dy*	*Dz*	*Rx*	*Ry*	*Rz*
Pier bottom	1	1	1	1	1	1
Girder tip	Damp	1	1	1	0	0

In Table 1, *Dx*, *Dy*, *Dz*, *Rx*, *Ry*, *Rz* are translational and rotational degrees of freedom of x-direction, y-direction, and z-direction respectively. "0" -freedom,"1" - constraint, "Damp" -damper.

TABLE 2 MATERIAL PARAMENTERS

Position	Material	Remarks
Pier and pile cap	C40	
Tower and girder	C50	
Corrugated steel webs	Q345C	$t = 12 - 24$ mm
Cable	Steel wire	$f_{pk} = 1\,670$ MPa

In Table 2, t is thickness of corrugated steel webs, f_{pk} is material standard strength.

Time History Analysis adopts immediate integration, time step is 0.02 s, and total analysis time is 200 s. Structural damping adopts Rayleigh damping, at the end of girder set viscous damper along the length direction respectively, and mechanics formula is showed as follows.

$$F = CV^{\xi} \tag{1}$$

In Eqn. 1, *F*-damping force, *C*-damping coefficient, *V*-Velocity, ξ-damping exponent. In the paper, the value of *C* is 2 000 and the value of ξ is 0.2.

Schedule acceleration load combination adopts the combination mode of longitudinal or traverse adding vertical. Vertical ground acceleration is 0.5 times of the level ground acceleration[8]. Selected 2 seismic waves, E1 and E2 are showed in Figure 3, the return period of E1 is 100 yeas, and the biggest ground acceleration is 66 cm/s^2, while the return period of E2 is 475 yeas, and the biggest ground acceleration is 144 cm/s^2.

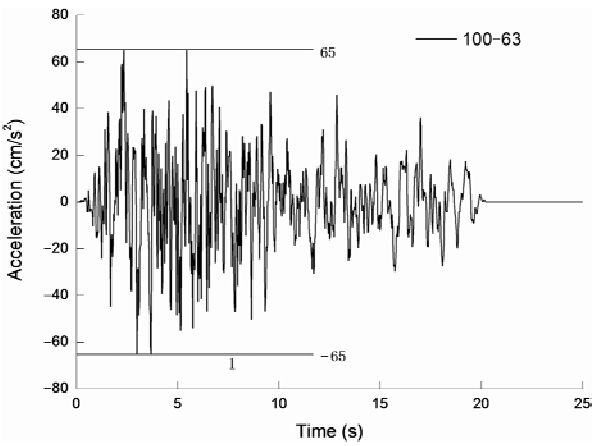

(a) E1 Seismic wave

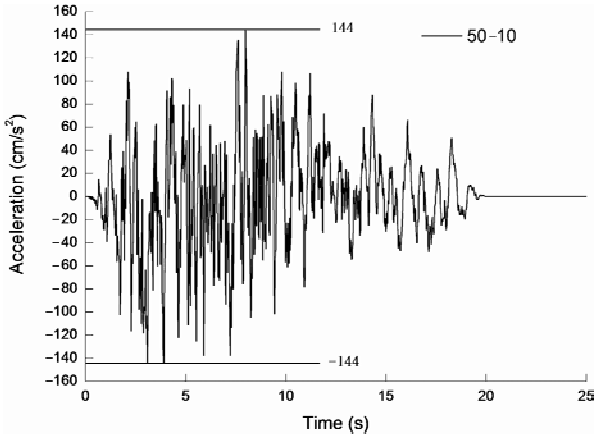

(b) E2 Seismic wave

Figure 3 Seismic wave

As Table 3 showed, built 4 models in all. The form of model's pier is hollow section and height-span ration is 1/7. The forms of model 2 to 4's piers are double thin-wall and height-span ratios are respectively 1/5, 1/6, 1/7. The finite element models are showed in Figure 4. In this paper, as calculation model has only side span, when calculates the height-span ratio, side span is equal to 0.6 times of main span, so the equivalent main span is about 220 m.

TABLE 3 STRUCTURE ANALYSIS MODEL

Model	Pier	Equivalent span	Tower height	Height-span ration
1	Hollow pier	220 m	31.4 m	1/7
2	Double thin-wall	220 m	44.0 m	1/5
3	Double thin-wall	220 m	36.7 m	1/6
4	Double thin-wall	220 m	31.4 m	1/7

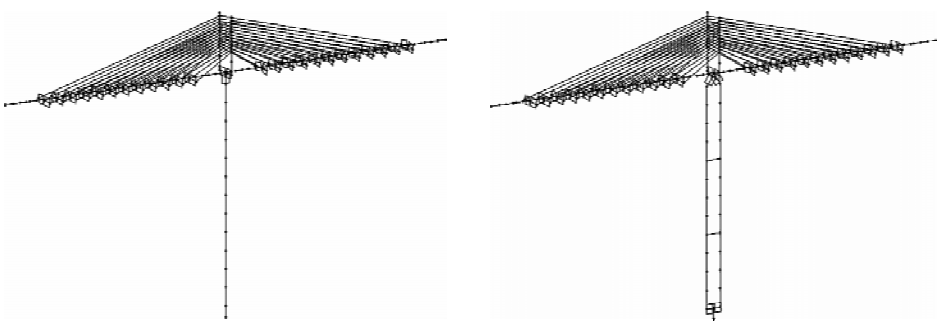

(a) Hollow pier structure (b) Double thin-wall structure

Figure 4 Finite element model

ANALYSIS RESULTS

Eigenvalue Analysis

The seismic characteristics of double thin-wall structure and hollow pier structure are illustrated in Table 4.

TABLE 4 THE DYNAMIC CHARACTERISTICS OF CORRUGATED STEEL WEBS EXTRADOSED CABLE-STAYED BRIDGE

Double thin-wall-construction						Hollow pie-construction					
Order	Frequency	Modal participation mass /%			Mode shape	Order	Frequency	Modal participation mass /%			Mode shape
	Hz	x	y	z			Hz	x	y	z	
1	0.15	69.9			L 1-order	1	0.31	58.6			L 1-order
2	0.28		58.5		T 1-order	2	0.32		56.0		T 1-order
3	0.66	7.2				4	0.92	5.5			
8	1.19			26.5	V 1-order	6	1.19			22.5	V 1-order
11	2.35		6.1			9	2.26	6.2			
22	4.56			17.7		10	2.44		8.7		
28	5.92			19.8		15	4.67			12.3	
34	7.37			6.3		21	6.27			23.1	
193	72.20	16.4				26	7.45			11.4	
195	73.33		16.3			164	70.99		14.8		
274	130.62			15.5		165	71.17	14.6			
						239	128.13			12.9	
	$\sum$:	100	100	100			$\sum$:	100	100	100	

In Table 4, L-Longitudinal, T-Transverse, V-Vertical.

From Table 4, we can see that double thin-wall structure and hollow pier structure's first-order mode shape are longitudinal vibration. Fundamental frequencies are respectively 0.15 Hz and 0.49 Hz. Mode participation mass are respectively 58.6% and 69.9%. Transverse first-order vibration frequency are respectively 0.28 Hz and 0.32 Hz. Mode participation mass are respectively 56% and 58.5%. Vertical vibration first-order frequencies are all 1.19 Hz. Mode participation mass are 22.5% and 26.5% respectively. Two types of structure's longitudinal and transverse mode shape contribution rate concentrated on first order and second order respectively, while vertical has no clear focus, in relative isolation.

The Moment of Structure Compared with Seismic Wave and Moving Load

Study the double thin-wall piers structure, main girder moments at mid-span and pier top, pier moment at bottom are showed in Table 5. Compared with seismic and moving load, structure's moment is larger under the earthquake. Especially, the moments under E2 seismic wave are larger than the moments under moving load, respectively 167%, 207%, 304%. When we design the bridge in the earthquake area, design process should be based on the control of internal forces under earthquake, and girder height is necessary to increase.

TABLE 5 CONSTUCTION'S LONGITUDINAL MOMENT UNDER EARTHQUAKE OR MOVING LOAD(kN · m)

Loads	Girder		Pier bottom
	Mid-span	Pier top	
Moving load	3.82E+04	6.36E+04	5.30E+04
E1	4.82E+04	8.96E+04	8.66E+04
E2	1.02E+05	1.95E+05	2.14E+05

Seismic Analysis Compared with Double Thin-wall Structure and Hollow Pier Structure

Under action of earthquake, internal force of main girder and pier are showed in Table 6. Compared with double thin wall structure and hollow pier structure, girder's transverse moment at pier top and pier's longitudinal moment at pier bottom vary greatly. The former increases about 43%, the latter decreases 24%.

TABLE 6 THE LONGITUDINAL MOMENT RATIO DOUBLE THIN-WALL TO HOLLOW PIER CONSTUCTION

Wave	Moment	Girder		Pier bottom
		Mid-span	Pier top	
E1	Mx	1.00	0.94	0.26
	My	1.32	1.43	0.67
E2	Mx	1.00	1.20	0.24
	My	1.12	1.07	0.76

As Table 5 and Table 6 showed, the double thin wall structure's displacement of tower top is different from the hollow pier structure. For the longitudinal displacement at tower top, about 30 seconds ago, the double thin wall structure is litter than the hollow pier structure. But after 30 seconds, the situation is contrary. For the transverse displacement maximum of tower top, the double thin wall structure is 104 mm larger than the hollow pier structure, and the double thin wall structure's convergence rate is slower.

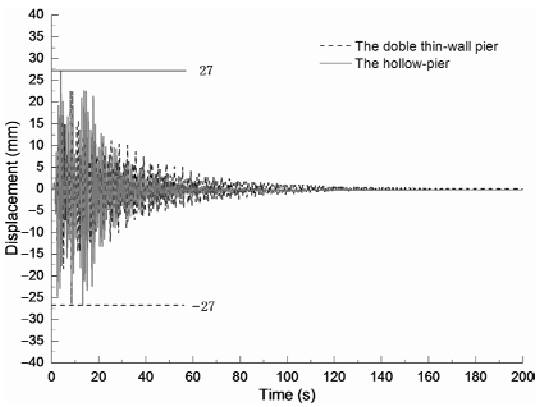

(a) Calculation results under E1

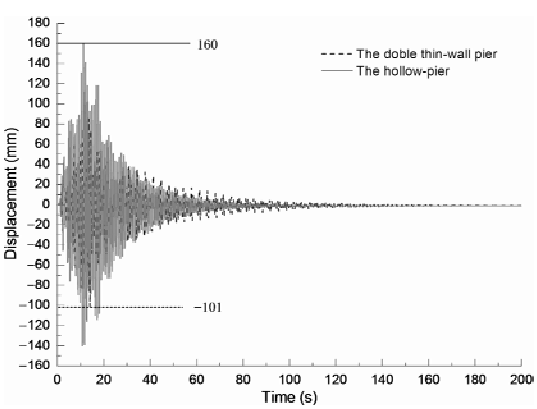

(b) Calculation results under E2

Figure 5 The longitudinal displacement time-history of tower top as different piers

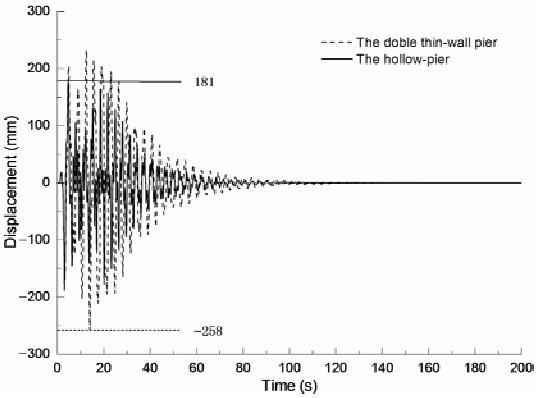

(a) Calculation results under E1

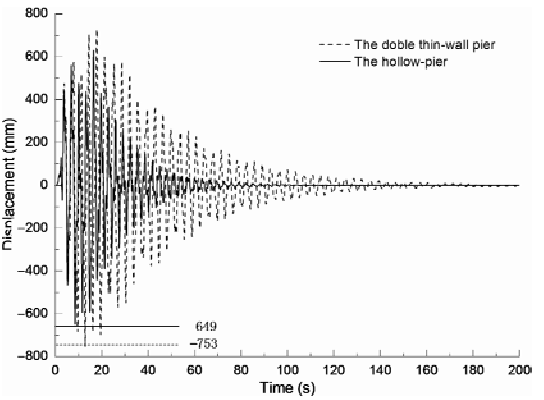

(b) Calculation results under E2

Figure 6 The transverse displacement time-history of tower top as different piers

The Change of Tower Height on Seismic Responses

Figure 7～10 are double thin-wall-structure calculation results. Under the fact of E1 seismic wave, the moment distribution showed in Figure 7(a) and Figure 8(a). As height-span ratio decreased, the moments changed as follows: For longitudinal moment, girder decreased and then increased, the pier bottom decreased. For transverse moment, girder changed a little, pier bottom decreased and then increased. Under the fact of E2 seismic wave, the moment distribution showed in Figure 7(b) and Figure 8(b). As height-span ratio decreased, the moments changed as follows: For longitudinal moment, girder increased and then decreased, the pier bottom changed a little. For transverse moment, girder increased, pier bottom decreased and then increased.

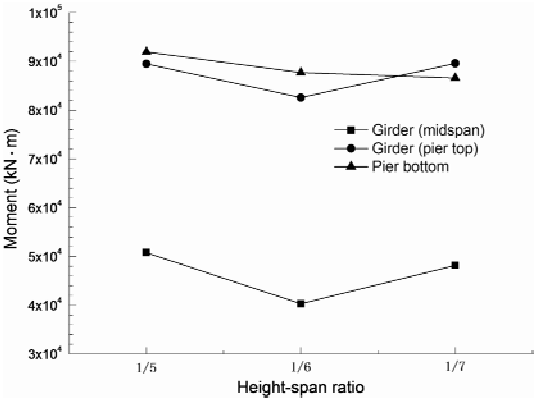

(a) Calculation results under E1

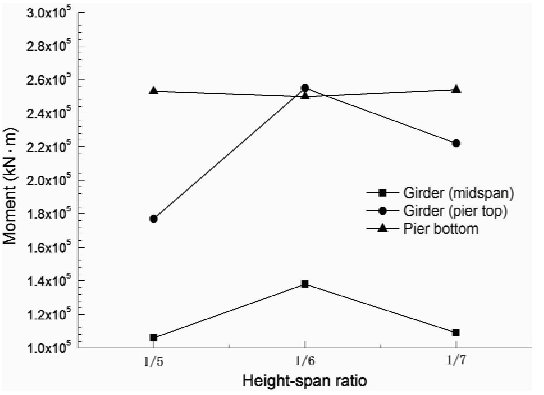

(b) Calculation results under E2

Figure 7 The relationship between longitudinal moments and height-span ratio

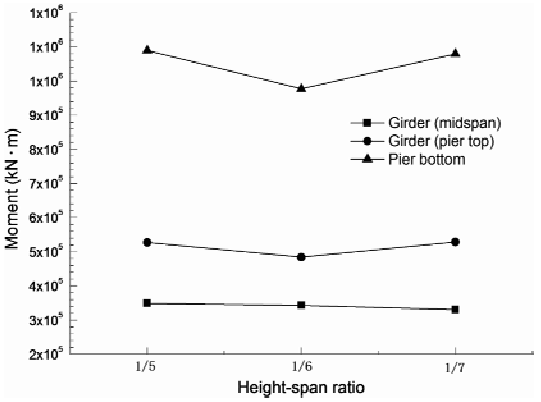

(a) Calculation results under E1

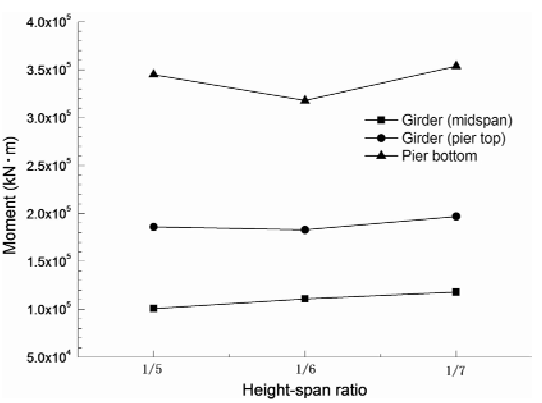

(b) Calculation results under E2

Figure 8 The relationship between transverse moments and height-span ratio

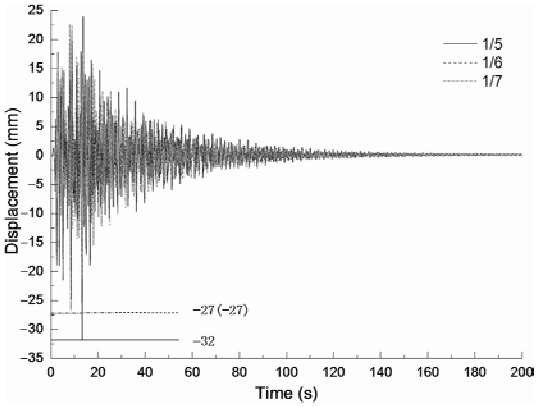

(a) Calculation results under E1

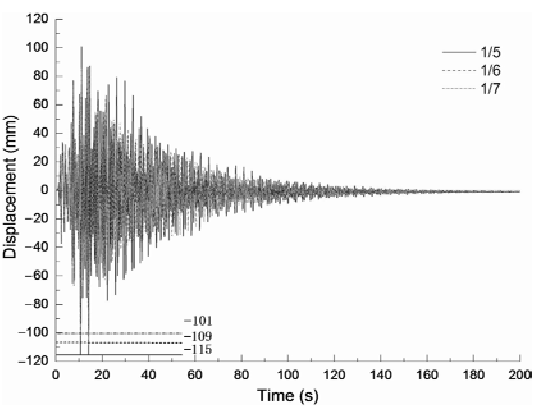

(b) Calculation results under E2

Figure 9 The longitudinal displacement time-history of tower top as different height-span ratios

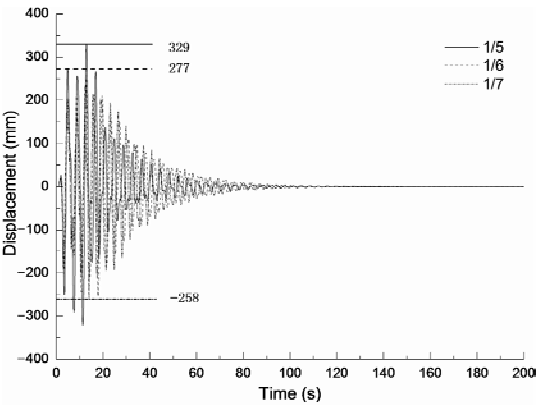

(a) Calculation results under E1

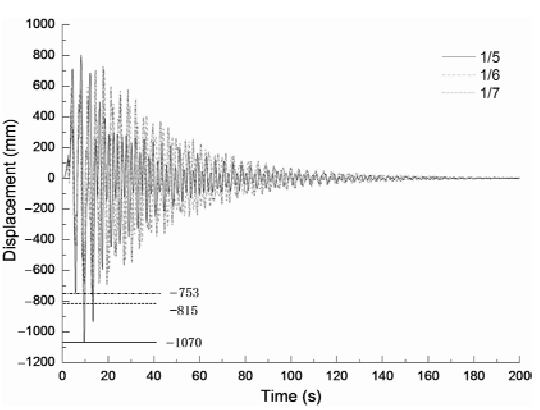

(b) Calculation results under E2

Figure 10 The transverse displacement time-history of tower top as different height-span ratios

Under the fact of E1 seismic wave, the tower top displacements changed as Figure 9(a) and Figure 10(a)

showed. As height-span ratio decreased, longitudinal displacement's maximum and decay rate changed a little. Transverse displacement's maximum turned down, and decay rate changed a little. Under the fact of E2 seismic wave, the tower top displacements changed as Figure 9(b) and Figure 10(b) showed. As height-span ratio decreased, longitudinal displacement's maximum and decay rate changed a little. Transverse displacement's maximum and decay rate turned down obviously.

CONCLUSION

Through the analysis above, the following conclusions are obtained:

Compared with seismic and moving load, structure's moment is larger under the earthquake. When we design the bridge in the earthquake area, design process should be based on the control of internal forces under earthquake, and girder height is necessary to increase.

Compared with double thin wall structure and hollow pier structure, girder's transverse moment at pier top and pier's longitudinal moment at pier bottom vary greatly. The former increases about 43%, the latter decreases 24%.

The double thin wall structure's displacement of tower top is different from the hollow pier structure's, For the longitudinal displacement of tower top, about 30 seconds ago, the double thin wall structure is litter than the hollow pier structure. But after 30 seconds, the situation is contrary. For the transverse displacement maximum of tower top, the double thin wall structure is 104 mm larger than the hollow pier structure, and the double thin wall structure's decay rate is slower.

Under earthquake, the moment distribution is complex as height-span ratio decreased. It depends on the characteristics of structure and seismic wave. The longitudinal displacement maximum and displacement convergence rate at tower top change little. The transverse displacement maximum decreased, and displacement convergence rate turns down obviously.

REFERENCE

[1] Chen, B.C., Chen, X.Y. and Lin, S., "Investigation and Analysis on the application of corrugated steel web Bridge", Journal of China & foreign highway, 2010(1), pp.109-118.

[2] Jiang, X.Q., "The dynamic characteristics analysis of corrugated sheet web plate PC combined box girder", Shanxi architecture. 2009(25), pp.323-324.

[3] Chen, C.C., Zhou, H.Z. and Xiao, R.C., "Recent research advancement of extradosed cable-stayed bridge", Word bridge, 2006(1), pp.70-73.

[4] Chen, B.C., Huang, L. and Wu, Y.X.g, "Extradosed-bridge with corrugated steel webs", Word bridge, 2004 (4), pp.5-8.

[5] Zhang, C.Q., An, Y.R. and An, L.P., "Corrugated steel web continuous rigid frame bridge seismic response analysis", Bridge construction, 2011(3), pp.17-21.

[6] Wang, C., Chen, H.L. and Wan, S., "Analysis on the anti-seismic performance of the Pre-stressed Composite box-girder viaduct with corrugated steel webs", Shanxi architecture. 2009(29), pp.291-292.

[7] Zhu, C.W. and Zhu, Y. F., "Corrugated steel web box girder bridge mechanics characteristics analysis", Science & technology information, 2009(19). pp.75-77.

[8] China communication press, "Guidelines for seismic design of highway bridges", JTG/T B02-01-2008.

PARAMETER SENSITIVITY ANALYSIS OF FLUTTER STABILITY AND ITS APPLICATION ON TAIZHOU BRIDGE

* H. Wang, J. Niu and Z. Zong

School of Civil Engineering, Southeast University, SiPaiLou 2, Nanjing, 210096, China
* Email: woneng2008@163.com

KEYWORDS

Suspension bridges, parameter sensitivity, triple-tower, flutter, finite element, aerodynamic stability.

ABSTRACT

As the most hazardous wind-induced vibration for the long-span suspension bridge, flutter turns into one of the key issues in bridge wind engineering research for a long time. Located in Jiangsu Province, Taizhou Yangtze River Bridge (Taizhou Bridge) is the first-built triple-tower long-span suspension bridge in China. Taizhou Bridge is taken as an example in this study. Firstly, the three-dimensional finite element (FE) model is established according to the design drawings based on ANSYS program. After the theory of ANSYS-based flutter stability analysis is demonstrated, the flutter analysis of the bridge is then conducted and the parametric sensitivity on the flutter stability of the bridge is investigated. The analyzed parameters and structural components include the sag-to-span ratio, the stiffness of the main girder, the dead load of the main girder, the rigid central buckle, the longitudinal stiffness of the middle tower and the cable system. Results show that the sag-to-span ratio of cables, the torsional stiffness of the main girder, the central buckle and the cable system has significant influence on the flutter stability of the bridge, and the influence of the cable system is prominent. The effects of the stiffness of the main girder, the dead load of the deck and the longitudinal stiffness of the middle tower are limited. This study can provide reference for flutter stability analysis and design of triple-tower long-span suspension bridges.

INTRODUCTION

Flutter is the most hazardous vibration for the long-span suspension bridge as the bridge oscillated in a divergent and destructive manner at some critical wind velocity (Simiu and Scanlan 1996). With the increases in bridge span, flutter instability potentially occurs for fairly low wind velocity because of the large flexibility and low structural damping. (Scanlan and Tomko 1971). During the design and construction procedure of long-span bridges, the lowest wind velocity inducing flutter instability of a bridge must be larger than the maximum design wind velocity of the bridge. There are many methods at present for flutter stability analysis of bridges, such as the full-order flutter analysis method (Dung et al. 1998; Ding et al. 2002), the multimode flutter analysis technique (Namini et al. 1992; Tanaka et al.

1992; Katsuchi et al. 1999; Chen 2007; Hua et al. 2007), etc. In this paper, full-order flutter analysis method was used to obtain the flutter velocity. The full-order method is not based on the structural modal but the system model of the interaction between the structures and aerodynamic forces, meanwhile, the overall influences of structural modal without modal analysis in advance is considered.

However, most researches on aerodynamic stability analyses are focused on two-tower suspension bridges (Abdel-Ghaffar, 2000; Zhang and Sun 2004; Almutairi et al., 2006; Wang et al., 2011). The triple-tower suspension bridge is totally a brand new type of structural form. Compared to a two-tower suspension bridge, structural characteristics of a triple-tower suspension bridge are strikingly different owing to the addition of a middle tower and an additional main span. Yoshida et al. (2004) studied the parameters influencing the deformation characteristics of a four-span suspension bridge which had two main spans 2 000 m in each length. In general, the analysis of triple-tower bridges is insufficient, especially the study on aerodynamic stability characteristics. In this paper, Taizhou Bridge, the first triple-tower long-span suspension bridge in China, is taken as an example for the study. The three-dimensional flutter stability analysis of the bridge is conducted based on ANSYS program using the full-order flutter analysis method, and the design parameter sensitivity analyses on the structural flutter stability are carried out.

FINITE ELEMENT (FE) MODEL OF THE BRIDGE FOR FLUTTER ANALYSIS

Bridge Description

Taizhou Bridge is a triple-tower long-span suspension bridge crossing the Yangtze River. The bridge connects Taizhou City with Changzhou City in Jiangsu Province, China. The typical streamline flat steel box girders were used as the main girder of the bridge. The material and sectional characteristic parameters of Taizhou Bridge are shown in Table 1.

TABLE 1 METERIAL AND SECTIONAL CHARACTERISTIC PARAMETERS OF TAIZHOU BRIDGE

Structural members	A /m^2	J_d/m^4	J_y/m^4	J_z/m^4	E/P$_a$	ρ/(kg/m^3)
Main girder	1.497	8.439	191.710	2.928	2.1×10^{11}	13 152.72
Main cable	0.286	—	—	—	2.0×10^{11}	7 850
Suspender	0.002 63	—	—	—	2.0×10^{11}	7 850
Middle tower	1.541～3.955	7.116～30.603	7.110～96.079	5.570～14.603	2.1×10^{11}	7 850

Notes: A—sectional area; J_d—torsional moment inertia; J_y—lateral bending moment inertia; J_z—vertical bending moment inertial; E—elastic modulus; ρ—density

Initial FE Model of Taizhou Bridge

A backbone model is generally used to simulate the main girder of the long-span suspension bridge as the researcher conducting dynamic analysis. Figure 1 shows the initial FE analysis model of Taizhou Bridge for performing the static, modal and seismic response analysis. The model was established based on ANSYS program, and the backbone was employed to simulate the steel box girder.

The model represented the bridge with the geometry and structural properties estimated according to the engineering design drawings. The steel girders and three towers were modeled by spatial beam elements

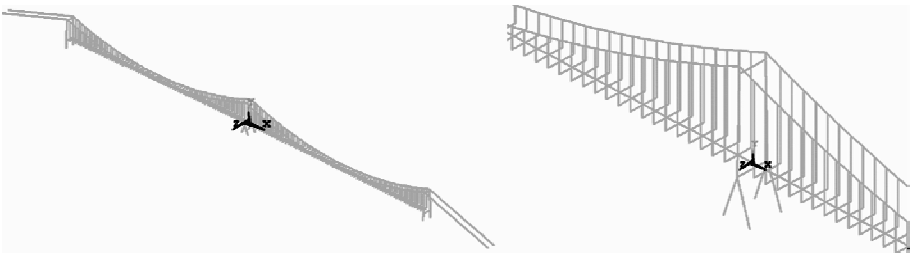

Figure 1 Initial FE model of Taizhou Bridge

with six degrees of freedom (DOF) at each node. The stiffness and the mass of the steel box girder were lumped on the middle nodes. As for the steel box girder, the element stiffness was taken as its actual stiffness, while the element density was taken as the transformed density of the dead loads including the first and second phases of the bridge deck. The cross beams connecting the suspender and the steel box girder, as well as the central buckle, were also modeled by spatial beam elements. The difference between cross beams and the central buckle is that the elastic modulus of these beam elements was set so high that they are actually considered as rigid arms. The main cable and the suspender were simulated by 3-D linear elastic truss elements with three DOFs at each node, and the main cable was also meshed to match the nodes of the suspender. The truss elements were assigned the property of tension-only with no compression based on the real condition observed. The nonlinearity of the back cable stiffness due to gravity was approximated by the linearized stiffness using the Ernst equation of equivalent modulus of elasticity (Ernst 1965). Refer to the design analysis of the bridge, the deck and two side towers were coupled in 3-DOFs, including the vertical displacement, the transverse displacement and the rotation around longitudinal direction. As for the middle tower, only the lateral DOF was coupled with the steel box girder. The spring element was used to simulate longitudinal elastic restraints between the lower cross beam of the middle tower and the steel box girder, and the stiffness of which is set as the value 640 KN/mm. The main cables were fixed on top of the towers. The bottom of both back cables and towers were fixed at the base, ignoring the soil-pile-structure interaction.

Simulation f Self-excited Forces of Bridge Deck

In order to conduct buffeting and flutter analyses using general-propose FE software, some efforts (Hua et al., 2007; Wang et al., 2011) have been made by employing a user-defined element with aeroelastic stiffness and damping matrices to model self-excited forces in ANSYS. The self-excited forces acting on unit span of bridge deck can be expressed as a linear function of nodal displacement and nodal velocity (Sarkar et al., 1994; Jain et al., 1996). The hybrid FE model for flutter analysis is achieved by attaching *Matrix27* elements to the initial FE model of the bridge. After *Matrix27* elements are incorporated into the initial FE model of the bridge, the FE model used for flutter analysis are achieved.

MODEL ANALYSIS OF THE BRIDGE

Modal analysis of Taizhou Bridge was conducted by using the SUBSPACE method based on ANSYS program, and dynamic characteristics of the bridge are obtained. Table 2 indicates that the first natural frequency of the bridge is 0.071 63 Hz corresponding to the first antisymmetric lateral bending mode of the main cable and the steel box girder. The longitudinal floating vibration mode of the bridge is not obvious due to the elastic restraint employed between the steel box girder and the middle tower.

TABLE 2 FRIST 25 VIBRATION MODES AND FREQUENCIES OF BRIDGE

Order No.	Frequency (Hz)	Vibration mode description	Order No.	Frequency (Hz)	Vibration mode description
1	0.071 63	AS L vibration of steel box girder	14	0.273 72	S vibration of main cables
2	0.080 23	AS V vibration of steel box girder	15	0.273 77	S vibration of main cables
3	0.095 12	S L vibration of steel box girder	16	0.289 52	S vibration of main cables
4	0.114 89	AS V vibration of steel box girder	17	0.289 54	S vibration of main cables
5	0.117 58	S V vibration of steel box girder	18	0.290 15	AS L vibration of main cables
6	0.137 09	S V vibration of steel box girder	19	0.290 64	L vibration of middle tower and main cables
7	0.170 89	AS V vibration of steel box girder			
8	0.185 18	S V vibration of steel box girder	20	0.302 62	AS L vibration of main cables
9	0.230 58	AS L vibration of steel box girder	21	0.314 61	AS V vibration of towers
10	0.237 86	AS V vibration of steel box girder	22	0.315 26	S V vibration of steel box girder
11	0.239 83	S V vibration of steel box girder	23	0.318 31	AS V vibration of steel box girder
12	0.245 14	L vibration of middle tower	24	0.320 88	S L vibration of main cables
13	0.272 90	AS T vibration of steel box girder	25	0.366 13	S T vibration of steel box girder

Notes: S—symmetric; AS—antisymmetric; L—lateral; V—vertical; T—torsional.

PARAMETER SENSITIVITY STUDY ON FLUTTER STABILITY OF THE BRIDGE

Based on the three-dimensional FE model for buffet analysis, the flutter stability analysis is performed in ANSYS. The structural damping ratio is assumed as 0.5%. The aerodynamic coefficients and flutter derivatives at different wind attack angles are obtained from the section-model tests (Chen, 2006). Table 3 shows that the flutter stability is worst when the wind attack angle is positive, therefore, only at the wind attack angles of 0° and +3° are considered in the following analysis.

TABLE 3 FLUTTER WIND SPEED OF TAIZHOU BRIDGE AT DIFFERENT ATTACK ANGLES

Wind attack angle (°)	+3	0	−3
Calculation flutter wind speed (m/s)	60.01	80.27	73.94
Measured flutter wind speed (m/s)	61.9	82.8	74.2

Sag-to-span Ratio

The sag-to-span ratio is an important design parameter for long-span suspension bridges since it can influence tension forces of main cables and the system stiffness of the bridge. Generally, the sag-to-span ratio of cables ranges from 1/8 to 1/12 (Zhang and Sun, 2004). The relations between the frequency of the mode participating in flutter and the sag-to-span ratio are shown in Table 4, and the relations between the flutter wind speed and the sag-to-span ratio are plotted in Figure 2. During the analysis, the line shape and the initial strain of the main cable, the height of the main tower and the length of the suspender vary according to the sag-to-span ratios. Other design parameters are kept unchanged. As shown in Table 4 and Figure 2, the sag-to-span ratio when it is smaller than 0.1 has great influence on the vibration frequency and the flutter wind speed of Taizhou Bridge. As the sag-to-span ratio increases, the 1-S-V frequencies decrease accordingly. As for the 1-AS-T frequencies, it becomes larger at first and turns down after the sag-to-span ratio reaches 1/9. The change results from the joint action of these two

frequency in the maximum flutter wind speed appears when the sag-to-span ratio is slightly greater than 0.09. In general, decreasing the sag-to-span ratio will improve the vertical stiffness and the static performance. Accordingly, the structural frequencies will be improved. However, the structural stiffness increasing is not favorable for aerodynamical behavior of the bridge. Therefore, the sag-to-span ratio should be determined by both the structural static performance and the dynamical behavior during the design procedure for a long span suspension bridge.

TABLE 4 INFLUENCE OF SAG-TO-SPAN RATIO

Sag-to-span ratio	1-S-V Frequency (Hz)	1-AS-V Frequency (Hz)	1-AS-T Frequency (Hz)
1/12	0.129 46	0.082 01	0.260 61
1/11	0.125 50	0.082 04	0.264 53
1/10	0.121 77	0.082 16	0.269 44
1/9	0.117 58	0.080 23	0.272 90
1/8	0.113 93	0.074 31	0.266 09

Notes: 1—first; S—symmetric; AS—antisymmetric; V—vertical; T—torsional.

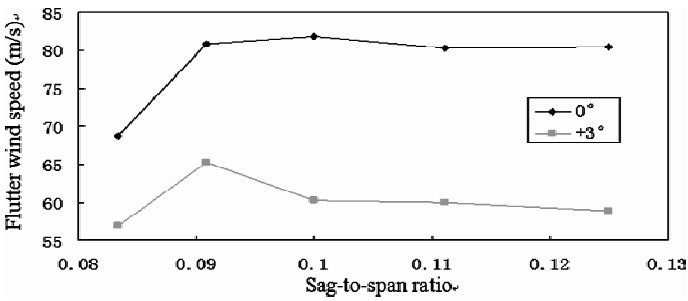

Figure 2 Influence of sag-to-span ratio on the flutter wind speed

Vertical Stiffness Of the Main Girder

The effects of stiffness of the main girder on the frequencies of modes participating in flutter and the flutter wind speed of the bridge were also studied in this paper. When the vertical stiffness multiple of the main girder changes from 0.8 to 1.8, the frequencies of dominated modes in flutter are shown in Table 5. Table 5 shows that the increase in vertical stiffness has little influence on the dominated frequency, while the 1-S-V and 1-AS-V frequencies increase a little. When the vertical stiffness multiple changes from 0.8 to 1.8, the 1-AS-V frequency increases from 0.080 02 Hz to 0.080 89 Hz, and the 1-S-V frequency increases from 0.117 13 Hz to 0.118 76 Hz, which is only 1.14% and 1.39%, respectively. The reason is that the gravity stiffness forms a large part of the vertical stiffness of the full bridge, reducing the influence of vertical stiffness of the main girder on the vibration frequencies of the bridge. As a result, the influence of vertical stiffness of the main girder on flutter wind speeds of the bridge is very small.

TABLE 5 INFLUENCE OF VERTICAL STIFFNESS OF THE MAIN GIRDER

V stiffness multiple	1-S-V Frequency (Hz)	1-AS-V Frequency (Hz)	1-AS-T Frequency (Hz)
0.8	0.117 13	0.080 01	0.272 85
1.0	0.117 58	0.080 23	0.272 90

continued

V stiffness multiple	1-S-V Frequency (Hz)	1-AS-V Frequency (Hz)	1-AS-T Frequency (Hz)
1.2	0.117 97	0.080 39	0.272 93
1.4	0.118 34	0.080 55	0.272 94
1.6	0.118 61	0.080 74	0.272 90
1.8	0.118 76	0.080 92	0.272 89

Torsional Stiffness of the Main Girder

The frequencies of dominated modes in flutter are also analyzed when the torsional stiffness multiple of the main girder changes from 0.8 to 1.8. The result shows that the 1-S-V and 1-AS-V frequencies keep almost unchanged as the torsional stiffness changes, while the 1-AS-T frequency increase accordingly. Table 6 shows the effects of torsional stiffness of the main girder on the 1-AS-T frequency of the bridge. The relations between the flutter wind speed and the torsional stiffness are plotted in Figure 3. Table 6 and Figure 3 show that the increase in torsional stiffness has significant effects on both the flutter wind speed and the 1-AS-T frequency. When torsional stiffness multiple of the main girder changes from 0.8 to 1.8, the 1-AS-T frequency changes from 0.262 81 to 0.293 64 Hz with increasing rate of 11.7%, which is a great contribution to the improvement of the flutter stability performance for the bridge.

TABLE 6 INFLUENCE OF TORSIONAL STIFFNESS OF THE MAIN GIRDER

V stiffness multiple	0.8	1.0	1.2	1.4	1.6	1.8
1-AS-T Frequency (Hz)	0.262 81	0.272 90	0.280 95	0.287 03	0.291 19	0.293 64

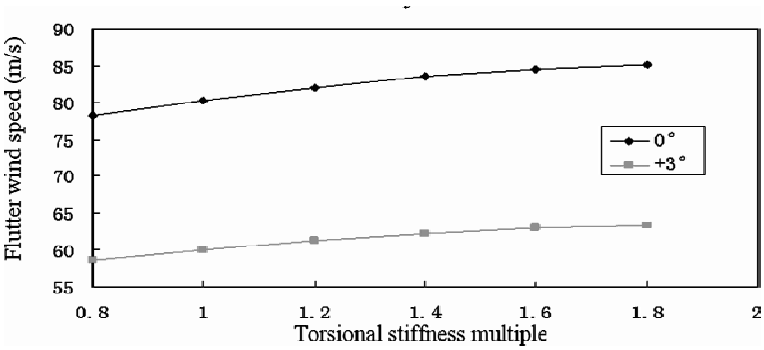

Figure 3 Influence of torsional stiffness on the flutter wind speed

Dead Load of the Main Girder

In order to investigate the influence of the dead load of the main girder on the flutter stability of the bridge, flutter analyses with different dead loads of the main girder are conducted. The relation between the frequencies of modes participating in flutter and the dead load of the main girder are shown in Table 7, and Figure 4 shows the influence of the dead loads of the deck on the flutter wind speed of bridge. During the analysis, the tension forces of the main cables and the suspenders change accordingly. Other parameters are kept unchanged. As shown in Figure 4, the influence of dead load of the main girder on

the flutter wind speed is very little when the attack angle is +3°. The reason is that adding the dead load will increase both the gravity stiffness and the mass of the bridge, making the dominated 1-S-V frequency almost constant and the 1-AS-T frequency decreases, as shown in Table 7. In addition, increasing the dead load of the main girder will lead to an uneconomical design. Therefore, increasing the dead load is not an effective measure to increase the flutter wind speed when all factors are considered.

TABLE 7 INFLUENCE OF DEAD LOAD OF THE MAIN GIRDER

Dead load multiple	0.8	1.0	1.2	1.4	1.6	1.8
1-S-V Frequency (Hz)	0.117 91	0.117 58	0.117 29	0.117 05	0.116 84	0.116 67
1-AS-V Frequency (Hz)	0.084 67	0.080 23	0.076 79	0.074 21	0.072 00	0.070 28
1-AS-T Frequency (Hz)	0.288 48	0.272 90	0.259 92	0.248 88	0.239 04	0.230 59

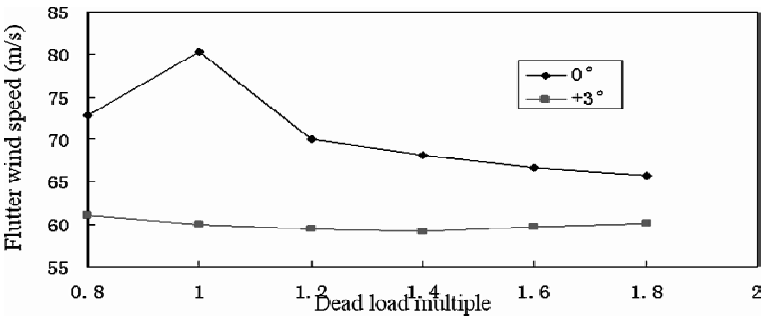

Figure 4 Influence of dead load on the flutter wind speed

Rigid Central Buckle

To investigate the influence of the rigid central buckle on the flutter stability performance of the bridge, the rigid central buckle is employed to replace the short suspenders at the midspan and other parameters are kept unchanged. The first 25 natural frequencies and vibration mode characteristics with the rigid central buckle are shown in Table 8.

TABLE 8 FRIST 25 VIBRATION MODES AND FREQUENCIES OF BRIDGE WITH RIGID CENTRAL BUCKLE

Order No.	Frequency (Hz)	Vibration mode description	Order No.	Frequency (Hz)	Vibration mode description
1	0.071 85	AS L vibration of steel box girder	15	0.291 30	S vibration of main cables
2	0.083 55	AS V vibration of steel box girder	16	0.291 30	S vibration of main cables
3	0.095 54	S L vibration of steel box girder	17	0.292 25	AS T vibration of steel box girder
4	0.130 04	S V vibration of steel box girder	18	0.296 84	L vibration of middle tower and main cables
5	0.133 44	AS V vibration of steel box			
6	0.169 19	S V vibration of steel box girder	19	0.301 20	AS L vibration of main cables
7	0.171 81	AS V vibration of steel box girder	20	0.305 94	AS L vibration of main cables
8	0.233 42	AS L vibration of steel box girder	21	0.317 72	AS V vibration of steel box girder
9	0.236 07	S V vibration of steel box girder	22	0.318 81	S V vibration of steel box girder
10	0.238 69	AS V vibration of steel box girder	23	0.325 33	L vibration of middle tower
11	0.241 37	S V vibration of steel box girder	24	0.340 92	Longitudinal vibration of middle tower
12	0.248 83	L vibration of middle tower			

continued

Order No.	Frequency (Hz)	Vibration mode description	Order No.	Frequency (Hz)	Vibration mode description
13	0.286 64	S vibration of main cables	25	0.370 63	S T vibration of steel box girder
14	0.286 72	S vibration of main cables			

TABLE 9 INFLUENCE OF RIGID CENTRAL BUCKLE ON THE FLUTTER WIND SPEED OF THE BRIDGE

Connection	Wind attack angle (+3°)	Wind attack angle (0°)
Short suspender	60.01 m/s	80.27 m/s
Rigid central buckle	65.87 m/s	86.93 m/s

As can be seen in Table 8, owing to employing the rigid central buckle, the 1-S-V frequency increase from 0.117 58 to 0.130 04 Hz, the 1-AS-T frequency changes from 0.272 90 to 0.292 25 Hz, and the 1-S-T frequency changes from 0.366 13 to 0.370 63 Hz , with the increasing rate of 10.6% , 7.1% and 1.2 %, respectively. As a result, the flutter wind speed of the bridge increases obviously, as shown in Table 9. Under the wind attack angle of +3° and 0°, the increase rate are 10.6% and 8.3%, respectively. Obviously, installing the rigid central buckle is an effective measure to improve the aerodynamic stability of the triple-tower long-span suspension bridge.

Longitudinal Stiffness of the Middle Tower

The influence of the longitudinal stiffness of the middle tower on the dynamic characteristics and the flutter stability performance of Taizhou Bridge are investigated. When the longitudinal stiffness multiple of the main tower changes from 0.8 to 1.8, the frequencies of dominated modes in flutter are shown in Table 10, and the corresponding flutter wind speed are plotted in Figure 5. During the analysis, only the longitudinal stiffness of the middle tower changes and other design parameters are kept the same. Table 10 shows that the influence of longitudinal stiffness of the middle tower on the 1-S-V and 1-AS-T frequency is not obvious. The changes of the flutter wind speed are very small when the longitudinal stiffness multiple of the main tower changes from 0.8 to 1.8, as shown in Figure 5. Therefore, increasing the longitudinal stiffness of the main tower alone is not an effective means to improve the flutter stability performance of the triple-tower long-span suspension bridge.

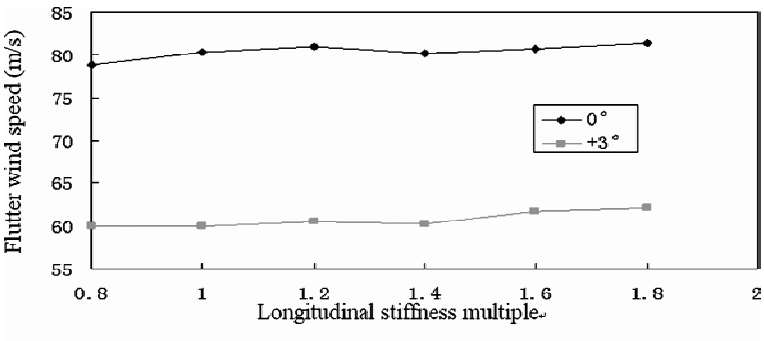

Figure 5 Influence of longitudinal stiffness of the middle tower on the flutter wind speed

TABLE 10 INFLUENCE OF LONGITUDINAL STIFFNESS OF THE MIDDLE TOWER

Longitudinal stiffness multiple	0.8	1.0	1.2	1.4	1.6	1.8
1-S-V Frequency (Hz)	0.117 53	0.117 58	0.117 66	0.117 72	0.117 60	0.117 70
1-AS-V Frequency (Hz)	0.077 69	0.080 23	0.085 50	0.084 37	0.087 12	0.086 84
1-AS-T Frequency (Hz)	0.272 11	0.272 90	0.273 54	0.274 85	0.275 46	0.276 05

Cable System

When the parallel cable system is changed into the spatial cable system, the frequencies of dominated modes in flutter and the corresponding flutter wind speed are shown in Tables 11 and 12, respectively. During the analysis, only the cable system is changed and other design parameters are kept the same. As shown in Table 11, the 1-AS-T Frequency increases remarkably when the spatial cable system is adopted. As a result, the flutter stability performance is improved greatly. Table 12 shows that the increasing rates of the flutter wind speed are 22.3% and 17.8% at the wind attack angle of $+3^{\circ}$ and 0°, respectively. Therefore, by using the spatial cable system is a very effective measure to improve the flutter stability performance of the triple-tower long-span suspension bridge.

TABLE 11 INFLUENCE OF CABLE SYSTEM

Cable system	1-S-V Frequency (Hz)	1-AS-V Frequency (Hz)	1-AS-T Frequency (Hz)
Parallel	0.117 58	0.080 23	0.272 90
Spatial	0.117 20	0.080 04	0.350 76

TABLE 12 INFLUENCE OF CABLE SYSTEM ON THE FLUTTER WIND SPEED

Cable system	Wind attack angle ($+3^{\circ}$)	Wind attack angle (0°)
Parallel	60.01 m/s	80.27 m/s
Spatial	73.37 m/s	94.58 m/s

SUMMARIES AND CONCLUSIONS

In this study, the full-order methods of flutter analysis based on ANSYS program are employed to perform the flutter analysis on the Taizhou Bridge. The influences of key parameters on the flutter stability of the bridge are investigated. And the following conclusions are made. (1) The sag-to-span ratio of cables has a great influence on the flutter stability of the triple-tower long-span suspension bridge. The maximum flutter wind speed appears as the sag-to-span ratio is slightly greater than 0.09. (2) The torsional stiffness has significant effects on the flutter stability of the triple-tower long-span suspension bridge, while the influence of vertical stiffness of the main girder on flutter wind speeds of the bridge is not obvious. (3) Increasing the dead load of the main girder is not an effective way to improve the flutter stability performance of the triple-tower long-span suspension bridge when the engineering cost-effectiveness is considered. (4) It is an effective measure to increase the flutter wind speed of the triple-tower long-span suspension bridge by installing the rigid central buckle to connect the main cable and the main girder. (5) Increasing the longitudinal stiffness of the main tower alone is not an effective means to improve the flutter stability performance of the triple-tower long-span suspension bridge, while selecting the proper shape of structure for the middle tower is a very effective way to enhance the flutter stability.

(6) The flutter stability performance of the triple-tower long-span suspension bridge can be greatly affected by the cable system, among which the spatial cable system is a very favorable way to increase the flutter wind speed of the bridge.

ACKNOWLEDGEMENTS

This work is supported by the National Science Foundation of China (Grant No. 50725828, 50908046, 50978056), the Teaching & Scientific Research Fund for Excellent Young Teachers of Southeast University, and the Basic Scientific & Research Fund of Southeast University (Grant No. Seucx201106) are gratefully acknowledged.

REFERENCES

[1] Abdel-Ghaffar, A.M. (2000), "Vibration studies and tests of a suspension bridge", Computers & Structures, 76 (6), pp.787-97.
[2] Almutairi, N.B., Hassan, M.F., Abdel-Rohman, M. and Terro, M. (2006), "Control of suspension bridge nonlinear vibrations due to moving loads", J Engrg Mech ASCE, 132(6): pp.659-670.
[3] Chen, A.R. (2006), "Wind-resistant Research on the Taizhou Yangtze River Highway Bridge", Research Report of Tongji University, Shanghai, China. (in Chinese)
[4] Chen, X. (2007), "Improved understanding of bimodal coupled bridge flutter based on closed-form solution", Journal of Structural Engineering, ASCE, 133, pp.22-31.
[5] Ding, Q., Chen, A. and Xiang, H. (2002), "Coupled flutter analysis of long-span bridges by multimode and full-order approaches", Journal of Wind Engineering and Industrial Aerodynamics, 90, 1981-1993.
[6] Dung, N. N., Miyata, T., Yamada, H. and Minh, N. N. (1998), "Flutter responses in long span bridges with wind induced displacement by the mode tracing method", Journal of Wind Engineering and Industrial Aerodynamics, 77-78, pp.367-379.
[7] Ernst, H. J. (1965), "Der E-Modul von Seilen unter Berücksichtigung des Durchhanges", Der Bauingenieu, 40 (2), pp.52-55 (in German).
[8] Hua, X. G., Chen, Z. Q., Ni, Y. Q. and Ko, J. M. (2007), "Flutter analysis of long-span bridges using ANSYS", Wind and Structures, 10(1), pp.61-82.
[9] Jain, A., Jones, N. P. and Scanlan, R. H. (1996), "Coupled flutter and buffeting analysis of long-span bridges", Journal of Structural Engineering, ASCE, 122, pp.716-725.
[10] Katsuchi, H., Jones, N. P. and Scanlan, R. H. (1999), "Multimode coupled flutter and buffeting analysis of the Akashi-Kaikyo Bridge", Journal of Structural Engineering, ASCE, 125, pp.60-70.
[11] Namini, A., Albrecht, P. and Bosch, H. (1992), "Finite element-based flutter analysis of cable-suspended bridges", Journal of Structural Engineering, ASCE, 118, pp.1509-1526.
[12] Sarkar, P. P., Jones, N. P. and Scanlan, R. H. (1994). "Identification of aeroelastic parameters of flexible bridges", Journal of Engineering Mechanics, ASCE, 120(8), pp.1718-1742.
[13] Scanlan, R. H. and Tomko, J. J. (1971), "Airfoil and bridge deck flutter derivatives", Journal of the Engineering Mechanics Division, ASCE, 91, pp.1117-1137.
[14] Simiu, E. and Scanlan, R. H. (1996), Wind Effects on Structures: Fundamentals and Applications to Design, 3rd edition, John Wiley, New York.
[15] Tanaka, H., Yamamura, N. and Tatsumi, M. (1992), "Coupled mode flutter analysis using flutter derivatives", Journal of Wind Engineering and Industrial Aerodynamics, 42, pp.1279-1290.
[16] Wang, H., Li, A. Q. and Hu, R. (2011), "Comparison of Ambient Vibration Response of the Runyang Suspension Bridge under Skew Winds with Time-Domain Numerical Predictions", Journal of Bridge Engineering, doi:10.1061/(ASCE)BE. 1943-5592.0000168. Published online.
[17] Yoshida, O., Okuda, M. and Moriya, T. (2004), "Structural characteristics and applicability of four-span suspension bridge", J Bridge Engrg ASCE, 9(5), pp.453-463.
[18] Zhang, X. J. and Sun, B. N. (2004), "Parametric study on the aerodynamic stability of a long-span suspension bridge", Journal of Wind Engineering and Industrial Aerodynamics, 92, pp.431-439.

GBT-BASED ELASTIC-PLASTIC ANALYSIS OF COLD-FORMED STEEL MEMBERS

* M. Abambres, D. Camotim and N. Silvestre

Department of Civil Engineering and Arquitecture, ICIST, Instituto Superior Técnico
Technical University of Lisbon, Av. Rovisco Pais, 1049-001 Lisbon, Portugal
* Email: abambres@netcabo.pt

KEYWORDS

Generalised beam theory (GBT), thin-walled members, cold-formed steel, J_2-flow plasticity, local deformation, global deformation.

ABSTRACT

This paper presents a formulation of Generalised Beam Theory (GBT) intended to perform thorough first-order elastic-plastic analyses of thin-walled members subjected to arbitrary deformations and made of an isotropic non-linear material. The J_2-flow theory is used to model plasticity in conjunction with the Euler-Backward return-mapping algorithm. After presenting the formulation, its application is illustrated by means of the first order analysis of a simply supported Z-section beam made of an elastic-perfectly plastic material (e.g., carbon steel) and acted by a load uniformly distributed along the flanges. The set of GBT-based results comprises the load-deflection curves (equilibrium paths), displacement profiles, stress distributions (diagrams and 3D contours), and deformed shapes (modal amplitude functions and 3D configureurations). These results are compared with the ones obtained from shell finite element analyses (SFEA) using ABAQUS. It is seen that the GBT results display a very good agreement with the SFEA values.

INTRODUCTION

The use of high performance materials, such as high-strength and high-ductility metals, has led to an economy in the weight of built structures. In fact, steel structures are progressively more slender and instability phenomena play an important role in their design. Steel members often display thin walls and slender cross-sections, exhibiting high susceptibility to global (flexural and torsional) and local buckling. An accurate prediction of the buckling and collapse behaviour of steel members has been possible by means of the performance of experimental tests. However, they are expensive and their set-up requires a careful preparation of all devices. A much cheaper alternative is the performance of SFEA, using non-linear constitutive laws and incremental-iterative techniques. However, the SFEA output data is generally difficult to interpret because (i) it is based on stresses and strains, not stress resultants, and (ii) it provides member deformed configureurations with mixed global-local modes. Since the use of complex

non-linear SFEA, as well as the interpretation of the results obtained, are time-consuming tasks, a very promising alternative to this approach is the use of Generalised Beam Theory (GBT). Currently, GBT is widely recognized by the scientific community as a powerful, versatile, elegant and efficient thin-walled beam theory. Its elegance arises from the modal nature, i. e., the displacement field is obtained as a linear combination of cross-section deformation modes that vary along the member length. GBT has attracted the interest of several researchers, leading to the development of new formulations and applications. The theory has been extensively upgraded at the Technical University of Lisbon[1] and has been applied to (i) different analysis (first order, buckling, vibration, post-buckling) and (ii) distinct materials (steel, steel-concrete, FRP). In these works, the material was always assumed elastic, with no degradation (plasticity) involved. The first physically non-linear GBT formulation was presented by Gonçalves and Camotim[2], in the context of elastic-plastic bifurcation analysis. Recently, Gonçalves and Camotim[3, 4] proposed a finite element based on the J_2-flow plasticity theory in the context of GBT. In parallel, Abambres et al.[5] developed a GBT first order elastic-plastic formulation, based on the J_2-flow plasticity theory, to analyse members undergoing only global (axial, flexural, torsional) deformation. In order to overcome this limitation, the work presented in this paper extends this formulation to account for arbitrary (local and global) deformations. Although J_2-flow plasticity theory was already adopted by Gonçalves and Camotim[3, 4], the GBT formulation presented herein has novel features, mainly because it is based on a different set of deformation modes, obtained through the GBT cross-section analysis developed by Silva et al.[8]. In order to illustrate the application of the proposed formulation, a simply supported cold-formed steel Z-section beam is analysed and the GBT results are thoroughly discussed and compared with those yielded by ABAQUS[6] SFEA.

BRIEF OVERVIEW OF THE GBT FORMULATION

Due to space limitations, only a brief overview of the GBT formulation is presented in this section. Detailed information can be found in Abambres et al.[5, 7]. The GBT analysis of a structural member consists of two main steps: (i) a cross-section analysis and (ii) a member analysis. The cross-section analysis comprises the determination of the deformation modes and corresponding displacement profiles ($u_k(s)$, $v_k(s)$, $w_k(s)$) along the cross-section mid-line (coordinate s – see Figure 1). The member analysis comprises the determination of the mode amplitude functions $\zeta_k(x)$ that characterise the variation of the mode displacement profiles along the member axis x, i.e., the GBT displacement field corresponds to a linear combination of cross-section deformation modes ($u = u_k(s)\zeta_{k,x}(x)$, $v = v_k(s)\zeta_k(x)$, $w = w_k(s)\zeta_k(x)$).

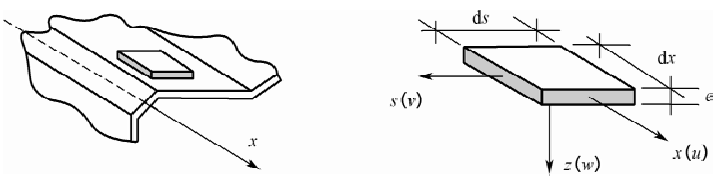

Figure 1 (a) Local coordinate system at each cross-section section wall

As mentioned earlier, the cross-section analysis adopted in this work is based on the approach developed by Silva et al.[8], wherein four deformation mode families (transverse extension, warping shear, local and global) are obtained via the solution of a sequence of eigenvalue problems. All the existing GBT approaches consider four degrees-of-freedom (dof) per node, corresponding to three displacements and one transverse flexural rotation. Besides these four dof, the proposed GBT formulation adopts, for the

first time, an additional dof: a rotation orthogonal to each wall mid-plane, designated as warping rotation. It is considered in each node and wall direction, making it possible to approach the warping profile $u(s)$ by means of piecewise Hermite cubic polynomials, instead of the usual piecewise linear functions[8]. In what follows, the derivation of the GBT incremental equilibrium equations is briefly described.

It is well known that the determination of a non-linear equilibrium configureuration requires the use of an incremental-iterative strategy. Thus, we consider the GBT incremental formulation, defined by

$$\Delta f^{\text{int}} = \Delta f \Leftrightarrow K_{\tan}\Big|_j \Delta d = \Delta\lambda \bar{f},\ K_{ik,\tan}\Big|_j = K^{xx}_{ik,\tan} + K^{ss}_{ik,\tan} + K^{xs}_{ik,\tan} \tag{1}$$

where f^{int} is the internal force vector, λ is the load parameter and $K_{\tan}$ is the tangent stiffness matrix at the j^{th} equilibrium configureuration. Furthermore, the component $i-k$ of the tangent stiffness matrix is a 4×4 sub-matrix related to modes i and k[7]. In addition, it is worth pointing out that the FE approximation is based on Hermite cubic polynomials (see[5]) and that the expressions presented in[7] are not valid for axial and warping shear modes①. Finally, it is also necessary to define the internal force vector at an arbitrary equilibrium configureuration. For all the modes displaying in-plane displacements, the component k of the elementary internal force vector at the j^{th} equilibrium configureuration (4×1 sub-vector) is obtained from

$$f^{\text{int}}_k\Big|_j = \int_{L_e}\left\{F_{(xx)k}\left(\psi^k_{H,xx}\right)^T + F_{(ss)k}\left(\psi^k_H\right)^T + F_{(xs)k}\left(\psi^k_{H,x}\right)^T\right\}\mathrm{d}x \tag{2}$$

$$F_{(xx)k} = \int_b\int_e E_{(ss)k}\sigma_{xx}\Big|_j \mathrm{d}z\mathrm{d}s \qquad F_{(ss)k} = \int_b\int_e E_{(ss)k}\sigma_{ss}\Big|_j \mathrm{d}z\mathrm{d}s \qquad F_{(xs)k} = \int_b\int_e E_{(xs)k}\sigma_{xs}\Big|_j \mathrm{d}z\mathrm{d}s \tag{3}$$

where σ_{mn} is a generic 2nd Piolla-Kirchhoff stress component, E_{mn} are sectional deformations (not strains) and Ψ_H are Hermite cubic polynomials. Concerning the plasticity model, the J_2-flow theory with the associated flow rule was adopted[9]. In order to compute the tangent stiffness matrix, the consistent elastic-plastic constitutive matrix $D^{ep\,*}$ was used[7], since it is known that it reduces the computational cost of the incremental-iterative procedure, when compared to the conventional constitutive matrix[9]. In order to compute the internal force vector (Eqs. (2)-(3)), one must be able to update the stresses and the plastic proportional factor at any equilibrium configureuration. For that purpose, a robust return-mapping scheme should be used for those points (configureurations) undergoing plastic flow during a deformation increment. In this work, the Euler-backward method based on a Newton-Raphson scheme was considered[9]. The GBT formulation was implemented using MATLAB[10].

ILLUSTRATIVE EXAMPLE

Now, an illustrative example is presented and the GBT results are compared with those yielded by ABAQUS SFEA[6]. We consider the simply supported Z-section beam depicted in Figure 2 which has length $L = 1\,200$ mm and the cross-section (mid-line) dimensions shown in Figure 2(a), and is acted by a uniformly distributed load $p = 0.1\lambda$ N/mm^2 (Figure 2(b)) applied at both flanges (Figure 2(a)). The cold-formed steel is modeled as an isotropic linear elastic-perfectly plastic material with Young's modulus

① *The components i-k due to those modes are obtained by replacing the corresponding vectors Ψ (Hermite shape functions) and their derivatives by vectors with one order of differentiation below.*

$E = 200\,000$ N/mm^2, Poisson's ratio $v = 0.3$ and uniaxial nominal yield stress $\sigma^y = 450$ N/mm^2. A total of 9 nodes were used to discretise the Z-section (see Figure 3), involving $7 \times 5 + 2 \times 6 = 47$ dof - recall that the 2 nodes located at the Z-section corners have 6 dof, corresponding to 3 displacements, 1 flexural rotation and 2 warping rotations (each of them orthogonal to a converging wall). The eigenvalue problem (cross-section analysis) provides 47 deformation modes: 4 global modes, 16 local modes, 19 warping shear modes and 8 transverse extension modes. Due to the minute contribution of 10 deformation modes, only the remaining 37 modes were included in the member analysis - the most relevant are represented in Figure 3. Regarding the FE models, (i) 15 beam FEs were used in the GBT analysis and (ii) 94 "transverse rows" of 14 shell FEs were considered to obtain the ABAQUS results. Concerning the numerical integration, 5 Gauss points were used by both the GBT FE model, in all directions (s, z, x) and the SFE model, in the through-thickness direction.

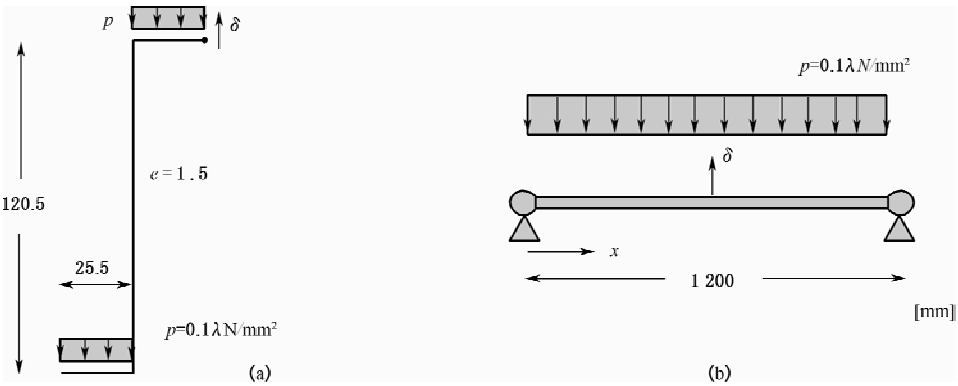

(a) Z-section geometry and loading (b) Structural model

Figure 2

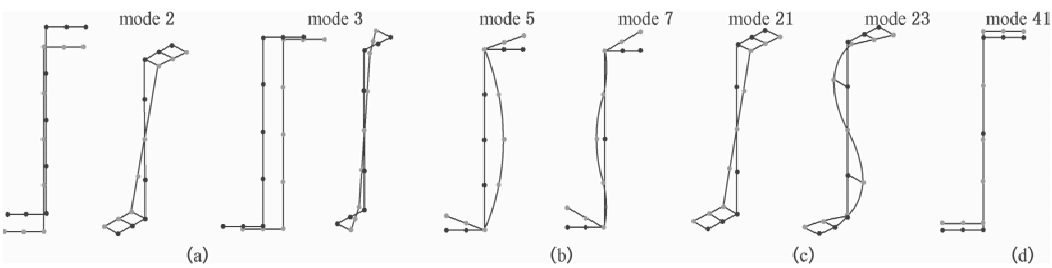

(a) Global (2, 3-major and minor axis bending) (b) Local (5, 7) (c) Warping shear (21, 23), (d) Transv. extension (41) modes.

Figure 3

Figure 4(a) presents the equilibrium paths $\lambda(\delta)$ obtained from the GBT (circles) and ABAQUS (triangles) analyses, where δ is the vertical displacement at the mid-span top flange edge node (Figure 2(a)) ($x = 600$ mm - Figure 2(b)). In order to compare the GBT and ABAQUS results, three equilibrium configureurations were selected: A (elastic), B (elastic-plastic) and C (plastic). It is seen that the GBT and SFE (ABAQUS) curves compare very well, with a maximum difference of 1.5%. In particular, the load parameter values at the 3 equilibrium configureurations A, B and C (see Figure 4(a)) are (i) $\lambda_{GBT} = 0.39$ and $\lambda_{SFE} = 0.39$ (A), (ii) $\lambda_{GBT} = 3.38$ and $\lambda_{SFE} = 3.36$ (B), and (iii) $\lambda_{GBT} = 3.63$ and $\lambda_{SFE} = 3.59$ (C). Using GBT, the yield load is $p_y \approx 0.233$ N/mm^2 ($\lambda \approx 2.33$) and the ultimate load is $p_u = 0.363$ N/mm^2 (λ

=3.63), corresponding to a shape factor $S = p_u / p_y = 1.56$. The GBT modal participation diagram is displayed in the bottom of Figure 4(a) and shows that the most relevant modes are mode 2 (major axis bending), with a participation between 12.53% ~ 13.28%, mode 3 (minor axis bending), with 73.30%~76.46% participation, and mode 5 (local), with 8.24%~9.25% participation - note that the participations of these modes change slightly along the whole equilibrium path. It should be noticed that mode 7, which has a negligible participation in the elastic regime, increases its contribution in the elastic-plastic and plastic phases to 3.83%. The ABAQUS and GBT beam deformed shapes at collapse (configureuration C), shown in Figure 4(b), are very similar - note that the deformed shape on the right side of Figure 4(b) is not a SFE representation, but a 3D view obtained from a beam theory that includes local deformations (GBT). Despite the load being vertical, it is interesting to highlight the huge lateral (horizontal) displacement at failure, mostly due to the participation of mode 3 (minor-axis bending). Notice also the local deformation at mid-span, involving flange rotations in opposite senses and web transverse bending, mostly due to the contribution of modes 5 and 7.

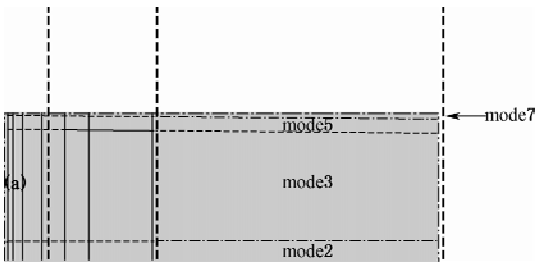

(a) Equilibrium path and modal participation diagram

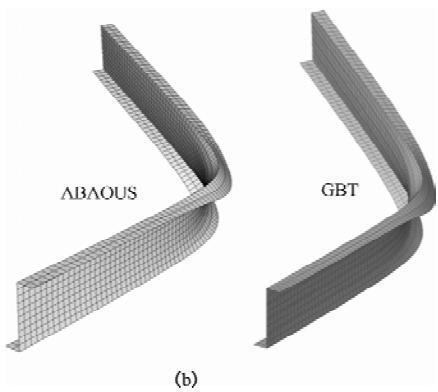

(b) beam deformed shapes at collapse (configureuration C).

Figure 4

Figures 5(a)-(b) and 6(a)-(b) show the variation of the modal amplitude functions along the beam length; while Figures 5(a) and 6(a) provide the amplitude variation ($\zeta_{k,x}(x)$) of the warping shear modes 21 and 23 (see Figure 3(c)), Figures 5(b) and 6(b) depict the variation ($\zeta_k(x)$) of the global (2 and 3-see Figure 3(a)) and local (5 and 7-see Figure 3(b)) modes. Although transverse extension modes (see Figure 3(d)) were also included in the analysis (they play an important role in the beam behaviour, especially in the plastic regime), their amplitudes are negligible when compared to those of global, local and shear modes. In configureuration A (elastic-Figure 5(a)), (i) the warping shear modes 21 and 23 vary linearly along the beam axis, in accordance with classical beam theory (note that mode 21 contributes to the web shear deformations and mode 23 contributes to both the web and flange shear deformation-see Figure 3(c)), (ii) the global modes 2 and 3 vary cubically along the beam axis, also in accordance with classical beam theory, and (iii) the local modes 5 and 7 exhibit a very smooth variation: they vary considerably near the supports ($0 \leqslant x \leqslant 150$ mm; $1\,050 \leqslant x \leqslant 1\,200$ mm) but remain almost uniform in a large fraction of the beam span ($150 \leqslant x \leqslant 1\,050$ mm)-note that the variation of mode 3 is larger than that of mode 2, due to the lower second moment of area. In configureuration C (plastic-Figure 6(a)), (i) the warping shear modes 21 and 23 still vary linearly along the beam axis, but only in the elastic and elastic-plastic zones ($0 \leqslant x \leqslant 400$ mm; $800 \leqslant x \leqslant 1\,200$ mm), showing a very pronounced non-linear variation with x where plasticity is spreading ($400 \leqslant x \leqslant 800$ mm), (ii) the global modes 2 and

3 vary almost linearly in the elastic and elastic-plastic zones ($0 \leqslant x \leqslant 400$ mm; $800 \leqslant x \leqslant 1\,200$ mm), but show a high non-linear variation in the mid-span zone ($400 \leqslant x \leqslant 800$ mm), where plasticity controls, and (iii) the participations of local modes 5 and 7 decrease in the elastic and elastic-plastic zones ($0 \leqslant x \leqslant 400$ mm; $800 \leqslant x \leqslant 1\,200$ mm), but increase in the mid-span plastic zone ($400 \leqslant x \leqslant 800$ mm). This shows that local modes influence the beam plastic resistance, as they are associated with very strong web transverse bending, which erodes the beam strength in the mid-span zone, as can be observed in Figure 4(b).

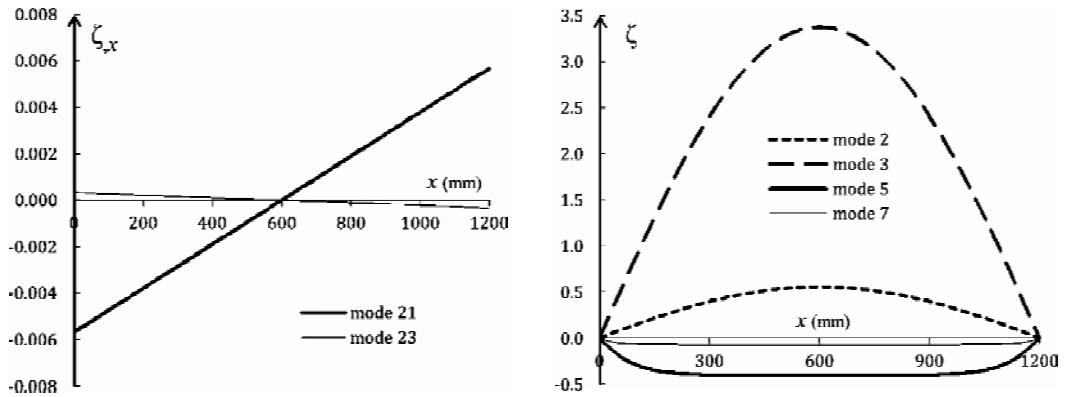

Figure 5 Variation of modal amplitude functions at configureuration A: (a) warping shear and (b) global and local modes.

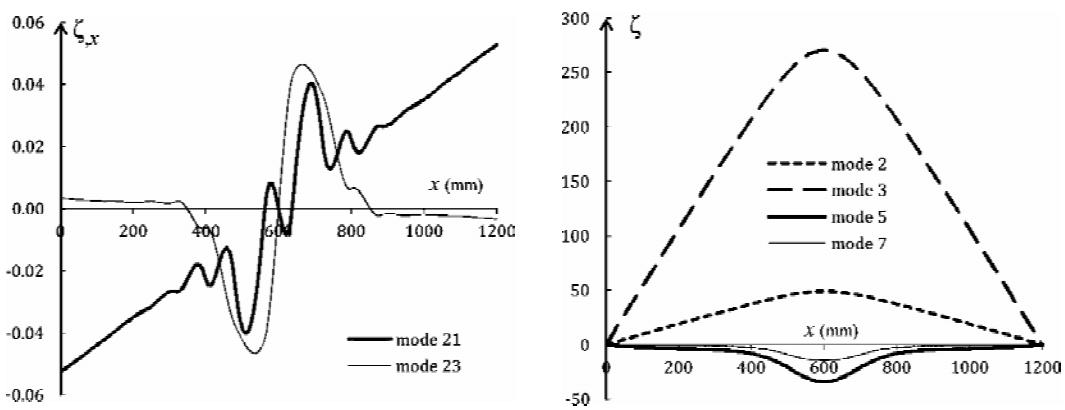

Figure 6 Variation of modal amplitude functions at configureuration C: (a) warping shear and (b) global and local modes.

Since the warping displacements are given by $u = u_k(s)\zeta_{k,x}(x)$, Figure 7 shows the variation of the warping shear modes (already depicted in Figure 6(a)), as well as the derivatives $\zeta_{k,x}(x)$ of global modes 2 and 3, for configureuration C (plastic). Note that the warping displacements remain almost unchanged in the elastic and elastic-plastic zones ($0 \leqslant x \leqslant 400$ mm; $800 \leqslant x \leqslant 1\,200$ mm) but vary a lot (even change sign) in the plastic mid-span zone ($400 \leqslant x \leqslant 800$ mm)-they are null at the mid-span section ($x = 600$ mm).

For the three equilibrium configureurations (A, B, C), Figure 8(a) depicts the variation of the vertical displacement δ of the top flange edge node (Figure 2(a)) along the beam axis ($0 \leqslant x \leqslant 1\,200$ mm). While the GBT and ABAQUS displacement profiles are nearly coincident at A and C, a maximum difference of

3% occurs at B. Note that the curve $\delta(x)$ concerning configureuration C is almost straight for $0 \leqslant x \leqslant 400$ mm and $800 \leqslant x \leqslant 1\,200$ mm but is quite non-linear in the mid-span zone ($400 \leqslant x \leqslant 800$ mm). This shows that the former zones are still in the elastic or elastic-plastic regimes, while the latter is fully yielded (forms a "plastic hinge"). Figure 8(b) displays the Mises stress diagrams at mid-span for the configureurations A, B and C. Once again, the GBT and ABAQUS results exhibit a quite satisfactory agreement. In configureuration A (elastic), the maximum stress takes place at the web-flange node, while nearly null values occur at the web and flange mid-points. In configureuration B (elastic-plastic), the minimum stress takes place at the web central and flange edge zones, while it equals the yield stress in the remaining Z-section zones. In configureuration C (plastic), the stress equals the yield stress in practically the whole Z-section (except in part of the flanges, for the ABAQUS diagram).

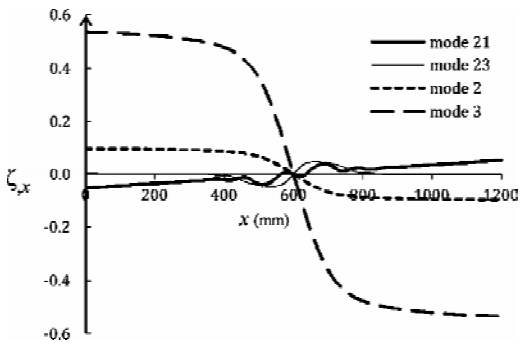

Figure 7 Derivative of the amplitude functions $\zeta_k(x)$ of the global and warping shear modes (configureuration C).

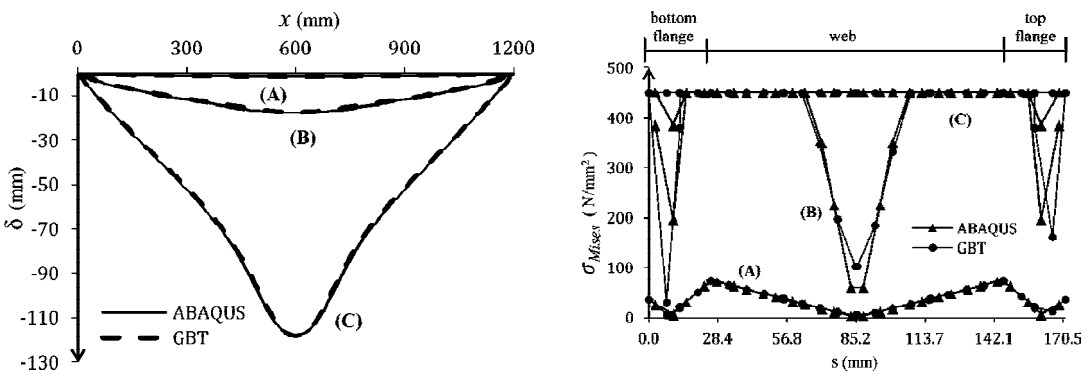

Figure 8 (a) Longitudinal variation of the vertical displacement of the flange edge node and (b) Mises stress (σ_{Mises}) diagram for configureurations A, B and C (mid-span section x=596 mm).

Figures 9(a)-(b) provide the axial stress diagrams at the mid-span section for configureurations A and B (Figure 9(a)), and C (Figure 9(b)), and show that there is a quite satisfactory resemblance between the ABAQUS and GBT results. From the observation of these figureures, it is concluded that plasticity spreads from the web-flange nodes to inside the web width and the flange edge. Figures 9(a)-(b), show that the neutral axis passes through the Z-section centroid and crosses both flanges - note that the flange tips and flange internal zones yield under axial stresses with opposite signs. It is also clear that the neutral axis location remains practically unaltered as the beam evolves from configureuration A (elastic) to configureuration C (plastic).

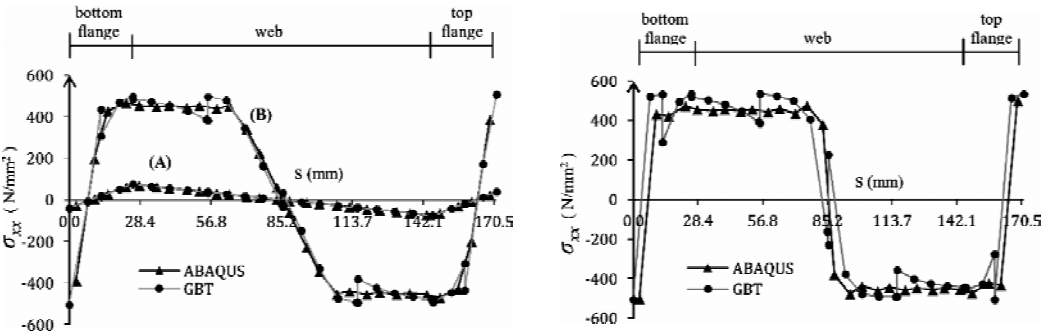

Figure 9 Axial stress (σ_{xx}) diagrams for configureurations (a) A, B and (b) C (mid-span section x=596 mm).

The shear and Mises stress contours at configureuration C (plastic), presented in Figures 10 and 11, provide further evidence of the similarity between the ABAQUS and GBT results. The sole exception is the small fluctuation of the GBT shear stress magnitude near mid-span, which disappears if a more refined FE is adopted at the mid-span zone. Figure 11 confirms the previous assertion that the mid-span zone ($400 \leqslant x \leqslant 800$ mm) is fully yielded, while the outer zones remain elastic ($0 \leqslant x \leqslant 200$ mm and $1\,000 \leqslant x \leqslant 1\,200$ mm) or elastic-plastic ($200 \leqslant x \leqslant 400$ mm and $800 \leqslant x \leqslant 1\,000$ mm).

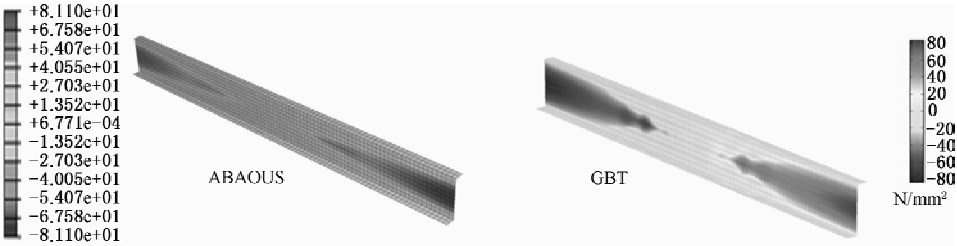

Figure 10 Shear stress (σ_{xs}) contour at configureuration C.

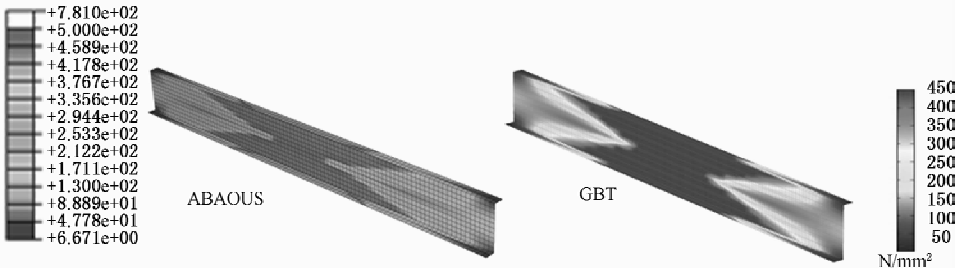

Figure 11 Mises stress (σ_{Mises}) contour at configureuration C.

CONCLUSIONS

A GBT elastic-plastic formulation was employed to perform a first order elastic-plastic analysis of a cold-formed simply supported Z-section steel beam subjected to a uniformly distributed load. The results presented consisted of (i) load-deflection curves (equilibrium paths), (ii) displacement longitudinal profiles, (iii) axial, shear and Mises stress diagrams, including 3D contours, and (iv) 3D deformed

configureurations. In order to highlight the modal nature of GBT, the variation of modal participation along the equilibrium path was shown, as well as the shapes of the modal amplitude functions-for this purpose, GBT results concerning three distinct equilibrium configureurations (elastic, elastic-plastic and plastic) were presented. All these results, found to be in very good agreement with those provided by ABAQUS (the best correlation was obtained for the equilibrium paths and displacement profiles-differences always below 3%), were discussed in great detail and revealed the potential of the proposed approach to provide in-depth insight on the spread of plasticity and formation of plastic mechanisms. Finally, it is important to highlight that, in the illustrative example shown, the number of d.o.f required by the ABAQUS SFEA was 7.4 times higher than that involved in using the GBT model, which attests the computational efficiency of GBT analyses.

REFERENCES

[1] Camotim, D., Basaglia, C., Bebiano, R., Gonçalves, R. and Silvestre N., "Latest developments in the GBT analysis of thin-walled steel structures", Proceedings of International Colloquium on Stability and Ductility of Steel Structures (SDSS'Rio 2010-Rio de Janeiro, 8-10/9), E. Batista, P. Vellasco, L. Lima (eds.), 2010, 33-58(1).

[2] Gonçalves, R. and Camotim, D., "GBT local and global buckling analysis of aluminium and stainless steel columns", Computers and Structures, 2004, 82(17-19), pp.1473-1484.

[3] Gonçalves, R. and Camotim, D., "Generalised beam theory-based finite elements for elastoplastic thin-walled metal members", Thin-Walled Structures, 2011, 49(10), pp.1237-1245.

[4] Gonçalves, R. and Camotim, D., "Geometrically non-linear generalised beam theory for elastoplastic thin-walled metal members", Thin-Walled Structures, 2012, 51, pp.121-129.

[5] Abambres, M., Camotim, D. and Silvestre, N., "Elastoplastic analysis of thin-walled bars in the context of generalised beam theory "(in Portuguese), Numerical Methods in Engineering 2011 (CMNE 2011-Coimbra, 14-17/6), A. Tadeu et al. (eds.), (2011), 151. (full paper in CD-ROM Proceedings) (Portuguese)

[6] DS Simulia Inc, ABAQUS Standard (version 6.5), (2004).

[7] Abambres, M., Camotim, D., Silvestre, N., "Physically non-linear analysis of steel beams in the context of GBT", Proceedings of Ⅷ Congress on Steel and Composite Construction (CMM Ⅷ-Guimarães, 24-25/11), L. Silva et al. (eds.), (2011), pp. Ⅱ-295- Ⅱ-304. (Portuguese)

[8] Silva, N.F., Camotim, D. and Silvestre, N., "GBT cross-section analysis of thin-walled members with arbitrary cross-sections: a novel approach", Proceedings of Fifth International Conference on Thin-Walled Structures - Recent Innovations and Developments (ICTWS 2008-Brisbane, 18-20/6), M. Mahendran (ed.), (2008), pp. 1189-1196 (vol. 2).

[9] De Borst R. and Sluys, L.J., "Computational Methods in Non-linear Solid Mechanics, Koiter Institute", Delft University of Technology, 2007.

[10] MathWorks, MATLAB - The Language of Technical Computing, 1998.

Proceedings of Seventh International Conference on Advances in Steel Structures, 2012, Nanjing, China

DIRECT STRENGTH DESIGN OF HIGH STRENGTH COMPLEX C-SECTIONS IN PURE BENDING

* C. H. Pham and G. J. Hancock

School of Civil Engineering, Faculty of Engineering and Information Technologies, The University of Sydney, NSW 2006, Australia.

* Email: caohung.pham@sydney.edu.au

KEYWORDS

Direct strength method, high strength steel, cold-formed channel, complex sections, pure bending.

ABSTRACT

Plain C-or Z-sections are two of the most common cold-formed steel shapes in use throughout the world. Other shapes are high strength SupaCee® and SupaZed® steel sections which are widely used in Australia as purlins in roof and wall systems. They contain additional return lips and web stiffeners which enhance the bending capacity of the sections. Design methods for these sections are normally specified in the Australian/New Zealand Standard for Cold-Formed Steel Structures (AS/NZS 4600:2005)[1] or the North American Specification for Cold-Formed Steel Structural Members[2]. In both Standards, which include the newly developed Direct Strength Method of design (DSM), the method presented (Chapter 7 of AS/NZS 4600:2005[1], Appendix 1 of AISI[2]) is developed for beams and columns, including the reliability of the method. This paper presents two different test series on both plain C- and SupaCee® sections in pure bending. They were performed at the University of Sydney for the extension of the DSM to include channel section beams with complex stiffeners. Two different section depths and three different thicknesses of high strength lipped channel sections were tested in pure bending. Tests with and without torsion/distortion restraint straps screwed on the top flanges in the pure bending region were also considered to allow local and distortional buckling to form in the sections respectively. Test results and formulae developed from the DSM are summarized in the paper. Three different cases where moments are used in association with yield, inelastic or plastic criteria in the DSM local and distortional strength equations are compared with the test data.

INTRODUCTION

Roof systems composed of high tensile steel profiled sheeting screw-fastened to cold formed steel purlins of high strength steel are widely used in civil construction. Two of the most common purlins employed in these applications are the C- and Z-sections. In Australia, the new SupaCee® and SupaZed® steel purlin profiles developed by Bluescope Lysaght and the University of Sydney[3] give higher capacities and more economical solutions. The longitudinal web stiffeners and return lip stiffeners of these sections significantly improve the performance when bending capacity governs. Currently, two basic design

methods for cold-formed steel members are formally available in the Australian/New Zealand Standard for Cold-Formed Steel Structures (AS/NZS 4600:2005)[1] or the North American Specification for Cold-Formed Steel Structural Members[2]. They are the traditional Effective Width Method (EWM) and the newly developed Direct Strength Method of design (DSM) (Chapter 7 of AS/NZS 4600: 2005[1], Appendix 1 of AISI[2]). As sections become more complex with additional multiple longitudinal web stiffeners and return lips as designed on SupaCee® and SupaZed® sections, the computation of the effective widths becomes more complex. For the EWM, the calculation of effective widths of the numerous sub-elements leads to severe complications with decreased accuracy. In some special cases, no design approach is even available for such a section using the EWM. The DSM appears to be more beneficial and simpler by using the elastic buckling stresses of the whole sections such as the SupaCee® and SupaZed®. There is no need to calculate cumbersome effective sections especially with intermediate stiffeners.

In the development of the DSM, Yu and Schafer conducted two series of flexural tests and finite element analyses on variety of C- and Z-Sections in local buckling[4] and distortional buckling[5]. Those series aimed at isolating the local and distortional modes used in verifying the DSM. Recently, additional tests on distortional buckling have also been conducted by Javaroni and Goncalves[6]. The main purpose of this paper is to provide additional experimental data on channel sections in pure bending performed at the University of Sydney. Both plain C- and SupaCee® sections were tested in the four point bending arrangement. Two different depths and three different thicknesses of each type of channels were tested in the above series. Half of the tests were conducted with straps attached on the top flanges in the pure bending region by self-tapping screws. The straps allowed the channels to buckle in local buckling modes. The remaining tests were tested without those straps on the top flanges which allowed distortional buckling failures. The current DSM is based on the yield moment (M_y) of the sections. However, a recent proposal by Shifferaw and Schafer[7] allows an inelastic moment (M_n) to be used. Another alternative is the plastic moment (M_p). The test results are plotted against the DSM local and distortional curves for beams where the three cases associated with yield (M_y), inelastic (M_n) and plastic (M_p) moments are used for comparison.

EXPERIMENTS ON PLAIN LIPPED C- AND SUPACEE® SECTIONS IN PURE BENDING

Tests Specimens and Experimental Rig

The experimental program comprised a total of twenty four tests (12 for plain C-lipped sections and 12 for SupaCee® sections) conducted in the J. W. Roderick Laboratory for Materials and Structures at the University of Sydney. All tests were performed in the 2 000 kN capacity DARTEC testing machine, using a servo-controlled hydraulic ram. A diagram of the test set-up for the common four point loading configuration is shown in Figure 1. Two different commercially available plain C-lipped and SupaCee® sections of 150 and 200 mm depths as shown in Figure 2(a) were chosen with three different thicknesses of 1.5, 1.9 and 2.4 mm (for plain C-lipped sections) and 1.2, 1.5 and 2.4 mm (for SupaCee® sections). The average measured dimensions and properties for the bending series of both plain C-lipped and SupaCee® sections are given in Pham and Hancock[8, 9] respectively.

Tests With and Without Straps Configurations

Twelve tests (6 of plain C-lipped sections and 6 of SupaCee® sections) had eight 25 × 25 × 5EA straps connected by self-tapping screws on the top flanges which were uniformly distributed in the pure bending

moment region between the two loading points as shown in Figure 2(b). The purpose of the straps is to force the channel members to buckle locally rather than by distortional buckling. The remaining tests were tested without the six middle 25×25×5EA straps as shown in Figure 2(c). Only two straps adjacent to the loading points were attached to the channel members to prevent distortion at the loading points.

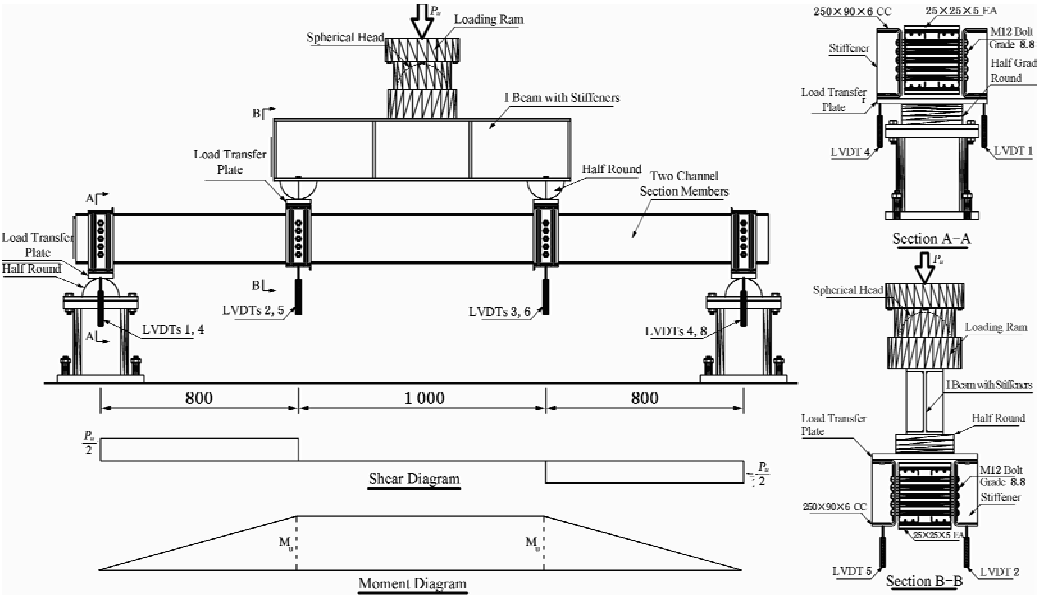

Figure 1 Bending test set-up configuration (dimensions for 200 mm deep section)

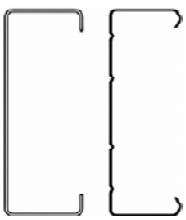

(a) Plain and SupaCee® Channel Sections

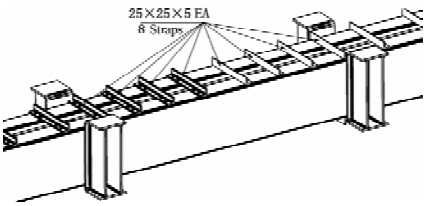

(b) Test With Straps

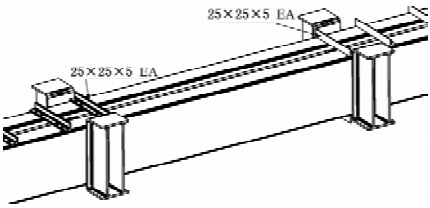

(c) Test Without Straps

Figure 2 Bending test set-up configuration-tests with and without straps

ELASTIC INSTABILITIES FOR THE CHANNEL CROSS-SECTIONS

Cold-formed thin-walled channel purlins may undergo one of the three modes of local, distortional and lateral-torsional buckling or combinations of these. The Semi-Analytical Finite Strip Method (SAFSM)

developed by Cheung[10] has been widely used in computer software (THIN-WALL, CUFSM) to develop the signature curve of buckling stress versus buckling half-wavelength for thin-walled sections under compression and bending to allow identification of these modes. Figure 3 shows the signature curves of both plain lipped C- (C20015) and SupaCee® (SC20015) sections in bending for comparison.

As can be seen in Figure 3, the buckling stresses associated with both the local and distortional buckling modes of SC20015 increase significantly compared with those of C20015 where the areas of these two sections are almost the same. The reason for this fact is due to four additional longitudinal web stiffeners and the return lips. They enhance the bending capacity of the sections for both local and distortional modes at short and intermediate half-wavelength respectively. Meanwhile, the buckling stresses for the lateral-torsional mode in one half-wave over the unbraced length of the purlins are almost unchanged. The minimum points of these curves are used in the Direct Strength Method (DSM) of design of cold-formed sections. Determination of the bending strength capacity requires consideration of these cross section instabilities, post-buckling characteristics, interaction between modes, and material yielding.

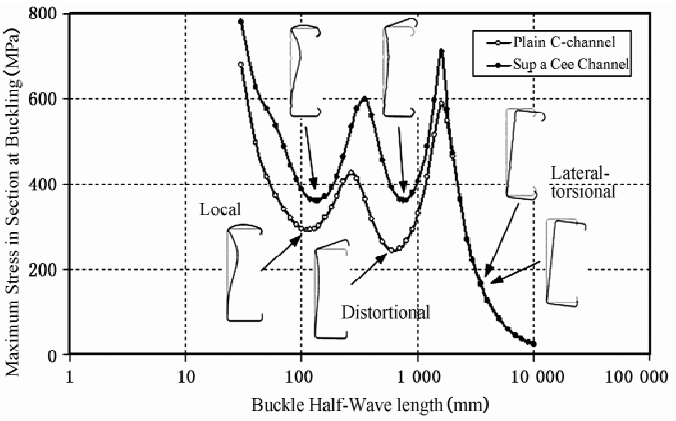

Figure 3 Buckling modes of cold-formed plain C- and supacee® sections

DIRECT STRENGTH METHOD (DSM) RULES OF DESIGN FOR FLEXURE

Local Buckling Strength

The nominal section moment capacity at local buckling(M_{sl}) is determined from Section 7.2.2.3 of AS/NZS 4600:2005 (Appendix 1, Section 1.2.2.2 of AISI[2]) as follows:

$$\text{For } \lambda_l \leqslant 0.776 : M_{sl} = M_y \tag{1}$$

$$\text{For } \lambda_l > 0.776 : M_{sl} = \left[1 - 0.15\left(\frac{M_{ol}}{M_y}\right)^{0.4}\right]\left(\frac{M_{ol}}{M_y}\right)^{0.4} M_y \tag{2}$$

where λ_l is non-dimensional slenderness used to determine M_{sl}; $\lambda_l = \sqrt{M_y / M_{ol}}$; $M_y = Z_f f_y$,
M_{ol} is elastic local buckling moment of the section; $M_{ol} = Z_f f_{ol}$,
Z_f is section modulus about a horizontal axis of the full section,
f_{ol} is elastic local buckling stress of the section in bending.

Distortional Buckling Strength

The nominal section moment capacity at distortional buckling (M_{sd}) is determined from Section 7.2.2.4 of AS/NZS 4600:2005 (Appendix 1, Section 1.2.2.3 of AISI[2]) as follows:

$$\text{For } \lambda_d \leqslant 0.673\text{: } M_{sd} = M_y \tag{3}$$

$$\text{For } \lambda_d > 0.673\text{: } M_{sd} = \left[1 - 0.22\left(\frac{M_{od}}{M_y}\right)^{0.5}\right]\left(\frac{M_{od}}{M_y}\right)^{0.5} M_y \tag{4}$$

where λ_d is non-dimensional slenderness used to determine M_{sd}; $\lambda_l = \sqrt{M_y/M_{od}}$; $M_y = Z_f f_y$,
M_{od} is elastic distortional buckling moment of the section; $M_{od} = Z_f f_{od}$,
Z_f is section modulus about a horizontal axis of the full section,
f_{od} is elastic distortional buckling stress of the section in bending.

Inelastic Buckling Strength

Although cold-formed thin-walled steel sections may fail due to numerous cross-section buckling modes, they still may develop inelastic reserve capacity. Shifferaw and Schafer[7] provided and verified a general method for prediction of inelastic bending capacity of cold-formed steel members. The methodology was based on an extensive experimental data base and nonlinear finite element models. The design approach for the inelastic lateral-torsional buckling is provided based on the hot-rolled steel AISC Specification. The resulting relationships for inelastic local and distortional buckling are provide in a DSM format for adoption in the AISI Specifications as follows:
For $\lambda_l \leqslant 0.776$ and $\lambda_d \leqslant 0.673$, and sections symmetric about the axis of bending:

$$M_n = M_y + \left(1 - 1/C_y^2\right)\left(M_P - M_y\right) \tag{5}$$

where $\lambda_l = \sqrt{M_y/M_{ol}}$, $\lambda_d = \sqrt{M_y/M_{od}}$, $C_{yl} = \sqrt{0.776/\lambda_l} \leqslant 3$, $C_{yd} = \sqrt{0.673/\lambda_d} \leqslant 3$
M_y is yield moment, M_p is plastic moment equal to $S_f f_y$ where S_f is the plastic section modulus of the full section.

COMPARISONS OF DSM DESIGN LOADS WITH TESTS

The full set of test results for the plain lipped C- and SupaCee® sections is given in the research reports by Pham and Hancock[8, 9]. Figures. 4(a) and 4(b) show the corresponding local and distortional buckling mode shapes of plain C-members (C20015) with and without straps. The results of tests are summarized in Tables 1 and 2 for the local and distortional buckling tests respectively. In each table, the test moments are compared with existing local and distortional DSM design curves in three different cases namely *Case A*, *Case B* and *Case C*. The comparisons with the test data are also provided graphically in Figures 5(a), 5(b) and 5(c) respectively. In *Case A*, the yield moment (M_y) is used in both horizontal axis for non-dimensional slenderness ($\lambda_l = \sqrt{M_y/M_{ol}}$ and $\lambda_d = \sqrt{M_y/M_{od}}$) and vertical axis for test to predicted capacities (M_T/M_y) as defined in existing DSM rules. In *Case B*, while the non-dimensional slenderness is unchanged in the horizontal axis, the yield moment (M_y) in vertical axis is replaced by inelastic bending moment (M_n) given by Eqn. (5) to take into account the effect of inelastic reserve capacity. For *Case C*, the yield moment (M_y) is replaced by the plastic moment (M_p) in both axes so that $\lambda_{lp} =$

$\sqrt{M_p/M_{ol}}$ and $\lambda_{dp} = \sqrt{M_p/M_{od}}$ as plastic slenderness.

For the local buckling tests, it can be seen in Table 1 that the means of test results divided by the DSM design local buckling predicted capacities are conservative (1.135 and 1.127) for both *Case A* and *Case B*. The corresponding coefficients of variations are 0.062 and 0.055 respectively. The reason for the slightly different results from *Case A* and *Case B* is due to the two stocky section tests (C15024 and SC15024) which have the non-dimensional slenderness ($\lambda_l = \sqrt{M_y/M_{od}}$) in the inelastic local buckling reserve range ($\lambda_l \leqslant 0.776$) so that Eqn. (5) can be used. For *Case C*, the results are better predicted (the mean = 1.005) by using M_p instead of M_y. The standard deviation for this case is quite low at 0.044.

For the distortional buckling tests, Table 2 shows the same means of test results divided by the DSM design distortional buckling predicted capacities of 1.152 for both *Case A* and *Case B*. This is due to the fact that no sections have the non-dimensional slenderness ($\lambda_d = \sqrt{M_y/M_{od}}$) in the inelastic distortional buckling reserve range ($\lambda_d \leqslant 0.673$). In *Case C*, the DSM also provides better strength predictions for the distortional buckling failures (the mean = 1.038) when M_p is replaced by M_y in comparison with that of *Case A* and *Case B* (the mean = 1.152). The corresponding standard deviation for *Case C* is reasonably low at 0.090 compared with 0.096 for both *Case A* and *Case B*.

TABLE 1 LOCAL BUCKLING TESTS OF PLAIN C- AND SUPACEE® SECTIONS-WITH STRAPS

Section	M_T (kNm)	$\lambda_l = \sqrt{\frac{M_y}{M_{ol}}}$	$\lambda_{lp} = \sqrt{\frac{M_p}{M_{ol}}}$	Case A		Case B		Case C	
				$\frac{M_T}{M_y}$	$\frac{M_T}{M_{sl}}$	$\frac{M_T}{M_n}$	$\frac{M_T}{M_{sl}}$	$\frac{M_T}{M_p}$	$\frac{M_T}{M_{sl}}$
C15015	10.43	1.063	1.138	0.890	1.090	0.890	1.090	0.777	0.996
C15019	15.86	0.841	0.901	1.079	1.135	1.079	1.135	0.940	1.033
C15024	19.84	0.629	0.676	1.178	1.178	1.145	1.145	1.020	1.020
C20015	13.47	1.326	1.425	0.745	1.060	0.745	1.060	0.645	0.965
C20019	21.76	1.060	1.138	0.930	1.137	0.930	1.137	0.808	1.035
C20024	31.39	0.807	0.868	1.135	1.163	1.135	1.163	0.982	1.054
SC15012	8.19	1.139	1.235	0.832	1.068	0.832	1.068	0.708	0.960
SC15015	11.40	0.911	0.996	1.036	1.148	1.036	1.148	0.868	1.018
SC15024	21.19	0.613	0.689	1.220	1.220	1.157	1.157	0.968	0.968
SC20012	10.71	1.551	1.685	0.645	1.024	0.645	1.024	0.547	0.921
SC20015	16.48	1.215	1.327	0.890	1.194	0.890	1.194	0.746	1.063
SC20024	33.82	0.784	0.877	1.195	1.203	1.195	1.203	0.956	1.032
				Mean	1.135	Mean	1.127	Mean	1.005
				STDEV	0.062	STDEV	0.055	STDEV	0.044

TABLE 2 DISTORTIONAL BUCKLING TESTS OF PLAIN C- AND SUPACEE® SECTIONS-WITHOUT STRAPS

Section	M_T (kNm)	$\lambda_d = \sqrt{\frac{M_y}{M_{od}}}$	$\lambda_{dp} = \sqrt{\frac{M_p}{M_{od}}}$	Case A		Case B		Case C	
				$\frac{M_T}{M_y}$	$\frac{M_T}{M_{sd}}$	$\frac{M_T}{M_n}$	$\frac{M_T}{M_{sd}}$	$\frac{M_T}{M_p}$	$\frac{M_T}{M_{sd}}$
C15015w	9.47	1.213	1.300	0.804	1.192	0.804	1.192	0.701	1.097
C15019w	12.94	1.065	1.141	0.888	1.192	0.888	1.192	0.774	1.093
C15024w	17.76	0.801	0.860	1.080	1.192	1.080	1.192	0.935	1.081
C20015w	12.20	1.444	1.552	0.672	1.145	0.672	1.145	0.582	1.053

continued

Section	M_T (kNm)	$\lambda_d = \sqrt{\frac{M_y}{M_{od}}}$	$\lambda_{dp} = \sqrt{\frac{M_p}{M_{od}}}$	Case A		Case B		Case C	
				$\frac{M_T}{M_y}$	$\frac{M_T}{M_{sd}}$	$\frac{M_T}{M_n}$	$\frac{M_T}{M_{sd}}$	$\frac{M_T}{M_p}$	$\frac{M_T}{M_{sd}}$
C20019w	18.85	1.250	1.342	0.821	1.245	0.821	1.245	0.712	1.143
C20024w	27.88	0.974	1.047	1.012	1.273	1.012	1.273	0.874	1.159
SC15012w	6.56	1.217	1.319	0.662	0.983	0.662	0.983	0.563	0.892
SC15015w	10.10	1.006	1.100	0.903	1.162	0.903	1.162	0.755	1.038
SC15024w	18.84	0.784	0.881	1.082	1.179	1.082	1.179	0.857	1.006
SC20012w	9.27	1.458	1.585	0.557	0.956	0.557	0.956	0.471	0.867
SC20015w	13.70	1.212	1.324	0.741	1.098	0.741	1.098	0.621	0.986
SC20024w	29.15	0.885	0.990	1.023	1.205	1.023	1.205	0.819	1.042
				Mean	1.152	Mean	1.152	Mean	1.038
				STDEV	0.096	STDEV	0.096	STDEV	0.090

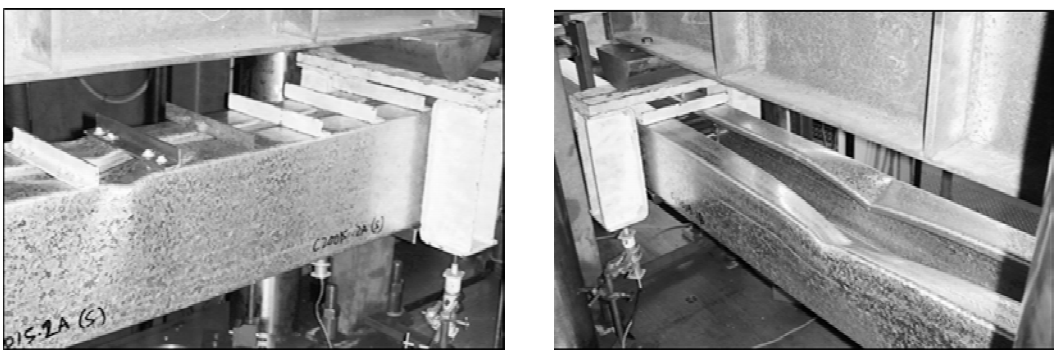

(a) With Straps (b) Without Straps

Figure 4 Local and distortional failure modes of cold-formed plain C-sections (c20015)

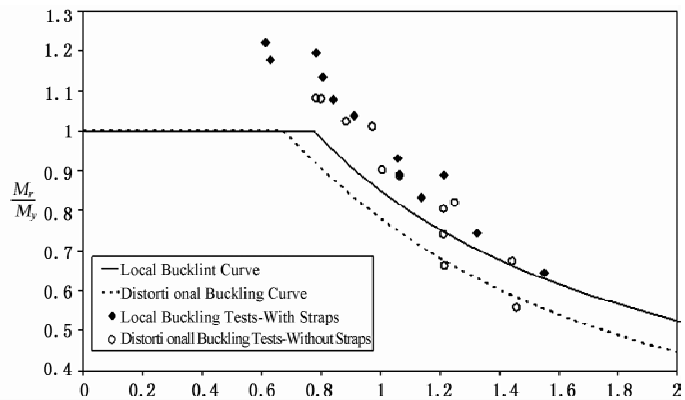

$\lambda_1 = \sqrt{\frac{M_y}{M_{ol}}}$ or $\lambda_d = \sqrt{\frac{M_y}{M_{od}}}$

(a) *Case A*

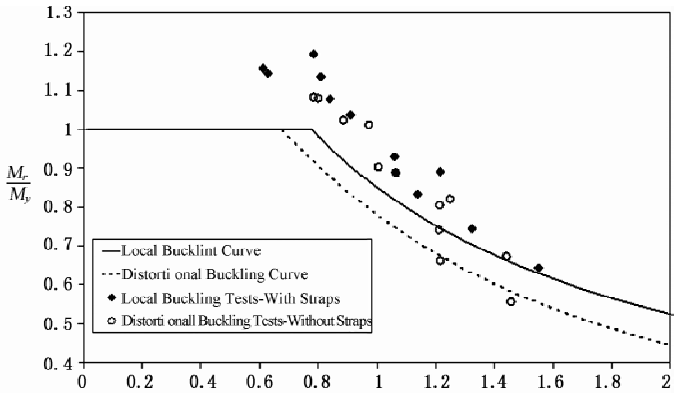

$$\lambda_l = \sqrt{\frac{M_y}{M_{ol}}} \text{ or } \lambda_d = \sqrt{\frac{M_y}{M_{od}}}$$

(b) *Case B*

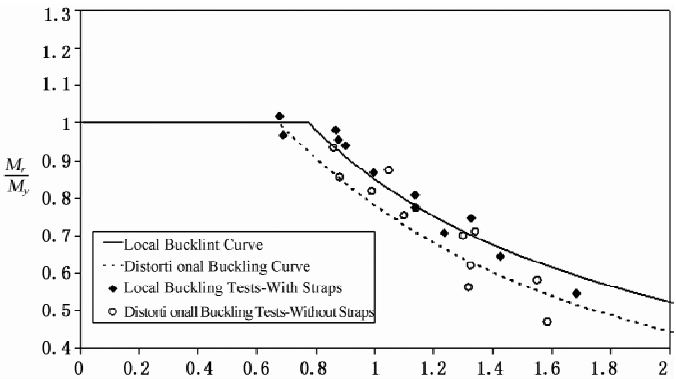

$$\lambda_{lp} = \sqrt{\frac{M_p}{M_{ol}}} \text{ or } \lambda_{dp} = \sqrt{\frac{M_p}{M_{od}}}$$

(c) *Case C*

Figure 5 Comparison of the DSM predictor curves with tests data for beam- Case A, B and C

CONCLUSION

An experimental program was carried out to determine the ultimate strength of high strength plain lipped C- and SupaCee® cold-formed channel sections subjected to pure bending. A total of twenty four tests of two different depths and three different thicknesses have been performed at the University of Sydney. While twelve tests were conducted with straps attached evenly in the pure bending region to enforce local buckling failure, the remaining tests were tested without straps to allow distortional buckling. No tests failed by lateral-torsional buckling. The test results are compared with the DSM prediction equations for both local and distortional buckling in which three different cases associated with yield, inelastic and plastic moments were considered. By comparison, the DSM when using the plastic moment (M_p) instead of the yield moment (M_y) provides good agreement with the results of both local and distortional buckling test series.

ACKNOWLEDGEMENT

The authors would like to thank Bluescope Steel for supply of the test specimens and financial support for the project performed at the University of Sydney. Thanks are also extended to all technicians at the J. W. Roderick Laboratory for Materials and Structures at the University of Sydney. The first author is supported by *GJ Hancock Innovation Fund* and *Centre for Advanced Structural Engineering* scholarships.

REFERENCES

[1] Standards Australia, "AS/NZS 4600:2005, Cold-Formed Steel Structures." Standards Australia/ Standards New Zealand, 2005.

[2] AISI, "North American Specification for the Design of Cold-Formed Steel Structural Members." 2007 Edition, AISI S100-2007, 2007.

[3] Lysaght., "NSW SupaCee® is trademark of Bluescope Steel Limited." Bluescope Steel Limited trading as Bluescope Lysaght, 2003.

[4] Yu, C. and Schafer, B. W., "Local Buckling Tests on Cold-Formed Steel Beams.", Journal of Structural Engineering, American Society of Civil Engineers, Vol.129, No12, 2003, pp.1596-1606.

[5] Yu, C. and Schafer, B.W., "Distortional Buckling Tests on Cold-Formed Steel Members in Bending.", Journal of Structural Engineering, American Society of Civil Engineers, 2006, 132(4), pp. 515-528.

[6] Javaroni, C.E. and Goncalves, R.M., "Distortional Buckling of Simple Lipped Channel in Bending Results of the experimental analysis verses Direct Strength Methods.", Proceedings, eighteenth International Specialty Conference on Cold-Formed Steel Structures, 2006, pp.133-146.

[7] Shifferaw, Y. and Schafer, B. W., "Inelastic Bending Capacity in Cold-formed Steel Members.", Structural Stability Research Council - Proceedings of the 2007 Annual Stability Conference, 2007, pp. 279-300.

[8] Pham, C. H. and Hancock, G. J., "Experimental Investigation of High Strength Cold-Formed C-Section in Combined Bending and Shear.", Research Report No R894, School of Civil Engineering, The University of Sydney, NSW, Australia, April, 2009a.

[9] Pham, C.H. and Hancock, G.J., "Experimental Investigation of High Strength Cold-Formed SupaCee® Sections in Combined Bending and Shear.", Research Report No R907, School of Civil Engineering, The University of Sydney, NSW, Australia, December, 2009b.

[10] Cheung, Y.K., "Finite Strip Method in Structural Analysis". Pergamon Press, Inc., New York, N.Y, 1976.

CALCULATION OF THE BUCKLING OF COLD-FORMED THIN GAUGE PURLINS CONNECTED TO SHEETING

* Y.Q. Chen

Zhejiang Hangxiao Steel Structure Co., Ltd., Hangzhou, 310003, China
* Email: cyq5212@126.com

KEYWORDS

Distortional buckling, flexural-torsional buckling, local post-buckling, lateral restraint, buckling length, diaphragm effect, anti-sag bar, sheeting, panel clip.

ABSTRACT

In practical engineering, the diaphragm effect of the sheeting on a roof can significantly influence the buckling of the purlins connected to the sheeting, and contributes to their stability. In the modern sliding sheeting fixed by panel clips, such diaphragm effect significantly reduces. Evaluation of the buckling effect is therefore important for the design of the purlins. However, the stability of cold-formed thin gauge purlins evades accurate evaluation, due to the complication by lateral distortional buckling, flexural-torsional buckling and local buckling. In this work we evaluated the stability of purlins using three different codes: the China code GB 50018—2002, the Euro code EC3-1-3 and the Australian/New Zealand Standard AS/NZS 4600. GB 50018—2002 factors out the diaphragm effect of the sheeting, and consequently maybe miscalculates the buckling of the purlins. EC 3-1-3 presents a method for cold-formed purlins calculating torsional restraint stiffness of the sheeting, which applies for purlins fixed to the sheeting only by self-tapping screws. AS/NZS 4600 gives different modes of buckling calculations. The three codes give equal results when there are not neither anti-sag bar nor restraint given by sheeting on the purlin, otherwise, different results occur. The result from EC3-1-3 suggests that a small increase in the torsional restraint stiffness of the sheeting leads to significant improvement of the purlin stability when the restraint stiffness is small; such dependence quickly attenuates as the restraint stiffness increases. Once the critical lateral stiffness of purlin buckling is reached, further stiffening of the sheeting restrain makes no more difference. The torsional restraint stiffness of the sliding sheeting fixed by panel clips, albeit weak, can provide significant purlin stability. The study of the diaphragm effects of roof sheeting sheds important light to the design of the purlins.

INTRODUCTION

The lateral stability of cold-formed thin gauge purlins is complicated to calculate because of the following reasons:

1. The geometric properties of the channel section and Z-section purlins are complicated. To calculate

their effective sections, the main axis of the section needs to be moved, and the section becomes asymmetric.

2. The loading at the center of the top flange of the purlin causes a twist in the purlin due to the eccentricity of the load from the shear center. The emergent warping stress and warping properties are difficult to calculate.

3. The stability estimate should account for both the flexural-torsional and the distortional buckling modes. In addition, the local post-buckling of the plate elements in compression must be allowed in the structure design. This necessitates the additional consideration of the interaction between the local post-buckling and the flexural-torsional buckling.

4. In steel structures, roof sheeting connected with purlins provides lateral and torsional restraint for purlins. The sheeting significantly affects the purlin stability such that Eurocode 3[1] defines a new approach different from the conventional analysis. The details in the connection design between the sheeting and the purlin vary too much to fit with a set of simple, accurate formulas.

The conventional analysis of the flexural-torsional buckling mode and the distortional buckling mode assumes ideal supporting and bracing conditions for purlins. Under the assumed conditions, the critical elastic buckling can be evaluated with sufficient accuracy. But the method ignores the local post-buckling of the plate elements in compression. This problem was resolved by the effective width method proposed by von Karman[2]. In addition, realistic purlins are subject to geometric imperfections, as well as residual stresses from the cold-formed operation. The consequent reduction in purlin strength was captured by a modification to the von Karman formula[3]. Nevertheless, in practical steel structures, the top flange of the purlins connected with roof sheeting is restrained by a mode different from the ideal supporting and bracing conditions. The different mode significantly alters the behavior of purlins. Therefore, the buckling theories mentioned heretofore must be modified.

This paper compares three different design codes for the estimation of purlin stability: the China code Technical Code of Cold-Formed Thin-Walled Steel Structures GB 50018—2002.[4], the Eurocode 3, Design of Steel Structures, Cold Formed Thin Gauge Members and Sheeting, EC3-1-3, ENV 1993-1-3: 2006.[1] and the Australian /New Zealand Standard, Cold-formed Formed Steel Structures, AS/NZS 4600:1996.[5]. Based on this comparison, a better method for calculating the buckling modes of purlins in practical current engineering can be developed in the future.

BUCKLING MODE OF PURLINS IN BENDING

The finite strip method may analyzes efficiently the buckling of the cold-formed purlins in bending. According to the theoretic analysis, there are two typical buckling modes for the whole purlin: the flexural-torsional buckling mode and the distortional buckling mode. These two modes do not exist simultaneously. The flexural-torsional buckling mode allows local buckling to coexist in which an interaction buckling occurs. For a lip-stiffened channel section or Z-section purlin, the local buckling stress is highest with the shortest buckle half-wavelength, and the flexural-torsional buckling stress is lowest with the longest buckle half-wavelength[6]. This suggests that the flexural-torsional buckling occurs when the compression flange of purlin is not laterally restrained, and the distortional buckling maybe occurs otherwise. To avoid a complex analysis of the interaction buckling, an effective section can be used for design in the cases where local post-buckling of the plate elements in compression is applied.

The above discussion was restricted to elastic buckling theories. Non-elastic buckling theories are far too complex for accurate derivation. They are generally approximated by empirical formulas summarized from numerous tests of purlin stability.

BEHAVIOUR OF PURLINS IN PRACTICAL STEEL STRUCTURES

The loading at the center of the top flange of the purlin generally causes a twist in the purlin due to the eccentricity of the load from the shear center. This causes a warping stress that is difficult to calculate. If the sheeting is tightly fastened by screws to the top flange of the purlins, the twist of purlin may be prevented by the lateral restraint from the sheeting. In this case the purlin can only bend in the plane parallel to their web. The bending can be simply characterized by the section modulus along the axis perpendicular to the web. If full lateral restraint acts on the compression flange of the purlins, it is not necessary to calculate purlin stability. However, the full lateral restraint will act on the tension flange of the purlin when the sheeting connected with the top flange is subject to an uplift wind load. The distorted deformation of the purlin section is shown in Figure 1. The behavior of purlins under this condition is very different from that of purlins restrained by the ideal boundary conditions as assumed in the conventional theories for flexural-torsional and distortional buckling. The distortional buckling mode of the purlin is based on the flexural-torsional buckling of a simple compression flange model developed by Lau and Hancock[7] (Figure 2). This deformation and buckling mode explains the behavior of sheeted purlins observed in tests (Ref.[7] and Ref.[8]). Channel section and Z-section purlins with the same dimensions (h, b, a, t in Figure 1) have the same critical buckling stresses.

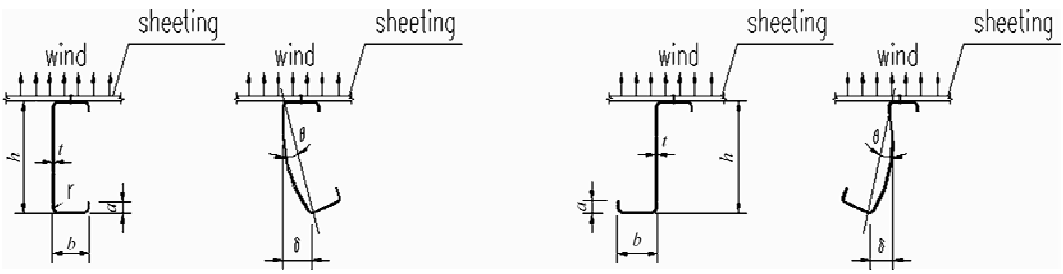

Figure 1 Distorted deformations of the purlins.

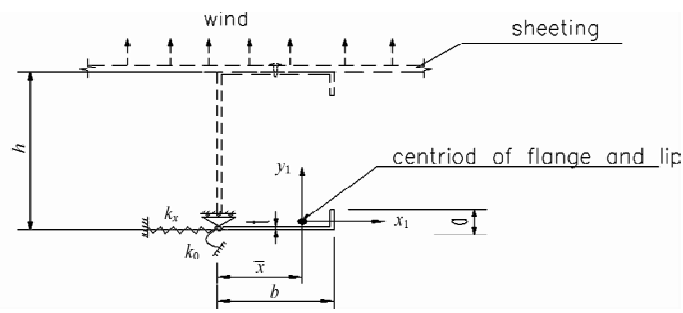

Figure 2 Compression flange elastically restrained along the flange-web junction.

In the above discussion about the tightly fastened sheeting, the sheeting diaphragm effect imposes strong lateral restraint to the purlins and the flexural stiffness of the sheeting imposes torsional restraint to the purlins. But the sheeting may be leaky caused by the heat related sheeting deformation. So panel clips

have replaced the screwed fastening in the past decade to conquer the disadvantages of screw holes in the roof sheeting. The sheeting connected with panel clips, e.g. standard seam roof panel, can move as temperature changes. Thus the sheeting diaphragm effect, e.g. the lateral restraint effect on the purlins, may disappear. Although the sheeting with panel clip can move along the direction perpendicular to the purlins, the sheeting still provides a weak lateral restraint to the purlins[9]. More importantly, the weak torsional restraint given by the panel clip can still affect the buckling behaviour of purlins[10].

Euro code 3 gives formulas for computing the buckling stresses of purlins with sheeting fastened tightly by screws[1]. From there the torsional restraint by the sheeting flexural stiffness can be evaluated. There are two typical models of roof panel clips as shown in Figure 3. Type A provides considerable torsional restraint to the purlins because the moveable piece is blocked in the slot and the panel clip is fixed by two screws. Type B, on the other hand, almost cannot restrain purlins from torsion.

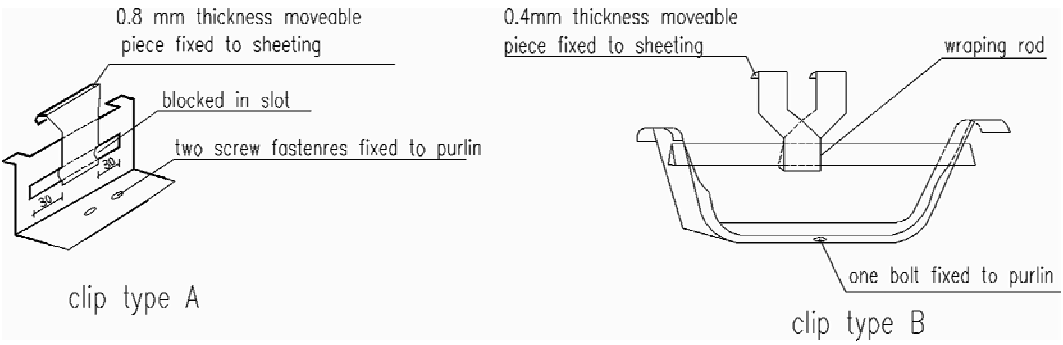

Figure 3 Two types of panel clip fixed at the purlins.

In order to study the effect of the torsional restraint of sheeting on the purlins, the buckling stresses of a 9-meter long channel purlin of section $250\times70\times20\times2.0$ were calculated for different numbers of anti-sag bars and different torsional restraint stiffness using the formulas in Euro code 3-1-3[1]. The buckling stress curves are presented in the dimensionless form, i.e. relative torsional restraint stiffness K/K_{full} (K_{full} stands for the full torsional restraint stiffness of sheeting with screw fastened tightly) versus dimensionless buckling stress σ_{cr}/f_y (f_y stands for yield stress), as shown in Figure 4, following our previous work[10, 11].

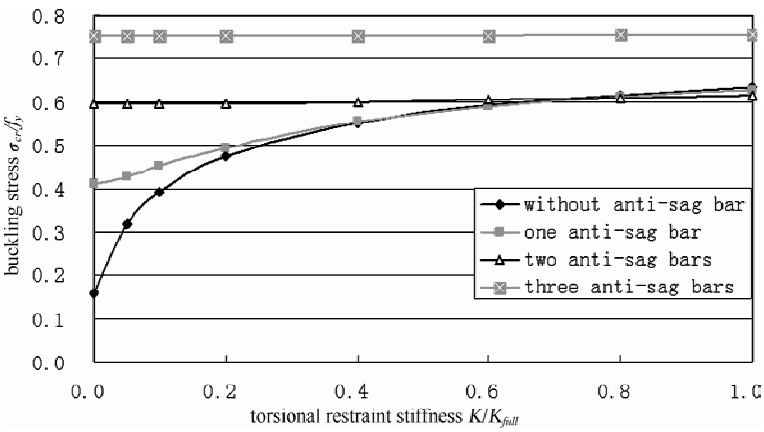

Figure 4 Dimensionless buckling stress curves of 9-meter long channel purlin.

The curves are presented in the dimensionless form. The torsional restraint stiffness is normalized by the full torsional restraint stiffness of sheeting with screw fastened tightly, i.e. K/K_{full}. The buckling stress is normalized by the yield stress, i.e. σ_{cr}/f_y. Four different cases are compared: without anti-sag bar (diamond), one row of anti-sag bar at the center of the purlin span (square), two rows of anti-sag bars at the third points (triangle), three rows of anti-sag bars at the center and the quarter points (square and cross). The calculation was carried out using Euro code 3-1-3 (Eq. (2)).

Figure 4 suggests the following points:

1. Without anti-sag bars a small increase in the torsional restraint stiffness of the sheeting leads to significant improvement of purlin stability when the restraint stiffness is small; such sharp dependence quickly attenuates as the restraint stiffness increases. Once the critical lateral restraint stiffness for purlin buckling is reached, further stiffening of the sheeting restraint makes almost no more difference.
2. If two and more anti-sag bars are arranged, the purlin buckling does not depend on the sheeting restraint. Conversely, once the sheeting restraint stiffness is enough the lateral restraint provided by a few anti-sag bars is dispensable.
3. Without the sheeting restraint (i.e. $K/K_{full}=0.0$) the buckling stress increases as the number of anti-sag bars increases.

COMPARING THE BUCKLING CALCULATIONS USING THREE DESIGN CODES

There are three widely used methods to calculate the stability of roof purlins:

1. In the China code Technical Code of Cold-Formed Thin-Walled Steel Structures GB 50018—2002, the stability calculation of the purlins is based on the flexural-torsional buckling. It does not capture the distortional buckling and the lateral restraint imposed by the sheeting connected with the purlins. Equation (A.2.1-1) of clause 5.3.3 in GB 50018[4] gives the buckling stress of the purlin as:

$$\sigma_c = \varphi_{bx} \cdot f_y = \frac{4\,320A \cdot h}{\lambda_y^2 \cdot W_x} \cdot \xi_1 \cdot \left(\sqrt{\eta^2+\zeta}+\eta\right) \cdot 235 \tag{1}$$

when $\varphi_{bx} > 0.7$, $\varphi'_{bx} = 1.091 - \dfrac{0.274}{\varphi_{bx}}$

2. In the Euro code Cold Formed Thin Gauge Members and Sheeting EC3-1-3.:2006, the stability calculation of the purlins conforms to the wind uplift tests of the purlins laterally restrained by the connected sheeting under practical engineering conditions. The rotational restraint imposed by the sheeting connected to the top flange of the purlin greatly improves the stability of the purlins (Figure 4). Equation (10.7) of clause 10.1.4.2 in EC3-1-3[1] gives the buckling stress of the purlin as:

$$\sigma_c = \frac{f_y}{W_x}\left(\frac{1}{\dfrac{1}{\chi \cdot \mathrm{W}_x} + \dfrac{\eta \cdot k \cdot C_b}{W_{fly}}}\right) \tag{2}$$

in which C_b is determined by the lateral bracing given by anti-sag bars.

3. In the Australian /New Zealand Standard Cold-formed Formed Steel Structures AS/NZS 4600, the stability calculation of purlins includes both the flexural-torsional buckling and the distorsional buckling. But it does not consider the effect of restraint imposed by the sheeting. In general, when a purlin is under more lateral restraint, e. g. connected with more anti-sag bars, the distorsional buckling dominates; otherwise, the flexural torsional buckling dominates. Equations 3.3.3.2(1) ~ 3.3.3.2(12) of clause

3.3.3.2 in AS /NZS 4600[5, 6] gives the flexural-torsional buckling stress of the purlin as:

$$\sigma_b = \frac{C_b \cdot \pi \cdot \sqrt{E \cdot I_y \cdot G \cdot J}}{l \cdot W_x} \cdot \sqrt{1 + \frac{\pi^2 \cdot E \cdot I_w}{G \cdot J \cdot l^2}} \tag{3}$$

when $\sqrt{f_y/\sigma_b} \leqslant 0.60$, $\sigma'_b = f_y$

$$0.6 < \sqrt{f_y/\sigma_b} < 1.336,\ \sigma'_b = 1.11 f_y \left[1 - \left(\frac{10 f_y}{36 \sigma_b}\right)\right]$$

$$\sqrt{f_y/\sigma_b} \geqslant 1.336 \quad \sigma'_b = \sigma_b$$

And Equation D2(1) of clause 3.3.3.3 in AS /NZS 4600[5, 6] gives the distorsional buckling stress of the purlin as:

$$\sigma_d = \frac{E}{2A}\left[(\alpha_1 + \alpha_2)^2 - \sqrt{(\alpha_1 + \alpha_2)^2 - 4\alpha_3}\right] \tag{4}$$

when $\sqrt{f_y/\sigma_d} \leqslant 0.674$, $\sigma'_d = f_y$

$$\sqrt{f_y/\sigma_d} > 0.674,\ \sigma'_d = \sqrt{\sigma_d \cdot f_y} \cdot (1 - 0.22\sqrt{\sigma_d/f_y})$$

The final buckling stress of the purlin is determined by the smaller of σ'_b and σ'_d, i.e.

$$\sigma_c = \min\{\sigma'_b, \sigma'_d\} \tag{5}$$

Using above the Eq. (1) ~ Eq. (5), previous channel section purlin under uplift wind loading was computed with the following coefficients:

$$h = 250 \text{ mm} \quad b = 70 \text{ mm} \quad a = 20 \text{ mm} \quad t = 2.0 \text{ mm}$$
$$r = 3.0 \text{ mm} \quad E = 206\,000 \text{ N/mm}^2 \quad f_y = 235 \text{ N/mm}^2$$

Anti-sag bars were arranged with four patterns: without anti-sag bar, one row of anti-sag bar at the center of the purlin span, two rows of anti-sag bars at the third points, three rows of anti-sag bars at the center and the quarter points. The corresponding buckling lengths are 9 000 mm, 4 500 mm, 3 000 mm, and 2 250 mm respectively. Using Eq. (2), the rotational restraint imposed on the purlin by the sheeting is evaluated in two cases: full torsional restraint stiffness and without torsional restraint stiffness. Geometry properties of purlin are shown in Tab. 1. And the computed buckling stresses from three design codes are shown in Figure 5.

TABLE 1 GEOMETRY PROPERTIES OF CHANEL SECTION PURLIN

area A (mm^2)	shear center e_o (mm)	I_x (mm^4)	W_x (mm^3)	I_y (mm^4)	i_y (mm)	J (mm^4)	I_w (mm^6)
830.3	45.2	7 510 400	60 083	504 320	24.6	1 107	6.123 1E+09

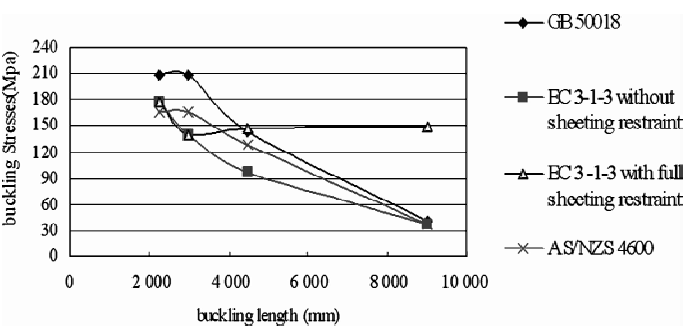

Figure 5 Comparing buckling stresses of 9 – meter purlin computed with different design codes

Four different cases are compared: China code (diamond), EC3-1-3 code without sheeting restraint, (square), EC3-1-3 code with full torsional restraint stiffness of sheeting by fastened tightly (triangle), AS/NZS4600 code (cross).

Figure 5 suggests the following points:

1. The three design codes give almost same buckling stress in the case without anti-sag bar, but different buckling stresses in the EC3-1-3 code with rotational restraint on the purlin by the sheeting. In this case the rotational restraint of sheeting significantly increases the buckling stress of the purlin.
2. With anti-sag bar, the buckling stress given by GB 50018 code is higher than that given by the other two design codes. But according to GB 50018 code, verifying stress needs to include warping stress so that GB 50018 code will give more conservative evaluation if without anti-sag bar or greater buckling length.
3. Result from EC3-1-3 code shows clearly that the rotational restraint of sheeting significantly increases the buckling stability if without anti-sag bars or greater buckling length.

CONCLUSIONS

The rotational restraint imposed on the cold-formed purlin by the connected sheeting can significantly improve the buckling behavior of the purlin. But conventional buckling analysis can not address the problem. Old type sheeting fixed to purlins by self-tapping screws can provide enough diaphragm effect to restrain purlins. But such effects are enormously weakened in the new sliding sheeting fixed by panel clips designed to prevent the permeation of water. However, the weak diaphragm effect of sheeting can still contribute notably to purlin stability. This finding awaits future experimental tests that measure the typical rotational restraint stiffness of the sheeting. Our study of the rotational restraint stiffness imposed on the purlins by the connected sheeting sheds important light on the design of the purlins.

REFERENCES

[1] Eurocode 3, Design of Steel Structures, "Cold Formed Thin Gauge Members and Sheeting", EC3-1-3, ENV 1993-1-3:2006.
[2] Von Karman, T., Sechler, E. E. and Donnell, L. H., "The Strength of Thin Plates in Compression", Transactions ASME, Vol. 54, MP 54-5,1932.
[3] Winter, G., "Strength of Thin Steel Compression Flanges", Transactions ASCE, Vol.112, Paper No,1947, pp 527-576.
[4] China code, "Technical Code of Cold-Formed Thin-Wall Steel Structures", GB 50018-2002.
[5] Australian /New Zealand Standard, "Cold-formed Formed Steel Structures", AS/NZS 4600:1996.
[6] G. J. Hancock, "Design of Cold-Formed Steel Structures", Australian Institute of Steel Construction 1998. PP. 39-42., pp.82.
[7] Hancock,G.J., Celeban, M. and Healy, C. L., "Behaviour of Purlins with Screw Fastened Sheeting under Wind Uplift and Downwards Loading", Australian Civil Engineering Transactions, The Institution of Engineers, Australian, Vol. CE 5, No. 3, August, 1993,pp.221-233.
[8] Hancock, G.J., Celeban, M., Healy, C. L. and Georbiou, P. N., "Testa of Purlins with Screw Fastened Sheeting under Wind Uplift", Proceedings, 10th International Specialty Conference on Cold-Formed Steel Structures, St. Louis, Missouri, U.S.A., 1990,pp.393-419.
[9] Chen Y. and Wang Y., "Application of Sheeting Diaphragm in Light-Weight Steel Structures", Building Structure, China Civil Engineering Society, Vol. 32, No. 2,2002,pp.29-33.
[10] Chen Y., "Comparison of Two Stabilized Calculation Modest of Cold-Formed Thin-Wall Steel Purlins", Steel Construction, China Iron and Steel Association, Vol.24, No.122, July, 2009,pp.62-65.
[11] Chen Y. and Wei C., "Explaining Problem of Steel Structure Design and Construction of Light-Weight Buildings with Gabled Frames", China Architecture & Building Press, 2009,pp.111-113.

Proceedings of Seventh International Conference on Advances in Steel Structures, 2012, Nanjing, China

PARAMETRIC ANALYSIS OF HYSTERETIC PERFORMANCE OF THE C-SECTION COLUMNS OF COLD-FORMED STEEL

* X. Peng[1], N.Q. Cheng[2], Y. Guo[1], L. Qiao[3]

1. Beijing Jiaotong University, Beijing 100044, China
2. Beijing Victory Star Archite ctural and Civil Engineering Design (0. LT1), Beijing 100025, China
3. Urban Construction Design & Research Institute, Beijing 100120, China
* Email: 09115282@bjtu.edu.cn

KEYWORDS

Cold-formed steel, C-section, buckling behavior, hysteretic performance, parametric analysis.

ABSTRACT

Recently, cold-formed steel structure are widely used in light steel house and will has a broad prospects, as its lightweight, high post-strength, convenient construction as well as green environmental protection and energy saving. Research home and abroad mainly focuses on the static performance of cold-formed steel, while research on hysteretic performance, which is the very base of wind-resistant and anti-seismic design of cold-formed steel structure, is deficient. Upon the base, the hysteretic performance of cold-formed steel and the key parameters influencing the hysteretic performance are analyzed by FEM, on the purpose of concluding the buckling mode and characteristics, obtaining the key parameters and supporting the consequent experimental research. The result indicates that the yield strength, width-thickness ratio and axial compressive ratio are playing important role. However, the initial defect and cold-formed effects give less influence.

INTRODUCTION

As the steel production and the technology keeps on increasing, as well as the advocation of green ideas, lightweight steel construction begins to develop fast. And the cold-formed steel is more and more widely used as a new and pro-environmental material. Compared to traditional steel, its most obvious advantage is the lightweight and thin-wall. At the same time, the advancing manufacturing process brings the material section variety, high strength, better durability as well as convenient construction, all of which give cold formed steel the great advantage and vast prospect on lightweight steel structure[1-3].

Research home and abroad are mainly focused on the static performance. He Baokang[4] experimentally studied the distortional buckling, which revealed the negative influence of the correlative role between local and distortion buckling and gave some suggestion on criterion modification. Shen Zuyan and Tang yang tested the short columns of cold-formed steel under axial load, in order to analyze the buckling mode

and compare to the results from the specification[5]. While in abroad, Lao and Hancock experienced on C-section struts and shelf columns, identifying that distortional buckling decided the bearing capacity on condition of certain shape and size[6]. Rogers and Schuster had done lots of work on specimens of C-section and Z-section and proved that there was some interaction between local buckling and distortion buckling[7]. Research on hysteretic performance of cold-formed steel was lack by contrast[8-9]. In addition, cold-formed steel had been widely used in lightweight building abroad, and the specimens of which thickness was less than 1 mm, were used as construction member. While, in china, the application just began, and there were few specimens thinner than 1 mm, most of which were used as secondary member.

Based on that, it is quite necessary to study the dynamic performance of cold-formed steel structure including wind resistance and seismic resistance. This paper goes into the hysteretic performance of cold-formed steel specimens, analyzes each parameter, obtains the key factors, and gives some advices on subsequent experimental research.

FINITE ELEMENT MODE AND BUCKLING MECHANISM

Finite Element Mode

As shown in Figure 1, The finite element mode uses Shell181, considers nonlinearity of material and geometry. Ideal elastoplastic model is chosen to be the materials mode. Two rigid boards (are not shown in Figure 1) are set in both ends of the components for uniform force and that is where the load and restrain are put. The bottom of the member is fixed, and Uz and Rotx on the top are restrained avoiding the influence of eccentricity and shear centre shift.

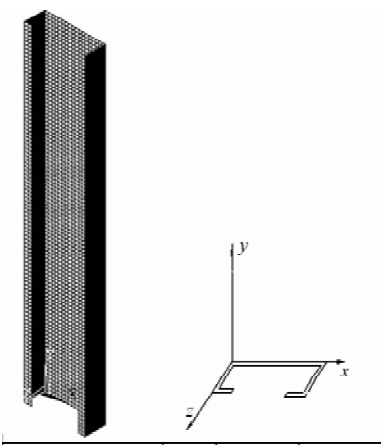

Top	*Uz*	Rotx	
Bottom	*Ux*	*Uy*	*Uz*

Figure 1 Finite element model

When analyzing the buckling mechanism, the paper use static horizontal load instead of cyclic load for the purpose of obtaining the consecutive process of buckling. And this simplification will cause small difference as follows: the later have less cumulative damage and local buckling occurs on the compressive

side. Anyhow, it will not change the mode and features of the buckling behavior with cold-formed steel.

Buckling Mechanism under Compressive and Bending Load

The buckling behavior and post-strength have been expounded in the buckling theory of sheet[3]. Simply speaking, the specimen's web occurs local buckling first under axial load. After that, web goes on carrying load by membrane effects as the flanges on sides give strong support until fractures (shown in Figure 2(a)).

While, the buckling behaviors of specimens under compressive and bending load are quite different for the ones under axial load. Figure 2(b) and (c) reveal the Mises stress and out-of-plane displacement that can stand for the local buckling. The low stress area is distributed in circle, which means the local buckling of the web caused by axial force. As the load process goes on, the bottom of the specimen bears the big moment, and the local buckling on the compressive side of web is exacerbated, while it on the tension side is decreased. And that is why the buckling half-wave moves to the compressive side. In addition, the direction of principal tensile stress changes as the nonuniform load, which makes the buckling half-wave slant and zonal. Interestingly, the buckling half-waves turn narrower in the bottom. That is mainly because this part of web bears bigger extrusion stress. The damaging process of components under compressive bending load can be also divided into two parts: pre-buckling and post-buckling. And the post-buckling strength comes from membrane effects dependent on the support of stiffen area beside. As the bending stress increases, local buckling on the compressive side develops fast, much faster than the one under axial load, and that is why the member fractures soon.

(a) Mises stress (Axial load) (b) Mises stress (c) Displacement of local buckling (Compressive bending load)

Figure 2 Buckling mode of specimens

PARAMETER ANALYSIS ON HYSTERETIC PERFORMANCE

Initial Geometrical Imperfection

According to the specification[10], the overall imperfection is supposed to correspond with sine function, and $L/750$ is chosen to be the amplitude. As to local imperfection, there is two way to consider it. One is supposing the curve plate accords with double trigonometric series:

$$w = \sum_{m=1}^{\infty}\sum_{n=1}^{\infty} A_{mn} \sin\frac{m\pi x}{a}\sin\frac{n\pi y}{b} \tag{1}$$

We called this one random imperfection (RI). The other way is choosing the first stage buckling mode to be the critical imperfection, which is called accordant imperfection (AI). The amplitude of local buckling can be defined to be WEB/150[11]. The specimens in Table.1 are chosen for analysis.

TABLE 1 DETAILS OF SPECIMENS WITH VARIOUS INITIAL DEFECT

Specimen	L(mm)	N/N_y	Defect	Local	Overall
C120×40×20×1	1 500	0.1	None	0	0
			AI	$W/150$	$L/750$
			RI	$W/150$	$L/750$
			RI	$W/200$	$L/750$
			RI	$W/150$	$L/1\,000$

As shown in Figure 3. It indicates the imperfection can weaken the member to an extent. However, the form and peak value of imperfection play little influence.

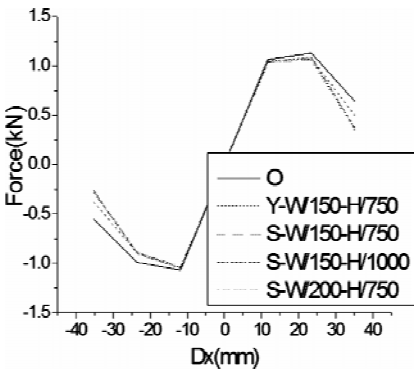

Figure 3 Results of specimens with various initial defect

Cold Bending Effect and Yield Strength

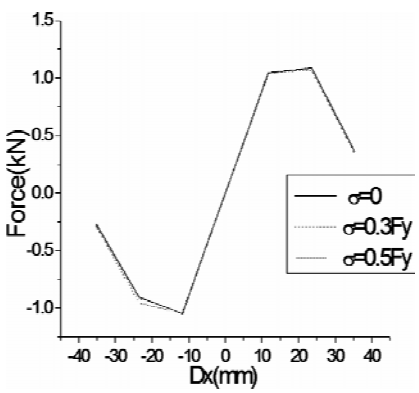

Figure 4 Results of specimens with various residual stress

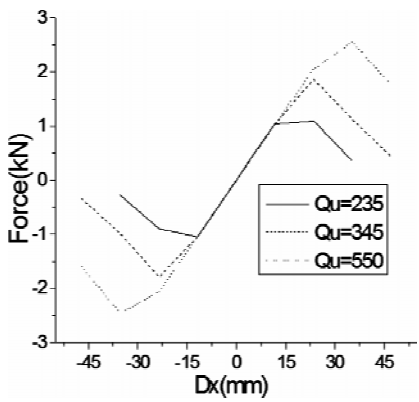

Figure 5 Results of specimens with various yield strength

Cold bending effect is formed in the process of fabrication. As to specimens under compressive and

bending load, the effects play little influence on the hysteretic performance according to the skeleton curve (shown in Figure 4).

As shown in Figure 5, the yield strength of steel influences the hysteretic performance, to a certain extent. And it is worth mentioned that improving yield strength is one of the main developing direction, as it can enhance the post-buckling strength.

High-thickness Ratio of Web

Figure 6 shows components with various high-thickness ratio of web. The hysteretic performance is not good enough. The strength decrease badly after the ultimate strength is approached.

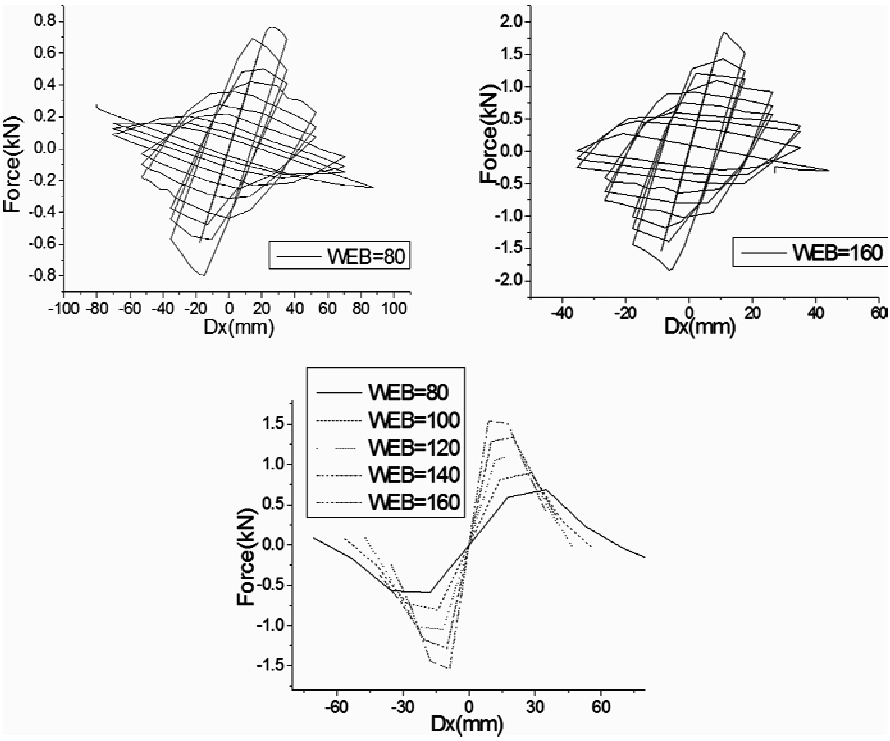

Figure 6 Results of specimens with various width-thickness ratio of web

TABLE 2 SPECIMENS WITH VARIOUS WEB

Section	L(mm)	Specimens	N/N_y	F_u(kN)	μ
C120×40×20×1	1 500	CW80	0.1	0.76	1.82
		CW100	0.1	1.03	1.78
		CW120	0.1	1.28	1.76
		CW140	0.1	1.56	1.76
		CW160	0.1	1.83	1.75

According to the analysis, the strength increases, while the ductility weakened with the high-thickness ratio of the web increases and it can also be easily seen in the skeleton curves. So, bigger high-thickness ratio of the web will make weaker hysteretic performance.

High-thickness ratio controls the half-waves of local buckling and the critical capacity. As shown in Figure 7(a), smaller high-thickness ratio gives stronger web and higher critical strength of local buckling, even higher than the critical capacity of bending-torsional buckling of the flange. Specimens of this kind are more likely occurs bending-torsional buckling, and the local buckling is not obvious. With the web turns bigger, the local buckling plays a more important role, and it is the reason that weakens the hysteretic performance. It is worth mentioned that the increase of the strength is due to the improvement of the resistance torque.

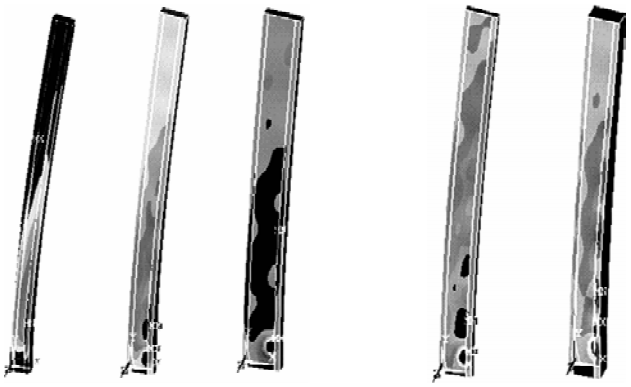

(a) various high-thickness of web (b) various width-thickness of flange

Figure 7 Buckling modes of various specimens

Width-thickness Ratio of Flange

The bending-torsional buckling and local buckling mode of the flange influence on the hysteretic performance. When the members are loaded with axial and horizontal load, wider flange can hardly occur bending-torsional buckling but easily occur local buckling. So it is difficult to judge the influence of the width-thickness ratio of the flange. The specimens in Table 3 are chosen to answer the question.

TABLE 3 SPECIMENS WITH VARIOUS FLANGE

Section	L(mm)	Specimens	N/N_y	F_u(kN)	μ
C120×40×20×1	1 500	CF40	0.1	1.28	1.70
		CF60	0.1	1.53	1.58
		CF80	0.1	1.51	1.44

According to the hysteretic skeleton curve with various width-thickness ratio shown in Figure 8, it can be easily known that the width-thickness ratio increases the capacity and the stiffness in a way. However when the ratio is bigger than 60, it plays little influence on the improving the bearing capacity, or even decreases it. The member CF80 occurs local buckling mode, which decreases the strength obviously. Generally speaking, the width-thickness ratio influences the hysteretic performance very little and the envelope area of the curve changes little. And the skeleton curve shows the same rule. The results in Table 3 show us the degradation of the ductility.

Figure 7(b) also shows the buckling behavior. Wider flange is less likely to torsion, but easier to occur local buckling. So the width-thickness ratio had better be less than 60.

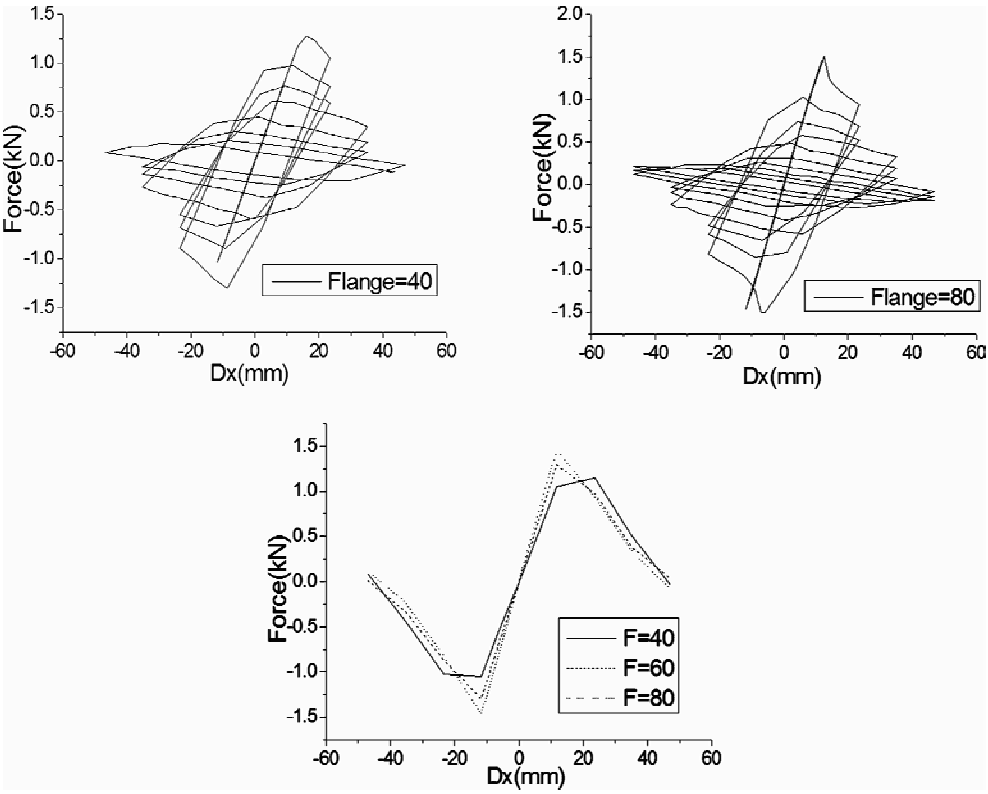

Figure 8 Results of specimens with various width-thickness ratio of flange

Width-thickness Ratio of Lip

The role of lip is to constrain the deformation of flange, especially that of flange's torsion, which actually is good for the stability of the member. Components in Table 4 are chosen to analyze.

Hysteretic and skeleton curve of various components are shown in Figure 9. Component with no lip has weak hysteretic performance. However, in the other hand, too wide lip will have little positive role on improving the hysteretic performance. According to the skeleton curve, the lip's width had better be less than 20.

The stress and deformation of the specimens in Table 4 are shown in Figure 10(a), which further tells the importance of lip. The deformation of local buckling of flange with no lip develops freely.

TABLE 4 COMPONENTS LIST OF VARIOUS LIP

Section	L(mm)	Specimens	N/N_y	F_u(kN)	μ
C120×40×20×1	1 500	CL0	0.1	0.63	1.42
		CL10	0.1	1.05	1.50
C120×40×20×1	1 500	CL20	0.1	1.28	1.70
		CL30	0.1	1.35	1.81

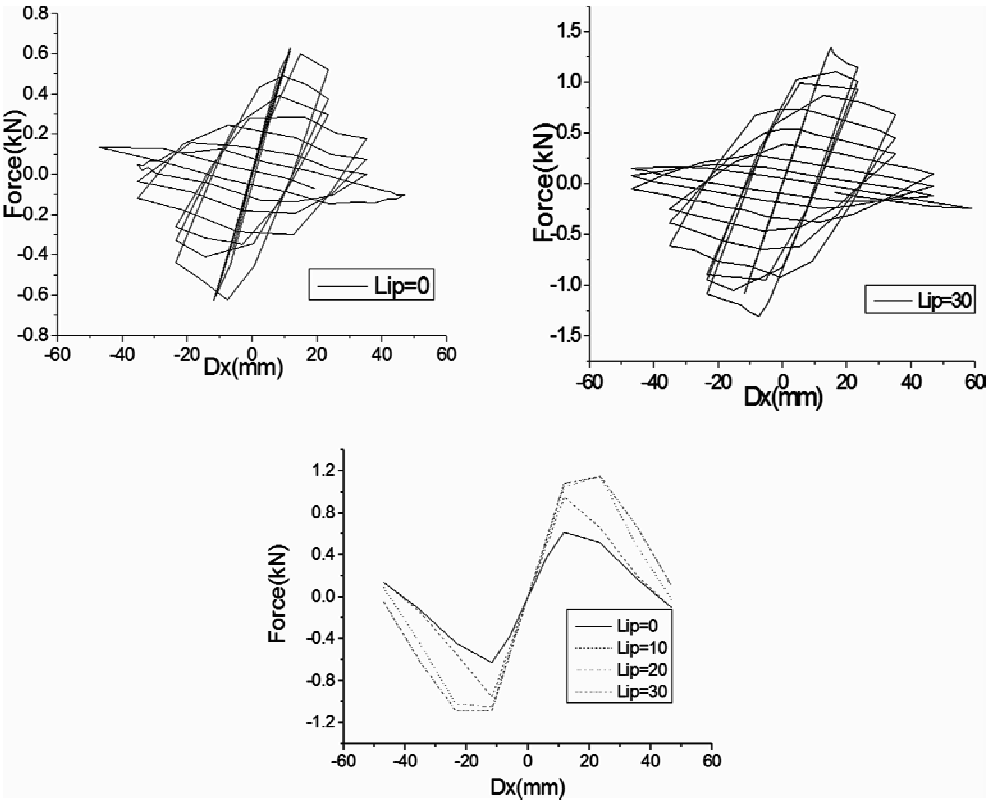

Figure 9 Results of specimens with various width-thickness ratio of lip

Axial Compression Ratio

The negative influence of axial compression ratio on thin-walled steel is quite obvious. As known to us all, the $P-\Delta$ effect will enhance the stress of the moment and the axial load will cause larger deformation of local buckling. Specimens in Table 5 are chosen.

Figure 11 shows the hysteretic curve and skeleton curve with different axial compression ratio. The hysteretic curve goes like a full spindle with no axial load. While the ratio is 0.1, compared to the former, the hysteretic performance decreases a lot. When the ratio reached 0.15, the envelop area of the curve is quite small and the hysteretic performance is weak. The data in Table 5 shows the ductility decreases 57.5% while the axial compression ratio changes from 0 to 0.1. And with the ratio goes on decreasing, the ductility is weaken not so badly. It can be easily seen according to the skeleton curve, the axial compression ratio weakens the strength stiffness and the hysteretic performance.

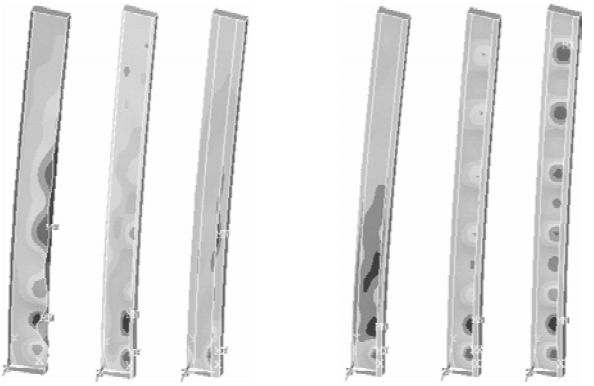

(a) various lips (b) various axial compression ratio

Figure 10 Buckling modes of various specimens

TABLE 5 SPECIMENS WITH VARIOUS AXIAL COMPRESSIVE RATIO

Section	L(mm)	Specimens	N/N_y	F_u(kN)	μ
C120×40×20×2	1 500	CZ0.5	0	3.30	4.45
		CZ1	0.1	2.90	2.56
		CZ1.5	0.15	2.69	2.20
		CT2	0.2	2.39	2.05
		CT2.5	0.25	2.11	1.92
		CT3	0.3	1.91	1.75

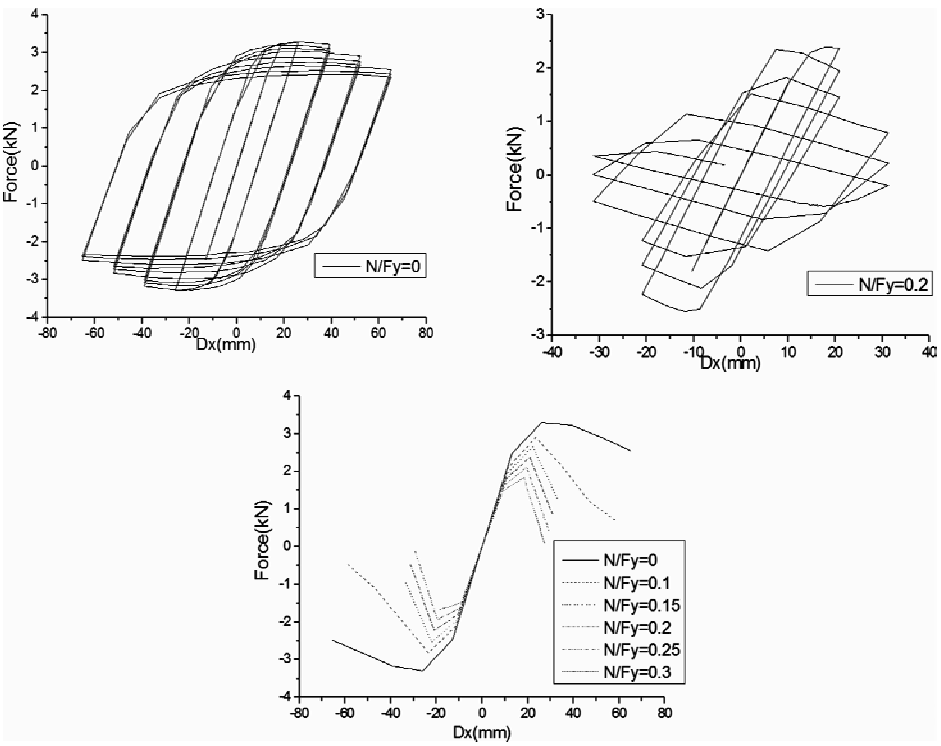

Figure 11 Results of specimens with various axial compressive ratio

In addition, from the local buckling deformation shown in Figure 10(b), it can be easily known that the axial compression ratio changes the local buckling half-wave.

CONLUSIONS

The paper research on the buckling behavior and hysteretic performance of C-section columns under compression and moment, and conclusions are made as follows:

1. The yield point of material plays influence on the hysteretic performance, while the initial defect and cold bending effect plays little influence.
2. The width-thickness ratio of the plates of the cold-formed steel members influences the hysteretic performance. Bigger width-thickness ratio gives better anti-twist ability, but easier to occur local buckling. In all, local buckling is the important reason weakening the hysteretic performance and the ductility.
3. Axial compression ratio increases the deformation of local buckling, and brings additional moment, both of which weakens the hysteretic performance a lot.

ACKNOWLEDGEMENT

This study is sponsored by the National Nature Science Foundation of China No. 50938008 and No. 51078026.

REFRENCE

[1] Yu, W. W., "Design of cold-formed steel structure (3rd)", Dong Jun, Xia Bingqing. Beijing: China Waterpower Press, 2002.12.
[2] Chen, S. F., "Steel structure (2nd)", Beijing, China Building Industry Press, 1993.
[3] Chen, J., "Stability theory and design of steel structure", Science Press, 1993.
[4] He, B. K., Jiang, L. and Yao, X. Y., "Experimental research on distortion buckling of C-section columns of high strength cold-formed steel under axial load", Journal of Building Structures, 2006.
[5] Tang, Y., "Test on cold-formed welded short columns under axial load", Journal of Structural Engineer, 1998, pp. 7-29.
[6] Lau, S. C. W. and Hancock, G. J., "Inelastic buckling of channel columns in the Distortional mode", Thin-walled structures, 1990, pp. 59-84.
[7] C. A. Rogers and R. M. Schuster, "Flange/Web distortional buckling of cold-formed Steel sections in bending", Thin-walled structures, 1997, pp. 13-29.
[8] Lu, X., "Research on bending hysteretic performance on C-section columns of cold-formed steel", Master thesis of Nanjing University of Technology, 2006.
[9] Wang, S. Q., "Analysis on tension-compression hysteretic performance on C-section columns of cold-formed steel", Master thesis of Nanjing University of Technology, 2005.
[10] GB 50018—2002. "Specification of cold-formed steel", Beijing, China Plan Press, 2002.
[11] Su M. Z. and Gu, Q., "Research on bending hysteretic performance and limit width-thickness ratio of boxed section columns", Journal of Building Structures, 2000, Vol. 21(5), pp. 41-47.
[12] Peng, X., "Research on hysteretic performance on C-section columns of cold-formed steel", Master thesis of Beijng Jiaotong University, 2007.

Proceedings of Seventh International Conference on Advances in Steel Structures, 2012, Nanjing, China

FRP STRENGTHENING OF LEAN DUPLEX STAINLESS STEEL HOLLOW SECTION SUBJECTED TO END BEARING LOAD

S. M. Z. Islam and * B. Young

Department of Civil Engineering, The University of Hong Kong, Pokfulam Road, Hong Kong, China
* Email: young@hku.hk

KEYWORDS

Adhesives, experimental investigation, fibre-reinforced polymer, lean duplex stainless steel, rectangular hollow section, strengthening, web crippling.

ABSTRACT

A test program on lean duplex stainless steel hollow section subjected to end bearing load is presented. The test specimens were strengthened with different fibre-reinforced polymer. The web crippling tests were conducted under End-Two-Flange loading condition. The investigation was focused on the effects of surface treatment, different adhesives and fibre-reinforced polymers for the strengthening of lean duplex stainless steel hollow sections against web crippling in a localised region of the members. The lean duplex stainless steel type EN 1.4162 was used in the investigation. Two different surface treatments, three different adhesives and six different fibre-reinforced polymers were investigated. The tests were performed on rectangular hollow section ($150 \times 50 \times 2.5$) having web slenderness ratio of 57.3. Three different failure modes were observed in the tests of the strengthened specimens, namely the adhesion, interlaminar failure of FRP plate and combination of adhesion and interlaminar failure of FRP plate.

INTRODUCTION

Cold-formed stainless steel hollow sections have been increasingly used in architectural and structural application due to its attractive features in terms of durability, superior corrosion resistance, easy maintenance, ease construction, aesthetic appearance and recyclability of the material. Lean duplex stainless steel is a relatively new grade of material, which contains approximately 1.6% nickel. The lean duplex type EN 1.416 2 material is much cheaper than the duplex type EN 1.446 2 containing approximately 5.7% nickel. The material price of lean duplex (EN 1.416 2) is approximately half of the duplex (EN 1.446 2) material. Despite the low nickel content, lean duplex stainless steel display a good combination of strength, corrosion resistance and fatigue resistance together with adequate weldability[1]. The webs of cold-formed stainless steel members may cripple due to concentrated bearing load in the absence of stiffeners[2]. However, the web crippling strength can be enhanced by fibre-reinforced polymer (FRP) strengthening in the web of the sections. Zhou and Young[2-4] conducted a series of tests on cold-formed stainless steel hollow sections subjected to web crippling. These test specimens were not

strengthened by FRP.

The conventional method of repairing or strengthening steel structures is to cut out and replace plating or to attach external steel plates[5]. However, such strengthening has some drawbacks due to bulky, heavy, difficult to fix and prone to corrosion and fatigue of these steel plates. Fibre reinforced-polymer (FRP) is an advanced material which is increasingly being used for strengthening and repair of existing metal structures. Therefore, externally bonded FRP strengthening can be considered as an alternately solution for the strengthening of stainless steel structural members in the localise region subjected to load concentration. Previous research on strengthening of metal structures is mainly focused on carbon steel members as summarized by Zhao and Zhang[5]. Experimental investigation on web crippling strengthening of rectangular carbon steel tubes and light steel beams have been conducted by Zhao et al.[6], Fernando et al.[7], and Zhao and Al-Mahaidi[8]. It should be noted that the stress-strain behaviour of carbon steel and stainless steel is quite different. Up-to-date, little research on carbon fibre-reinforced-polymer (CFRP) strengthening of lean duplex stainless steel hollow sections has been conducted, in particular, investigation of web crippling. Different failure modes for CFRP strengthened metallic structures have been reported[5-11]. Overall, little research on FRP strengthening of lean duplex stainless steel hollow sections subjected to web crippling. Hence, investigation on strengthening of lean duplex stainless steel hollow sections to localise region subjected to concentrated load is needed.

The purpose of this paper is to investigate the effects of surface treatment, different adhesives and different FRPs on the strengthening of lean duplex stainless steel hollow sections against web crippling. The effects of different surface treatments and adhesives on FRP strengthened lean duplex stainless steel hollow sections against web crippling failure were investigated. The effects of different FRPs on the strengthening of lean duplex stainless steel hollow sections subjected to End-Two-Flange loading condition was also investigated.

MATERIAL PROPERTIES

Lean Duplex Stainless Steel Tube

Tensile coupon test was conducted to determine the material properties of the lean duplex stainless steel hollow section specimen. The flat tensile coupon was taken from the centre of the face at 90° angle from the weld of the lean duplex stainless steel specimen in the longitudinal direction. The tensile coupon was prepared and tested according to the American Society for Testing and Materials Standard[12] and the Australian Standard AS 1 391[13] for the tensile testing of metals using 12.5 mm wide coupon of gauge length 50 mm. The coupon was tested in a displacement controlled testing machine. Two strain gauges and a calibrated extensometer of 50 mm gauge length were used to measure the longitudinal strain. A data acquisition system was used to record the load and strain at regular intervals during the tests. The static load was obtained by pausing the applied straining for 1.5 minutes near the 0.2% tensile proof stress and the ultimate tensile strength. This allowed the stress relaxation associated with plastic straining to take place. The material properties of the lean duplex stainless steel section had the measured static 0.2% tensile proof stress ($\sigma_{0.2}$) of 620 MPa, static tensile ultimate strength (σ_u) of 735MPa, initial Young's modulus (E_o) of 202.8 GPa, and tensile strain at fracture of 38.7% based on a gauge length of 50mm coupon test.

FRPs and Adhesives

In this study, six different types of FRP were used, and the FRPs are follows: (a) Sika Wrap-300C/60 carbon fibre, (b) Sika Wrap-430G/25 glass fibre, (c) Tyfo UC laminate, (d) Sika CarboDur S1214, (e) Sika CarboDur M614, and (f) Sika CarboDur H514. These FRPs are symbolized as 'a' to 'f' in Table1. The specified material properties of each FRP provided in the specifications are also shown in Table 1.

TABLE 1 MATERIAL PROPERTIES OF FRP GIVEN IN SPECIFICATIONS

Types of FRP	Symbol	t(MPa)	σ_u (MPa)	E_0(GPa)	ε_f (%)
Sika Wrap-300C/60 (CFRP)	a	0.166	3 900	230	1.50
Sika Wrap 430G/25 (GFRP)	b	0.172	2 300	76	2.80
Tyfo UC laminate (Laminate Plate)	c	1.400	2 790	155	1.80
Sika CarboDur S1214 (Laminate Plate)	d	1.400	3 100	165	1.70
Sika CarboDur M614 (Laminate Plate)	e	1.400	3 200	210	1.35
Sika CarboDur H514 (Laminate Plate)	f	1.400	1 500	300	0.45

Three different types of adhesive were used. The three types of adhesive are Tyfo TC, Araldite 2015 and Araldite 420, which are symbolized as 'C', 'E' to 'F' respectively, as shown in Table 2. Tensile coupon tests were conducted to obtain the material properties of these three types of adhesive[14]. The material properties of the adhesives are shown in Table 2.

TABLE 2 MEASURED MATERIAL PROPERTIES OF ADHESIVE OBTAINED FROM TENSILE COUPON TESTS[14]

Types of adhesive	Symbol	σ_u (MPa)	E_0(GPa)	ε_f (%)
Tyfo TC	C	19.6	2.3	1.3
Araldite 2015	E	19.7	1.8	3.3
Araldite 420	F	24.3	1.6	3.2

TEST SPECIMENS AND LABELLING

A series of web crippling tests was conducted on FRP strengthened lean duplex stainless steel hollow section subjected to web crippling. The lean duplex stainless steel type EN 1.4162 test specimen was used. Firstly, two different surface treatments using electric sander (S) and electric grinder (G) were used in order to find out the effective surface treatment for FRP strengthened lean duplex stainless steel section under the End-Two-Flange (ETF) loading condition. Three different adhesives of Tyfo TC, Araldite 2015 and Araldite 420 with high modulus CFRP Sika CarboDur H514 laminate plate were used to investigate the effective surface treatment. Secondly, six different FRPs were investigated to find out the best performance of FRP for lean duplex cold-formed stainless steel hollow section using a suitable surface treatment. The grinding surface treatment and adhesive Araldite 420 were used to find the best FRP for strengthening of lean duplex stainless steel section. The measured dimensions of the test specimens subjected to End-Two-Flange (ETF) loading are shown in Tables 3, 4 and 5 using the nomenclature defined in Figure 1(a). The specimen lengths $L = N + 1.5d$ for ETF loading condition was used, where N is the bearing length 50 mm and d is the overall web depth. The specimen lengths were determined according to the ASCE Specification[15]. In this study, the length of strengthening is identical to the length of the bearing (N) which is 50 mm. The height of the CFRP plates is equal to the flat portion of the web of the specimen as shown in Figure 1(b).

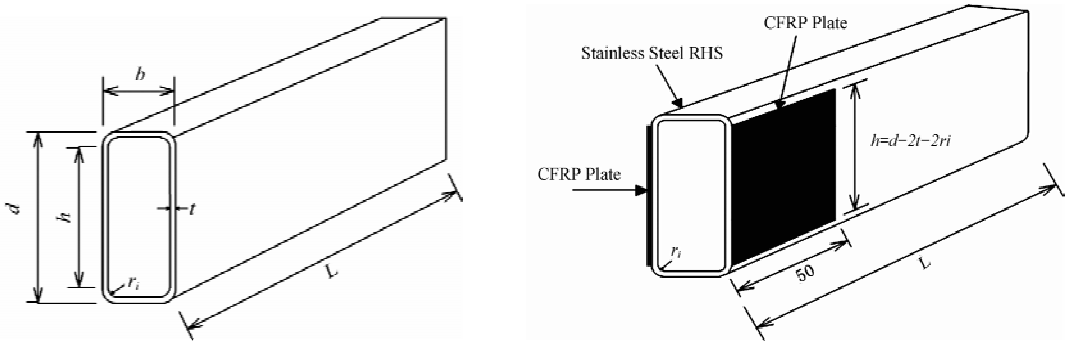

(a) Lean duplex stainless steel RHS section (b) FRP plate strengthened lean duplex stainless steel RHS section

Figure 1 Definition of symbols and FRP strengthened lean duplex stainless steel hollow section

The specimens were labelled such that the material types, nominal dimensions of the specimen, loading condition, type and number of FRP layer, type of adhesive and surface treatment can be identified, which is shown in Tables3－5. For example, the label "D150 × 50 × 2.5-ETF-f1-F-G-R" defines the following specimen: The first letter indicates the material type of the specimen, where "D" refers to lean duplex stainless steel. The following symbols are the nominal dimensions ($d \times b \times t$) of the specimen in mm, where 150×50×2.5 means d = 150 mm, b = 50 mm and t = 2.5 mm. The following three letters indicate the loading condition of End-Two-Flange (ETF). The following two letters indicate the type and number of fibre-reinforced polymer (FRP) layer, where "f1" means Sika CarboDur H514 of one layer (refer to Table 1), but the reference test without FRP is represented as "0". The following letter indicates the type of adhesive, where "F" refers to Araldite 420 as shown in Table 2. The following letter indicates surface treatment, where "G" refers to grinding surface treatment. If a test was repeated, then "R" indicates the repeat test. If a test was repeated for the second time, then "R2" indicates the second repeated test.

TABLE 3 MEASURED DIMENSIONS AND TEST RESULTS OF DIFFERENT ADHESIVE EFFECT ON GRINDING SURFACE TREATMENT OF SPECIMENS SUBJECTED TO END-TWO-FLANGE LOADING

Specimen	d (mm)	b (mm)	t (mm)	r_i (mm)	L (mm)	h/t	P_u (kN)	P_u/P_{u0}	Failure mode
D150×50×2.5-ETF-0	149.7	49.8	2.487	2.50	274.8	56.2	19.9	1.00	W
D150×50×2.5-ETF-f1-C-G	150.0	49.7	2.494	2.50	276.3	56.1	20.1	1.01	A
D150×50×2.5-ETF-f1-E-G	149.9	49.5	2.506	2.50	275.0	55.8	19.9	1.00	A
D150×50×2.5-ETF-f1-F-G	149.9	49.7	2.476	2.50	274.5	56.5	22.3	1.12	I
D150×50×2.5-ETF-f1-F-G-R	150.0	49.9	2.501	2.50	275.1	56.0	22.1	1.11	I

Note: A = adhesion failure; I = Interlaminar FRP failure; W = Web crippling.

TABLE 4 MEASURED DIMENSIONS AND TEST RESULTS OF DIFFERENT ADHESIVE EFFECT ON SANDING SURFACE TREATMENT OF SPECIMENS SUBJECTED TO END-TWO-FLANGE LOADING

Specimen	d (mm)	b (mm)	t (mm)	r_i (mm)	L (mm)	h/t	P_u (kN)	P_u/P_{u0}	Failure mode
D150×50×2.5-ETF-0	149.7	49.8	2.487	2.50	274.8	56.2	19.9	1.00	W
D150×50×2.5-ETF-f1-C-S	150.0	49.7	2.484	2.50	274.7	56.4	19.8	1.00	A
D150×50×2.5-ETF-f1-E-S	150.0	49.9	2.498	2.50	275.5	56.0	20.7	1.04	A
D150×50×2.5-ETF-f1-F-S	149.9	49.9	2.554	2.50	275.3	54.7	21.2	1.06	A

Note: A = adhesion failure; W = Web crippling

TABLE 5 MEASURED DIMENSIONS AND TEST RESULTS OF DIFFERENT FRP EFFECT ON GRINDING SURFACE TREATMENT OF SPECIMENS SUBJECTED TO END-TWO-FLANGE LOADING

Specimen	d (mm)	b (mm)	t (mm)	r_i (mm)	L (mm)	h/t	P_u (kN)	P_u/P_{u0}	Failure mode
D150×50×2.5-ETF-0	149.7	49.8	2.487	2.50	274.8	56.2	19.9	1.00	W
D150×50×2.5-ETF-a3-F-G	149.7	49.8	2.489	2.25	275.7	56.3	22.9	1.15	W
D150×50×2.5-ETF-b3-F-G	150.1	49.6	2.467	2.25	274.9	57.0	21.3	1.07	W
D150×50×2.5-ETF-c1-F-G	149.8	49.8	2.477	2.25	274.9	56.7	21.5	1.08	A+I
D150×50×2.5-ETF-d1-F-G	150.3	49.6	2.467	2.25	275.4	57.1	23.2	1.17	I
D150×50×2.5-ETF-d1-F-G-R	149.9	49.7	2.471	2.25	276.3	56.8	24.2	1.22	I
D150×50×2.5-ETF-e1-F-G	150.0	49.5	2.470	2.25	275.1	56.9	21.8	1.10	I
D150×50×2.5-ETF-f1-F-G-R	149.8	49.7	2.481	2.50	275.3	56.4	22.3	1.12	I
D150×50×2.5-ETF-f1-F-G-R2	150.0	49.6	2.454	2.25	275.7	57.3	22.5	1.13	I

Note: A = adhesion failure; I = Interlaminar FRP failure; A + I = combination of adhesion and interlaminar failure of FRP plate; W = Web crippling

SPECIMEN PREPARATION

The two surface treatment methods of electric sander (S) and electric grinder (G) were considered in this study to find out a more suitable surface treatment method for FRP strengthened lean duplex stainless steel sections. Generally, grinding, sanding or sand blasting surface treatments are used for FRP strengthening of metal structures[6-9, 16-18]. A BOSCH (PSS-23) sander or an electric grinder with 11 000 rpm 710 w was used for treatment of each surface of lean duplex stainless steel section. The silicon carbide (80Cw-medium grit) water proof electro coated abrasive/sand paper comprising an average particle diameter of 192 μm was used in the electric sander. The adhesive thickness for specimens strengthened with FRP plate was around 1.0 mm, whereas the thickness of adhesive for specimens strengthened with FRP sheet was around 0.25 mm. The FRP sheets were wrapped outside the lean duplex stainless steel hollow specimens, while CFRP plates were bonded to each web for a width of 50 mm. The test specimens were tested after 7 days of curing at room temperature.

WEB CRIPPLING TESTS

The web crippling tests were conducted under End-Two-Flange (ETF) loading condition specified in the ASCE Specification[15]. In the first phase of investigation, the specimens were tested to examine the surface treatment using electric sander and grinder as well as examine the adhesive on FRP strengthening. The test specimens are shown in Tables 3 and 4. In the second phase of investigation, the specimens were strengthened by different FRPs. The test specimens are shown in Table 5. A servo-controlled hydraulic testing machine was used to apply a concentrated compressive force to the test specimen. Displacement control was used to drive the hydraulic actuator at a constant speed of 0.3 mm/min. The test setup of ETF loading condition is shown in Figure 2.

TEST RESULTS AND DISCUSSIONS

The failure modes of lean duplex section D150×50×2.5 strengthened with FRP are shown in Tables 3-5. The failure mode of the specimen using grinding treatment is shown in Figure 3. It is shown that adhesion

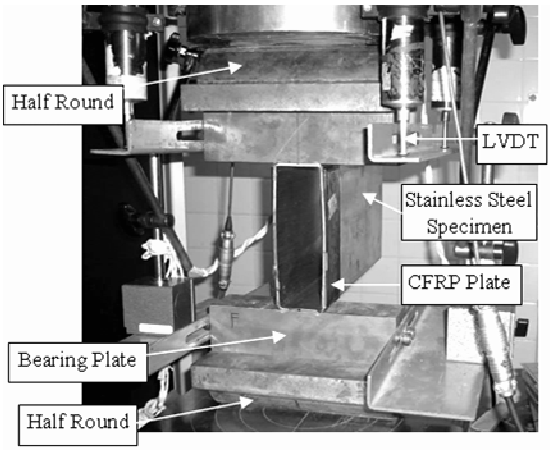

Figure 2 Test setup of End-Two-Flange loading condition

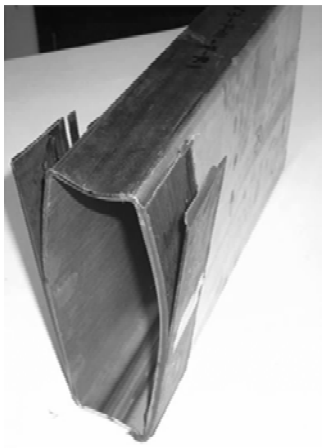

Figure 3 Interlaminar FRP failure of lean duplex stainless steel specimen

failure and interlaminar FRP failure were found for specimens using grinding surface treatment as shown in Table 3. However, only adhesion failure was found for specimens using sanding surface treatment as shown in Table 4. The failure modes for specimens strengthened with different FRP using grinding surface treatment are shown in Table 5 and Figure 4. The adhesive Araldite 420 was used in these specimens. The specimens strengthened with FRP sheets of Sika Wrap-300C/60 and Sika Wrap 430G/25 were failed by web crippling. Interlaminar FRP failure was found for specimens strengthened with CFRP plates, except for specimen D150×50×2.5-ETF-c1-F-G combination of adhesion and interlaminar FRP failure was also found, as shown in Table 5. The experimental ultimate web crippling loads per web with FRP (P_u) and without FRP (P_{u0}) are presented in Tables 3, 4 and 5. The specimen without strengthening of FRP was tested as reference test and this specimen is labelled using a suffix of "−0" as shown in Tables 3, 4 and 5 as well as labelled as "F0" in Figures 5-6. In the first stage of the tests, two different surface treatments using electric sander (S) and electric grinder (G) were investigated on section D150×50×2.5 to find a suitable surface treatment and adhesive for the FRP strengthened lean duplex stainless steel sections. Three different adhesives of Tyfo TC (C), Araldite 2015 (E) and Araldite 420 (F) as well as high modulus CFRP Sika CarboDur H514 laminate plate (f) were considered in the

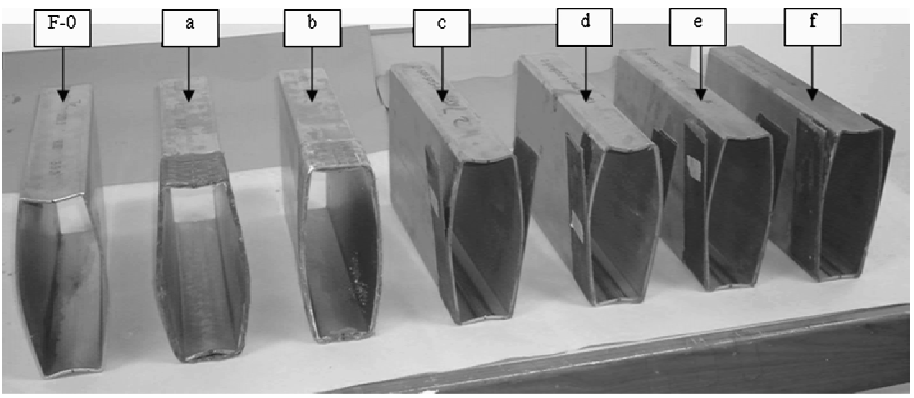

Figure 4 Failure modes of lean duplex stainless steel section D150×50×2.5 using grinding surface treatment and different FRPs

investigation. It is shown that the grinding surface treatment and adhesive Araldite 420 provided better performance ($P_u/P_{u0}=1.12$) compared to other lean duplex stainless steel sections in terms of the peak load enhancement, as shown in Tables 3-4 and Figure 5. In the second stage of the tests, grinding surface treatment was used. Six different FRPs were investigated using adhesive Araldite 420 on the section D150×50×2.5. It is shown CFRP Sika CarboDur S1214 with high strength, high strain, and small modulus delivered the best performance ($P_u/P_{u0}=1.22$) for the tested lean duplex stainless steel hollow sections as shown in Table 5 and Figure 6.

It is shown that grinding surface treatment, the adhesive Araldite 420 and the high strength and strain with lower modulus CFRP CarboDur S1214 laminate plate provided the best performance subjected to web crippling in this study. In this study, the web crippling strengths of CFRP strengthened lean duplex stainless steel hollow section was increased up to 22% for specimens subjected to ETF loading condition. It should be noted that the specimens D150×50×2.5-ETF-a3-F-G and D150×50×2.5-ETF-b3-F-G wrapped with three layers of CFRP and GFRP sheets, respectively, showed a lower initial stiffness compared to the reference test without FRP, as shown in Figure 6. This is due to the top and bottom flanges of the specimens were wrapped with FRP sheets.

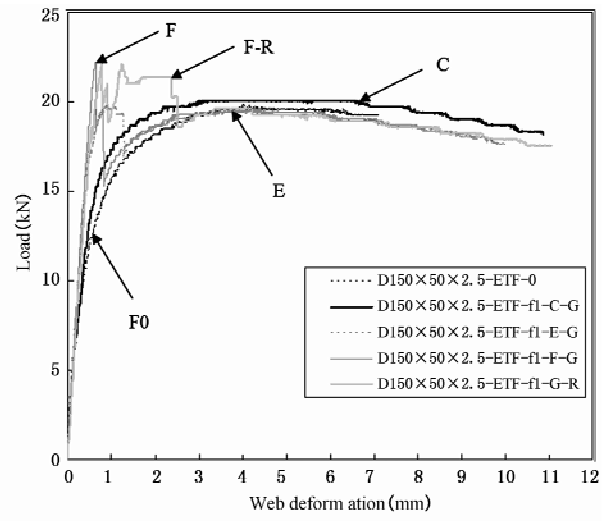

Figure 5 Comparison of different adhesive effects on load-web deformation behaviour of D150×50×2.5-ETF-f1-G specimens using grinding surface treatment

CONCLUSIONS

A test program on fibre-reinforced polymer (FRP) strengthened lean duplex stainless steel hollow section subjected to end bearing load has been presented. The investigation examined two different surface treatments, three different adhesives and six different FRPs for strengthened lean duplex stainless steel sections. The web crippling tests were conducted under End-Two-Flange (ETF) loading condition. In this study, the grinding surface treatment generally provide better performance than the sanding surface treatment for lean duplex stainless steel hollow sections subjected to web crippling. Furthermore, the use of adhesive Araldite 420 and the high strength with lower modulus CFRP CarboDur S1214 laminate plate for the tested lean duplex stainless steel specimens also showed better performance compared to other

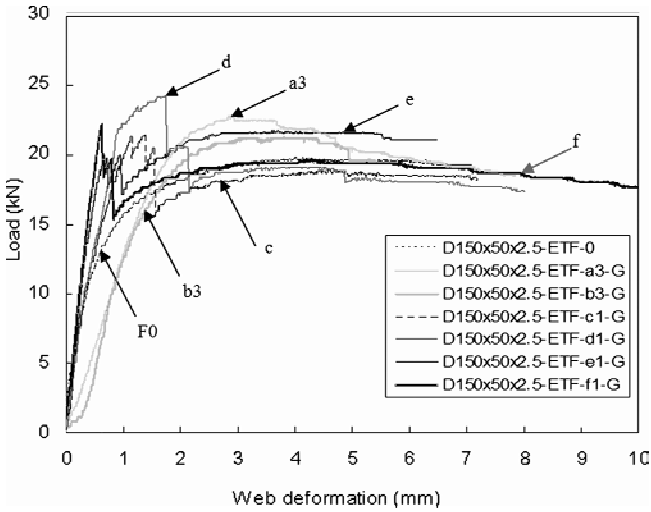

Figure 6 Comparison of different FRP effects on load-web deformation behaviour of D150×50×2.5-ETF-G specimens using grinding surface treatment

adhesives and FRPs. The failure modes of adhesion failure, interlaminar FRP failure and combination of adhesion and interlaminar FRP failure were found in the tests.

ACKNOWLEDGMENT

The authors are grateful to STALA Tube Finland for supplying the test specimens.

REFERENCES

[1] Nilsson, J.O., Chai, G. and Kivisäkk, U., "Recent development of duplex stainless steels", Proceedings of the 6th European Stainless steel Conference, Helsinki, Finland, 2008, pp. 585-590.

[2] Zhou, F. and Young, B., "Experimental and numerical investigations of cold-formed stainless steel tubular sections subjected to concentrated bearing load", Journal of Constructional Steel Research, 2007a, 63(11), pp. 1452-1466.

[3] Zhou, F. and Young, B., "Cold-formed stainless steel sections subjected to web crippling", Journal of Structural Engineering, ASCE, 2006, 132 (1), pp.134-144.

[4] Zhou, F. and Young, B., "Cold-formed high-strength stainless steel tubular sections subjected to web crippling", Journal of Structural Engineering, ASCE, 2007b, 133(3), pp.368-377.

[5] Zhao, X.L. and Zhang, L., "State-of-the-art review on FRP strengthened steel structures", Engineering Structures, 2007, 29(8), pp.1808-1823.

[6] Zhao, X.L., Fernando, D. and Al-Mahaidi, R., "CFRP strengthened RHS subjected to transverse end bearing force", Engineering Structures, 2006, 28(11), pp.1555-1565.

[7] Fernando, D., Yu, T., Teng, J.G. and Zhao, X.L., "CFRP strengthening of rectangular steel tubes subjected to end bearing loads: effect of adhesive properties and finite element modelling", Thin-Walled Structures, 2009, 47(10), pp.1020-1028.

[8] Zhao, X.L. and Al-Mahaidi, R., "Web buckling of light steel beams strengthened with CFRP subjected to end bearing forces", Thin-Walled Structures, 2009, 47(10), pp.1029-1036.

[9] Schnerch, D.A., "Strengthening of steel structures with high modulus carbon fiber reinforced polymer (CFRP) materials" 2005, PhD dissertation, North Carolina State University, Raleigh (NC), pp.17-18.

[10] Xia, S. H. and Teng, J. G., "Behaviour of FRP-to-steel bonded joints", Proceedings of the International Symposium on Bond Behaviour of FRP in Structures, Hong Kong, China, 2005, pp. 411-418.

[11] Wu, C., Zhao, X. L., Duan, W. H. and Phipat, P., "Experimental and numerical study on CFRP strengthened aluminium tubular sections subjected to end bearing force", International Journal of Structural Stability and Dynamics, 2012, 12(1), (Article in Press).

[12] ASTM. "Standard test methods for tension testing of metallic materials", E 8M-97. West Conshohocken: American Society for Testing and Materials; 1997.

[13] AS. "Metallic materials—Tensile testing at ambient temperature", Australian Standard, AS 1391—2007. Sydney, Australia: Standards Association of Australia; 2007.

[14] Islam, S. M. Z. and Young, B., "FRP strengthened aluminium tubular sections subjected to web crippling", Thin-Walled Structures; 2011, 49(11), pp. 1392-1403.

[15] ASCE. "Specification for the design of cold-formed stainless steel structural members", SEI/ASCE 8-02; Reston, VA: American Society of Civil Engineers; 2002.

[16] Fawzia, S., Al-Mahaidi, R., Zhao, X. L. and Rizkalla, S., "Strengthening of circular hollow steel tubular sections using high modulus CFRP sheets", Construction and Building Materials, 2007, 21(4), pp. 839-845.

[17] Kim, S. J., Smith, S. T. and Young, B., "Effect of surface preparation on the strength of FRP-to-mild steel and FRP-to-stainless steel joints", Proceedings of the 5th International Conference on FRP Composites in Civil Engineering, Beijing, China, 2010, pp. 869-872.

[18] Islam, S. M. Z. and Young, B., "Effects of different adhesive and FRP on strengthening of stainless steel tubular structural members", Proceedings of the 13th International Symposium on Tubular Structures, Hong Kong, China, 2010, pp. 273-280.

A PARAMETRIC STUDY ON THE MODIFIED SLENDERNESS RATIO FOR COLD-FORMED STEEL BUILT-UP BACK-TO-BACK CHANNEL STUB COLUMN

* H. H. Lau and T. C. H. Ting

Department of Civil & Construction Engineering, Curtin University, Sarawak Campus, CDT 250, 98009 Miri, Sarawak, Malaysia

* Email: lau.hieng.ho@curtin.edu.my

KEYWORDS

Cold-formed steel, modified slenderness ratio, built-up section, back-to-back, finite elements.

ABSTRACT

Built-up member design is addressed in provision C4.5 of the American Iron and Steel Institute 2001 Specification (AISI). A finite elements model of the built-up member was created for this parametric study on the slenderness ratio formulae of the provision C4.5 in AISI design specification. The governing slenderness ratio of built-up member in the AISI design specification is that a/r does not exceed half of the governing slenderness ratio of the overall built-up member. This study examined the 0.5 requirement for this governing slenderness ratio of the built-up member with or without the use of the modified slenderness ratio of the provision C4.5. The parametric study focused on stub columns with different material thicknesses and connector spacing. Comparison of the finite element and theoretical results concluded that the use of the modified slenderness equations of provision C4.5 will give a more conservative capacity prediction when the spacing, s between the connectors along the length of the specimen increased. Also, with thicker material thickness, the modified slenderness ratio also will give a more conservative capacity prediction.

INTRODUCTION

Built-up cold-formed steel columns are composed of two lipped channels inter-connected using a series of screws. For most structures, the occurrence of a local collapse does not necessarily ensure failure of the whole structure. However, for built-up members, failure of the screws results in an extensive reduction in the overall member strength. Despite the vast availability of literature in the general subject of columns, there is little focus on built-up columns. The American Iron and Steel Institute 2001 Specification (AISI)[1] and AS/NZS 4100[2] give no specific provision for the design of built-up columns except stating that built-up members should be designed with a modified slenderness ratio (Eqn. 1) if there are shear forces induced between the weld or screw connectors. The provision C4.5 of AISI Specification also introduced a minimum fastener strength requirement and a fastener spacing requirement (Eqn. 2) for

built-up members. The fastener spacing requirement can also be rewritten to determine the maximum longitudinal spacing of connections (Eqn. 3). These requirements were rewritten in the form of equations with unified nomenclature as stated in provision C4.5 of the AISI Specification as follows:

$$\text{Modified slenderness ratio } \left(\frac{KL}{r}\right)_m = \sqrt{\left(\frac{KL}{r_{ybu}}\right)_o^2 + \left(\frac{s}{r_{yc}}\right)^2} \tag{1}$$

$$\text{Intermediate fastener spacing } \frac{s}{r_{yc}} \leqslant 0.5\left(\frac{KL}{r_{ybu}}\right)_o \tag{2}$$

$$\text{Maximum longitudinal spacing of connections } s_{\max} = \frac{Lr_{yc}}{2r_{ybu}} \tag{3}$$

where $(KL/r_{ybu})_o$ is the overall slenderness ratio of the entire section about the built-up member axis; s is the intermediate fastener or spot weld spacing; K is the effective length factor; and L is the unbraced member length; $s_{\max}$ is the maximum permissible longitudinal spacing of connectors; r_{yc} is the radius of gyration of one C-section about its centroidal axis parallel to the web; and r_{ybu} is the radius of gyration of the I-section about the axis perpendicular to the direction in which buckling would occur for the given conditions of end support and intermediate bracing.

These equations are introduced to maintain the slenderness ratio of the individual C-section to be less than or equal to half of the slenderness ratio for the overall compression member. This is to ensure that the maximum spacing of the connectors is close enough to prevent buckling of individual C-sections, if any one of the connectors may be loosened or ineffective. The buckling of individual C-sections about their own axes parallel to the web is undesirable as it is at a load equal to or smaller than the buckling load of the overall member. With these requirements in provision C4.5 met, the built-up member would function integrally as a single compression member rather than behaving as individual C-sections. Despite being critical, the modified slenderness ratio is heavily adopted from the American Iron and Steel Construction (AISC) code[3] for hot-rolled, built-up members. This is inconsistent with the fact that the behaviour of hot-rolled steel members is very much different from the cold-formed steel members. Thus, it is the purpose of this research to study the provision C4.5 of the Specification for cold-formed steel built-up back-to-back channel columns.

LITERATURE REVIEW

Research on the slenderness modification for built-up members began as early as 1952, when Bleich[4] proposed an analytical criterion to modify the overall slenderness ratio of battened columns. The proposed equation was limited to battened columns with hinged-end conditions only. Later, Zandonini's[5] study on hot-rolled stitched built-up struts made a greater step as the 1986's AISC Specification introduced the slenderness modification equation for built-up members based on his research study. The modification takes into account the effects of connectors and their spacing on the buckling mode of built-up members. The AISC Specification is the first AISC publication to introduce the slenderness ratio formulae for built-up members. These formulae were later verified and improved by Aslani and Goel[6] with inclusion of the section separation ratio (α).

As the amount of investigations increased, many design codes started to adopt the consideration of the

slenderness ratio. Thus more researchers were interested to further investigate the slenderness ratio effects of the other design codes. In 2004, Lue et al.'s[7] research on the hot-rolled, axially loaded, built-up, double-channel columns concluded that the AISC column design strengths with the modified slenderness ratio were generally conservative. A more thorough research study was conducted by Lue et al.[8] as they made comparisons of the slenderness ratios from various design codes including the AISC-ASD, the AISC-LRFD, the AS-4 100 and the Canadian code CSA S16-01. They found that the design strengths determined based on the slenderness ratio formulae of the Australian Code (AS-4100) are more conservative. Later in 2009, Liu et al.[9] again concluded that the Australian and Canadian design strengths are overall more conservative when compared to the current AISC design because both designs are without the use of a separation ratio (α).

The slenderness modification was first investigated on cold-formed steel built-up sections by Stone and LaBoube[10] in 2005. They investigated the effects of using the modification equation on perforated built-up studs with different material thicknesses and concluded that the results with the slenderness modification were conservative on built-up members. The results with slenderness modification were on average conservative for thin members and highly conservative for thicker members (greater than 0.89 mm (0.035 in.)). Additional work was conducted by Brueggen and Ramseyer[11] on cold-formed channel sections in open- and closed-sections with intermediate, welded stitch attachments. Their research on the built-up stub columns concluded that the AISI design methods to be conservative for compact members but un-conservative for members with slender elements. They also recommended for additional tests to be performed to determine the effects of length and location, spacing, and number of weld attachments on the behaviour of welded built-up members[12]. In a more recent study, Whittle and Ramseyer's[13] research on the closed-section, built-up members concluded that the results were more conservative for longer built-up members and thicker built-up members with the use of the modified slenderness ratio. Moreover, if the fastener and spacing requirements of the provision C4.5 for built-up are followed, strength prediction using the modified slenderness ratio for built-up members is marginally more conservative than using the unmodified slenderness ratio.

FINITE ELEMENTS MODEL

The behaviour of built-up columns composed of thin-walled lipped C-section members connected back-to-back is investigated numerically using the finite elements method. Verification of this finite elements model in predicting ultimate capacities and the corresponding results of the tested specimens were carried out and available in previous authors' publication[14]. A parametric study covering different material thicknesses and connector spacing was performed using these verified results and finite element models. Thus, comparisons of the computed design strengths based on the primary design codes of AISI were made in this paper.

This study used the verified finite elements model generated by a commercially available finite element package-LUSAS version 14.4[15]. Thin-shell elements with four nodes and six degrees of freedom at each node (i.e. QTS4) were used to model the built-up columns. Large displacement and small strains analyses have been incorporated in the finite elements model using the Total Langragrian geometric nonlinearity. Material nonlinearity was also modelled with von Mises yield criteria and plastic hardening. Steel properties for the specimens were obtained from tensile coupon tests and subsequently used to define the nonlinear material attributes in the LUSAS finite elements modelling. The columns were loaded under

uniform compression at the loaded end in automatic increments. The end conditions of the columns were pin ended with the loaded end prevented from rotations at the z-axis, and displacements in both x and y directions. At the other end, the unloaded end was prevented from displacement in all three directions x, y, and z and also prevented from rotation at the z-axis.

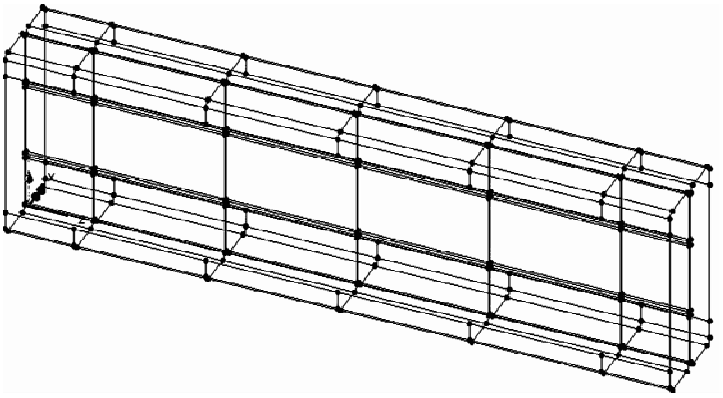

Figure 1 LUSAS Model

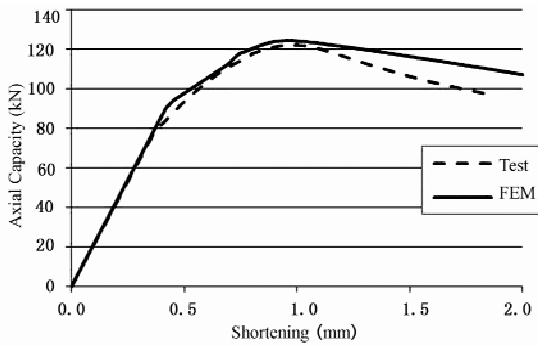

Figure 2 Typical Load vs Displacement Curve for Built-up Stub Column

Each model is 250 mm long and connected at the intervals of 50, 75, 100, 150 or 200 mm. The section size used were simple C lipped channels with web width of 75 mm, flange width of 20 mm, lip width of 10 mm, and thickness is 1.2 mm. The model was set up in such a way that buckling of the specimens would occur in y－y axis only. The finite element model used in this research study is as illustrated in Figure 1. Typical load－displacement curves are shown in Figure 2.

PARAMETRIC STUDY ON BACK TO BACK BUILT-UP STUB-COULMNS

A parametric study was performed concentrating on the behaviour of built-up back-to-back channel stub columns. The purpose of the study was to assess the behaviour of the built-up cold-formed steel compression members and to determine if the present AISI design provision is appropriate for cold-formed steel members. The present study highlighted two parameters identified in[10],[11] and[13] that directly influence the behaviours of the built-up columns. These parameters are identified as: (i) s/L which is defined as the ratio of the clear distance between connectors-to-the overall length of the column; and (ii) t which is defined as the material thickness. This study investigated a total of 12 models which were

classified into 2 specimen groups. The built-up sections were made up of two channels connected together back-to-back as illustrated in Figure 3.

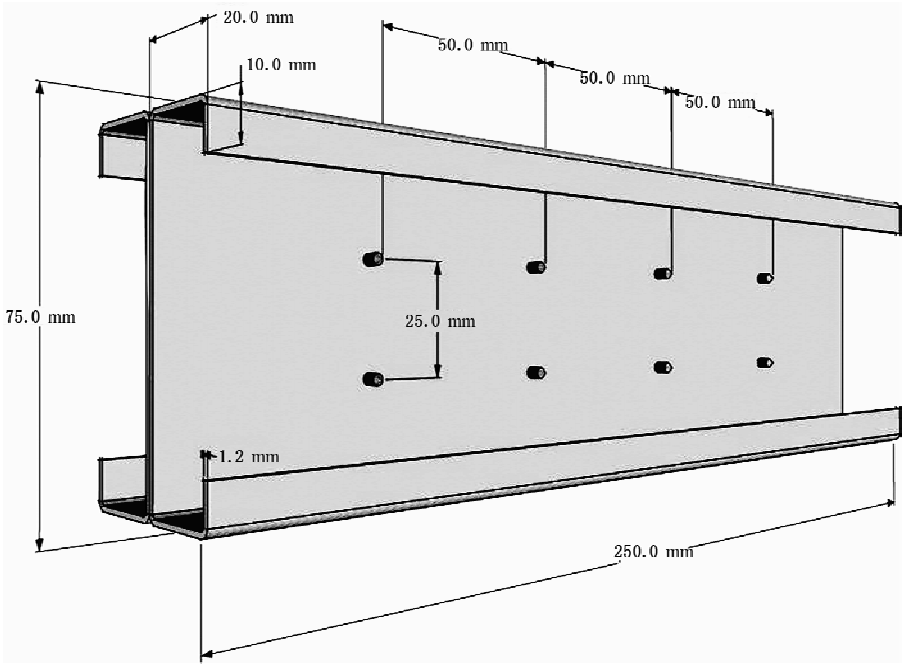

Figure 3 Cross Sectional Geometry and the Configuration of the Investigated Built-up Members

Effect of Thickness (t) on Column Strength

The finite elements model results, P_{FEM}, for four different thicknesses (i.e. 1.0 mm, 1.2 mm, 1.55 mm and 1.95 mm) were compared to the theoretical results calculated in accordance to the AISI specification. Comparisons were also carried out for both modified and unmodified predicted axial capacity, P_n, as determined by provision C4 of the AISI specification. Figure 4 and Figure 5 illustrate the comparison of axial capacity predicted by the finite elements method, the Effective Width Method, and the Direct Strength Method. Results from Figure 4 indicate that for the models with thicker material thickness, the existing AISI design equations without using the modified slenderness ratio are conservative. However, the capacity of the thinner material (1.0 mm) was slightly overestimated. Similarly, comparison was carried out with the modified slenderness ratio in Figure 5. The results obtained were similar but with greater increment for the models with thicker material thickness. Comparison between Figure 4 and Figure 5 shows that the strength prediction for thicker models is more conservative when the modified slenderness ratio is used. For thinner models, the strength predictions by both were very close. This suggests that the modification of the slenderness ratio is not necessary for the thicker materials. For both unmodified and modified slenderness ratios, finite element method consistently overestimates the axial strength predicted by the Direct Strength Method. The finite elements models with the thicker material thickness also show an upward pattern when the modified slenderness ratio is used and the strength predictions are also more conservative. This trend was also observed by Stone and LaBoube's[10] research on built-up studs. In more recent research studies, Whittle and Ramseyer[13] further confirmed that modified slenderness ratio is conservative for members with thicker material thickness.

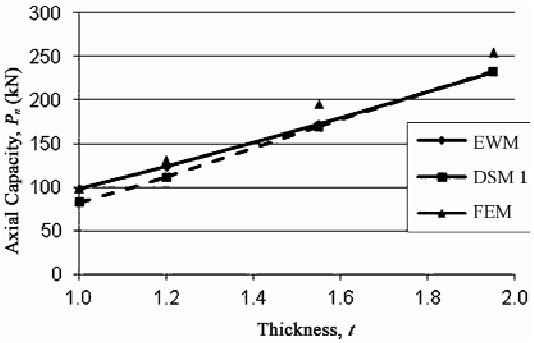

Figure 4 Comparison of Finite Element Results and Calculated Results using Unmodified Slenderness Ratio $(KL/r)_{lu}$

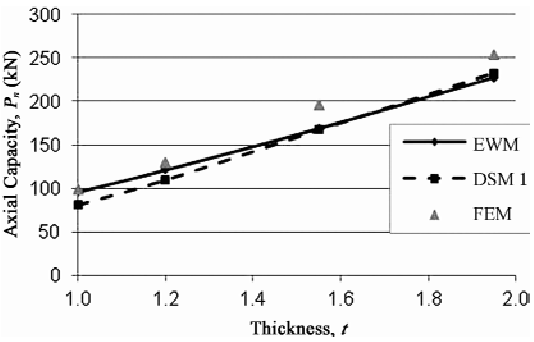

Figure 5 Comparison of Finite Element Results and Calculated Results using Modified Slenderness Ratio $(KL/r)_m$

Effect of Connector Spacing (s) on Column Strength

The finite elements model results, P_{FEM}, for various spacing (i.e. 50 mm, 75 mm, 100 mm, 150 mm and 200 mm) were compared to the theoretical results calculated in accordance to the AISI specification. Comparisons were made to both modified and unmodified predicted axial capacity, Pn, as determined by provision C4 of the AISI specification. Figure 6 illustrates the failure modes of the stub columns at various spacing.

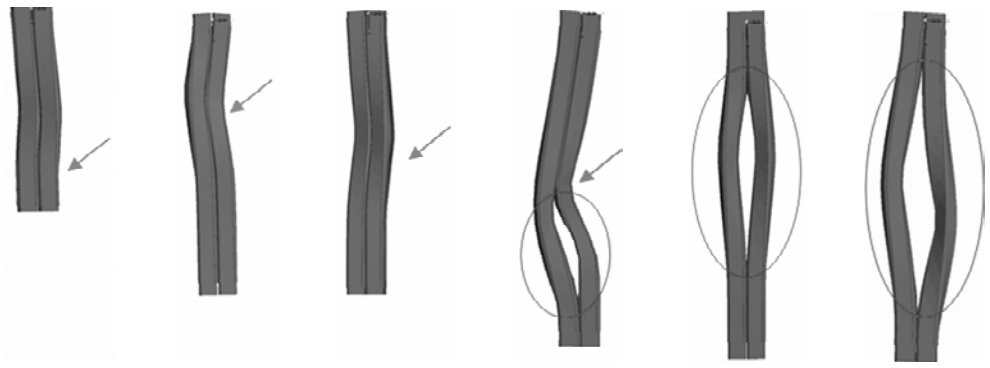

(a) s = 30 mm (b) s = 50 mm (c) s = 75 mm (d) s = 100 mm (e) s = 150 mm (f) s = 200 mm

Figure 6 Buckling Behaviour of Stub Columns at Various Spacing Predicted by LUSAS

Failure Modes

Built-up members buckled in various ways, sometimes as one integral section and often individually with each c-channel buckling separately. Figure 6 shows the buckling behaviour of the built-up members with various spacing. The most common buckling modes for the built-up stub column were local buckling and distortional buckling. The smaller spacing built-up stub columns (30 mm, 50 mm, 75 mm), buckled with angular buckling shapes. The buckled shape appeared as a "hinge" around the screw connection of the column when the deformation increased. The channel sections also moved laterally as a built-up integral section. With connectors at 100 mm spacing, the channel sections moved together laterally at the upper part of the column, while the channels at the bottom part moved separately with the channels prying apart. However, the hinge phenomena occurring at smaller spacing built-up stub columns is still visible. This hinge separates the buckling behaviour into two parts with the upper column buckling integrally and the bottom column buckling separately. Models with larger spacing (150 mm) buckled separately with the channel sections prying apart at mid length due to the lack of fasteners along the length of the member. With the largest connector spacing (200 mm), the prying apart of the channel sections occurred at mid length of the member. Similar buckling behaviours were also observed by Whittle and Ramseyer[13] in their research on the built-up columns with different lengths, and different cross section sizes.

Strength Predictions

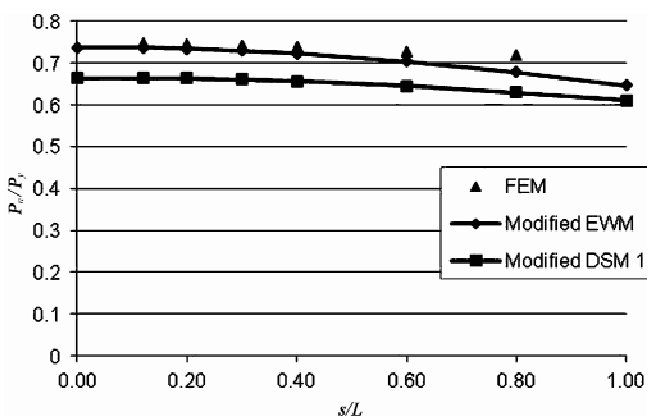

Figure 7 Graph of P_n/P_y vs s/L for BU07512 Stub Column

Figure 7 shows the relationship between the normalized ratio of the spacing between connectors to the overall length of the column (s/L), and the normalized ratio of the predicted load to the yield load of the column (P_n/P_y) for different design methods. Figure 7 shows that connector spacing has a significant effect on the strength of the built-up columns. For the same column length, as the spacing increased, the corresponding ultimate load decreased. This is attributed to higher values of the modified slenderness ratio which directly leads to a reduction in the load carrying capacity of the built-up column. The greater the connector spacing, the C-channels starts to behave individually rather than as one integral section. This is because the overall global buckling of the member is dominating the behaviour, while the effect of the local buckling becomes minimal. These types of columns are more susceptible to distortional and overall buckling effects. This is due to lack of intermediate connectors to hold the c-channels together as an integral built-up column. Thus, explains the reduction of built-up column strength with increased connector spacing. The average strength capacity calculated based on the modified slenderness ratio was

more conservative than the average strength capacity calculated based on the unmodified slenderness ratio. However, if all the fastener and spacing provisions for built-up members in C4.5 were met, the strength prediction without slenderness modification calculation was less conservative than the prediction based on the modified slenderness ratio calculation. This indicates that the strength prediction based on the unmodified slenderness ratio calculation were not conservative for built-up stub columns which do not meet the C4.5 spacing provision. For built-up stub columns that met the C4.5 spacing provision, the finite element results were closer to the theoretical results predicted using modified slenderness ratio.

CONCLUSIONS

A finite elements method is used to investigate the effect of the material thickness and the connector spacing on the behaviour of the built up column. The finite elements model results were compared to theoretical buckling capacities calculated based on the provision C4.5 for modified slenderness ratio of AISI Specification. Based on the results presented, it is reasonable to draw the conclusions that the average strength capacity calculated based on the modified slenderness ratio of provision C4.5 is conservative for built-up members. Secondly, the modified slenderness ratio of the provision C4.5 is not necessary for thicker members when computing axial capacity. Finally, the capacity of built-up sections decreased with the increased spacing, s. For the models with larger spacing, the modification ratio resulted in a more conservative buckling strength prediction. However, further studies with different cross section sizes of channel sections and different spacing with different member lengths should be studied analytically and experimentally to reaffirm the conclusion drawn.

ACKNOWLEDGEMENTS

The authors would like to thank EcoSteel Sdn Bhd for supplying the specimens for the testing.

REFERENCES

[1] American Iron and Steel Institute, AISI. "Commentary on North American specification for the Design of Cold-formed Steel Structural Members", American Iron and Steel Institute, Washington, DC. 2007.

[2] AS-4100. Steel Structures. Homebush (NSW, Australia): Standards Association of Australia; 1998.

[3] AISC "Load and resistance factor design specifications for structural steel buildings", 1st edition, American Institute of Steel Construction, Inc.; Chicago (IL). 1986.

[4] Bleich, F., "Buckling strength of metal structures", McGraw-Hill, New York, 1952, pp. 167 C92.

[5] Zandonini, R., "Stability of compact built-up struts: experimental investigation and numerical simulation", Construzioni metalliche, 1985, No. 4.

[6] Aslani, F. and Goel, S.C., "An Analytical Criterion for Buckling Strength of Built-up Compression Members", Engineering Journal, AISC, 1991,28(4),pp.159-168.

[7] Lue, D.M., Yen, T., Liu, J.L. and Hsu, Y.T., "Experimental investigation for buckling strength of double-channel columns", Proceedings of the annual stability conference, 2004, Long Beach, CA.

[8] Lue D.M., Yen, T. and Liu, J.L., "Experimental investigation on built-up columns", Journal of Constructional Steel Research, 2006, Vol.62,1325-C1332.

[9] Liu, J.L., Lue, D.M. and Lin, C.H., "Investigation on slenderness ratios of built-up compression members", Journal of Constructional Steel Research 2009,Vol. 65,237-C248. (2009)

[10] Stone, T. A. and LaBoube, R. A., "Behaviour of Cold-formed Steel Built-up I-sections, Thin-Walled

Structures", 2005, Vol. 43, pp. 1805-1817. (2005)

[11] Brueggen, B. and Ramseyer, C., "Capacity of built-up cold-formed steel axial compression members, Structural stability research council", Proceedings of the Annual Stability Conference, Rolla, Missouri. 2005.

[12] Brueggen, B. and Ramseyer, C., "Cold formed steel joist member buckling capacity testing", Report for star building systems, 2003, Oklahoma City. Norman, Oklahoma: Fears Structural Engineering Laboratory.

[13] Whittle, J. and Ramseyer, C., "Buckling capacities of axially loaded, cold-formed, built-up C-channels", Thin-Walled Structures, 2009, Vol. 47, pp. 190-201.

[14] Ting, T. C. H. and Lau, H. H., "A Numerical Investigation on Cold-formed Steel Built-up Back-to-back Channel Stub Columns, Proceedings of the International Conference on Steel and Aluminium Structures", 2011, Kuching, Sarawak, Malaysia.

[15] FEA Co., Ltd., "Lusas Element Reference Manual & User's Manual (version 14.4)", 2010, United Kingdom.

Proceedings of Seventh International Conference on Advances in Steel Structures, 2012, Nanjing, China

OPTIMISATION OF COMPOSED DOUBLE-Z COLD-FORMED STEEL MEMBERS

* I. Georgieva[1], L. Schueremans[1], L. Pyl[1, 2] and L. Vandewalle[1]

[1]Civil Engineering Department, Catholic University Leuven, Kasteelpark Arenberg 40, B-3001 Heverlee, Belgium

[2]Department Mechanics of Materials and Constructions, Free University Brussels, Pleinlaan 2, B-1050 Brussels, Belgium

* Email: Iveta.Georgieva@bwk.kuleuven.be

KEYWORDS

Cold-formed steel, built-up members, FEA, parametric study, non-linear buckling analysis.

ABSTRACT

The standard cold-formed steel profiles are easily paired to form built-up members, when higher loads are to be taken. The resulting members are more stable and of higher strength; besides, the production method remains unchanged. Previous investigations, performed by the authors, revealed the response and failure pattern of one type of built-up member. Full-scale tests were performed on double-Z members, both in compression and weak-axis bending, in order to study how the flexible interconnection between the Z-profiles influences the member response. A finite element model was validated based on the experiments. This numerical model is used to optimise the geometry of the investigated members, so that higher ultimate strength-to-weight ratios can be achieved. The objective is to deliver highly stable member geometry and to exclude effects that can deteriorate the axial buckling capacity. The member type can then be employed to take up the increasing loads and spans in ambitious structural applications of light-steel framing.

INTRODUCTION

Cold-formed steel (CFS) profiles are being used for increasingly ambitious undertakings. Airplane hangars, large supermarkets, industrial and agricultural halls are assembled entirely from light galvanized profiles and corrugated sheets. The assets are many-the corrosion resistance, the material recyclability, the large strength-to-weigh ratios and avoiding the use of heavy-lifting equipment on site are just a few. Such buildings are exposed to various environmental and service conditions, and due to their large spans, thin-walled trusses and/or composed elements are more appropriate for primary members. Moreover, it is cheaper and easier to couple Z, C or Σ profiles into built-up members, than to readjust the production lines and manufacture new more stable, but more complex profiles.

Composed light members behave in a far different way than their conventional hot-rolled steel (HRS) counterparts. The thin profiles accumulate various types of buckling effects; the interaction between the profiles and the connection pieces is more difficult to predict, yet more important for the overall response. What is more, the initial geometrical imperfections and the residual stresses, caused during the production phase alone, are far more pronounced.

Whether modern-day structural standards are applicable to the design of built-up CFS members has not been validated experimentally. The available design guidelines treat single profiles mainly, therefore such predictions may not account for many aspects in the behaviour of the members. Full-scale tests, on the other hand, allow the engineer to establish the actual behaviour and failure mechanism of the members, prior to proposing a design method for a certain type of built-up member geometry. The following paragraphs present the conclusions drawn from previous investigations, performed by the authors, on double-Z CFS members.

DOUBLE-Z CFS COLUMNS-EXPERIMENTAL AND NUMERICAL BACKGROUND

Specimens

Various fasteners may be used to assemble built-up CFS members-bolts, screws, spot welds, etc. In this paper, bolted members are treated. These comply best with the current European engineering practice. To be able to assemble the members, the profiles are produced with a 1-2 mm bolt-hole clearance. This simplifies the assembly, but causes unavoidable slip when the fasteners are loaded in shear. The galvanised surface of the profiles and the small thickness of the connected sheets prevent the use of pre-stressed bolts. Such slippage in the members has a major effect on the response, both related to the strength and to the stiffness of the member[1].

The specimens consist of two Z-profiles, interconnected by HRS spacers along the member length (spacing 1.0, 1.5 and 2.0 m), and by column base HRS connections at the member ends (Figure 1). Because such members are employed as columns and girders in portal frames (for industrial halls and other frame structures), in practice, special connection pieces are employed at the ends, to transfer considerable bending moments (Figure 1c). The double-Z CFS cross-section is characterised by flexible interconnection between the two Z-profiles. As established in[2], the end connections have a major influence of the interconnection quality between the constituents of a built-up member. Therefore, the two columns bases are included in the investigation, with bolt-spacing as used in practice. In this way, the effect of these connections on the overall stiffness, the warping in the member and the failure mode can be seen.

Experiments

Twelve tests have been performed in weak-axis bending (4 m span), to establish the stiffness of the member for its axis of symmetry. Eight tests have been performed in compression (4.45 m length), to obtain the structural response and failure mode of slender columns with the adopted cross-section. Details on the performed experiments can be found in[1]. From the tests, important aspects of the behaviour of such members have been established[3]. The post-ultimate stage of the columns response was captured by performing the tests as displacement controlled.

Failure Mechanisms

The beams failure was facilitated by the small width of the edge stiffeners of the Z-profiles. Distortional buckling (DB) appeared in all specimens in the midspan region, resulting in sudden snap-through of the top flange and severe yielding there (Figure 2a). The short lips in the contact zone lost contact eventually, also due to DB (Figure 2b), leading to sudden failure of the member. A significant longitudinal slip was established in each of the 12 tests.

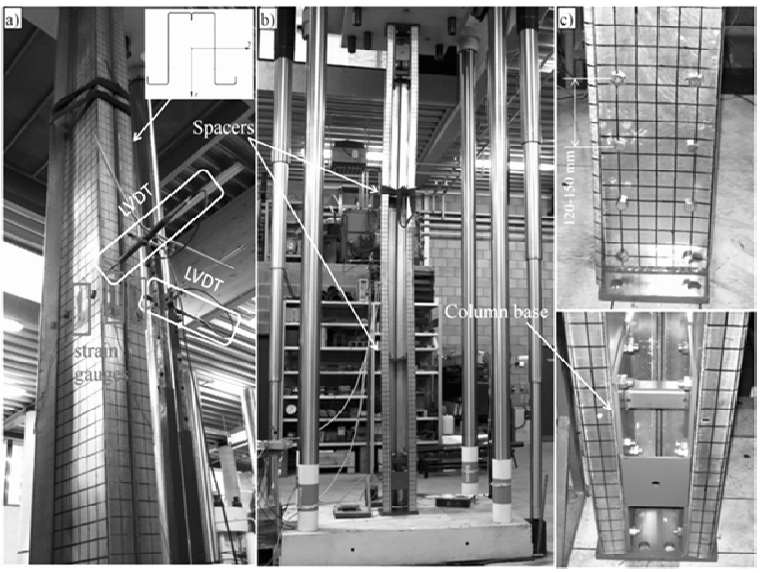

Figure 1 Experiments: (a) Column tests-specimens and equipment; (b) Columns-test setup and failure mechanism; (c) End connection

The column specimens failed in torsional-flexural buckling, TFB (Figure 1b and Figure 2f), which is typical for singly-symmetric cross-sections. No torsional buckling of the Z-profiles was observed between the HRS spacers and the interconnection spacing (in the range 1-2 m) did not influence the obtained ultimate resistance[1]. Overall TFB buckling coupled with local buckling in the slender webs of the Z-profiles, see Figure 2e. At ultimate load, distortional deformations appeared in one of the outer flanges, resulting in subsequent yielding, see Figure 2d. This yielding stage is represented in the load-lateral deflection response by a plateau (see test results in Figure 3)-the load was retained while the rate of lateral deflections increased considerably.

Numerical analysis was used to simulate the response, observed during the tests[4]. The finite element model demonstrated that fasteners play an important role for the member behaviour. Unlike members, built-up with screws (or welds), where a limited number of screws can result in a perfect and continuous interconnection[5], the complex deformation pattern of CFS members eventually leads to shear forces in the interconnecting bolts and eventual slip. To simulate the experimentally observed response, trilinear springs had to be introduced at the bolt locations, to represent the effects of slip and bearing in the thin steel sheets[4]. This reduced the overall stiffness of the member, resulting in overall capacities, lateral deflections and strains, comparable to the ones that were measured.

Initial imperfections showed to have a major influence on the axial buckling capacity of the slender

columns, specifically the overall lack-of-straightness. Such imperfections introduced a stress gradient in the cross-section, resulting in the columns moving laterally, mainly in the direction of weak-axis bending.

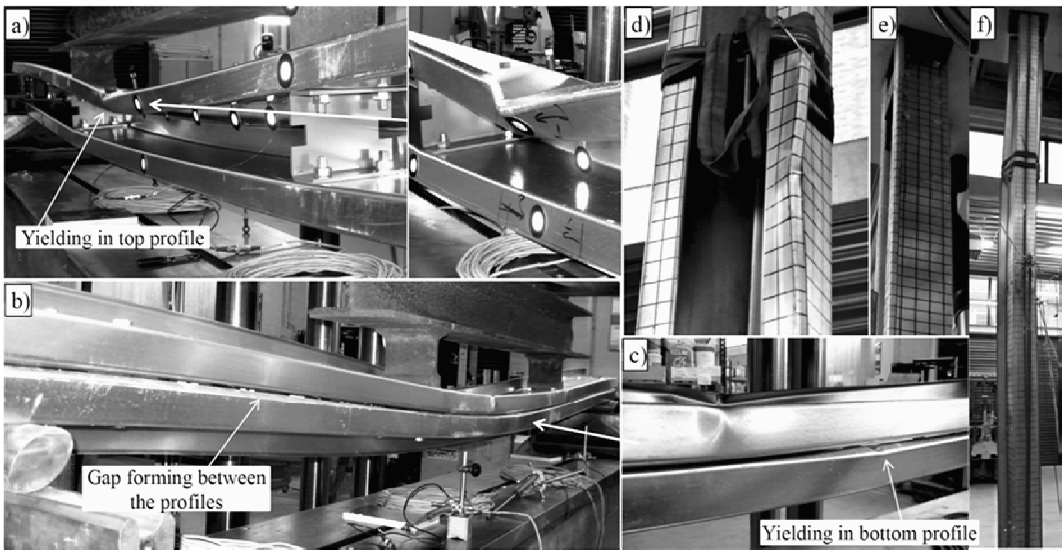

Figure 2 Failure mechanism: (a) Beam tests-yielding top flange; (b) and (c) Beam tests-loss of contact; (d), (e) and (f) Column tests-distortional buckling, local buckling and overall buckling

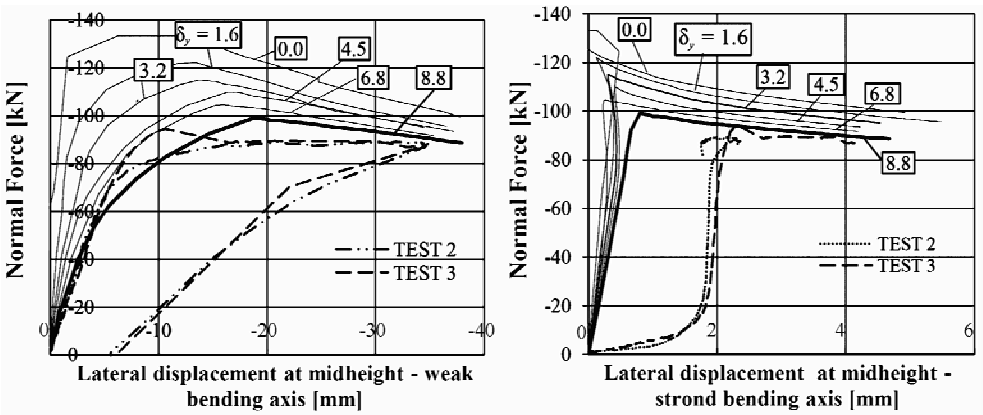

Figure 3 Lateral response of the tested columns-experiments vs. numerical results

The numerical model was employed to study the columns sensitivity to initial imperfections[6]. An initial lateral bow was introduced in the models and varied within the production tolerances, which are given in[7]. The numerical load-deflection response of a specimen, in function of the introduced overall imperfection, δ_y, is given in Figure 3, and compared to the experimental results. Depending on the amplitude of the overall imperfections, the obtained capacity may vary considerably. The sensitivity of the axial buckling capacity to local and distortional imperfections is restricted though, due to the large slenderness of the studied columns[7].

Conclusions

Regardless of the additional flexibility, due to slip in the bolted connections, the test results showed that

the double-Z CFS cross-section is a reliable and economic solution for compressed members in light-steel framing. The column specimens withstood loads, higher than the capacity, predicted by the equations, given in[8] and[9] and by the direct strength method, given in[9] (see[3]). The large sensitivity to geometrical imperfections, and the low stresses attained were due to the large slenderness of the members, which could be restricted by proper lateral bracing.

Knowing the actual response of the member, amendments to the member geometry can be made, so that double-Z members with higher strength-to-weight ratios can be obtained.

FINITE ELEMENT MODEL

Finite element simulations were performed in ANSYS v 12.1, using shell elements (SHELL181) to represent the connected CFS and HRS plates, and springs (COMBIN39 elements) to represent the fasteners. Model calibration was performed, in order to obtain comparable deflections for the beam specimens from the experiments and the model. The calibrated model was then validated against test data from the column tests.

The model was intended for parametric studies of different cross-section proportions and steel grades. Therefore, it was important to restrict the calculation time needed for a single run by making certain simplifications in the geometry of the profiles and connection pieces. The rounded corners of the Z-profiles were assumed as sharp, since the proper meshing of these requires that the element dimensions be reduced 5–10 times. No contact elements were used to represent the interaction between the constituents of a specimen. The interaction between profiles and connections was represented by spring elements at the bolt positions only. The contact between the Z-profiles was ignored, due to the small contact area. Residual stresses were not included.

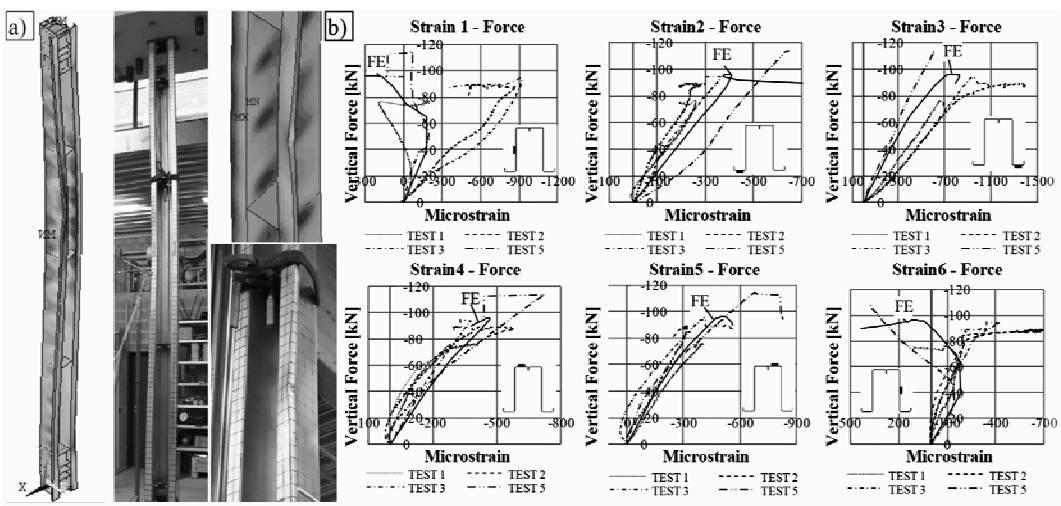

Figure 4 Experimental vs. numerical results: (a) Failure mode; (b) Normal strains measured at mid-height

The model (GMNIA) delivers satisfactory prediction of the column behaviour, when geometrical imperfections, comparable to the production tolerances, are introduced in the analysis (Figure 3 and Figure 4). Good agreement is obtained in terms of failure mode, ultimate capacity, strain patterns in the

mid-height cross-section[6], see Figure 4. Balance is established between computational effort and the accuracy of the model predictions.

Localised imperfections are introduced as well, also varied within the production tolerances. Their effect on the overall capacity, however, is much less significant (less than 3 kN), due to the large slenderness of the tested members[6].

AXIAL BUCKLING CAPACITY-PARAMETRIC STUDY

Originally, two cross-section sizes were tested-Z200-1.5 with Z-profiles of height 200 mm and thickness 1.5 mm, of steel grade S280, and 2xZ250-2.0 with Z-profiles of height 250 mm and thickness 2.0 mm, of steel grade S350. The parametric study is performed using the validated finite elements model, by varying a certain characteristic of the member at each run. To obtain double-Z members with optimised geometry, changes in the profile thickness, yield strength, lip width c, are considered. Table 1 lists the modifications, considered in the study.

TABLE 1 PARAMETRIC STUDY-INPUT FOR THE DIFFERENT SIMULATIONS

Simulation	2xZ200-1.5				2xZ250-2.0			
	Yield Strength [MPa]	Thickness [mm]	Lip width c [mm]	Cover plate	Yield Strength [MPa]	Thickness [mm]	Lip width c [mm]	Cover plate
Original	280	1.5	22	no	350	2.0	21.5	no
A	350	1.5	22	no	400	2.0	21.5	no
B	400	1.5	22	no	450	2.0	21.5	no
C	450	1.5	22	no	500	2.0	21.5	no
D	280	2.0	22	no	350	2.5	21.5	no
E	280	2.5	22	no	350	3.0	21.5	no
F	280	3.0	22	no	350	3.5	21.5	no
G	280	3.5	22	no	350	4.0	21.5	no
H	280	1.5	25	no	350	2.0	25	no
I	280	1.5	30	no	350	2.0	30	no
J	280	1.5	35	no	350	2.0	35	no
K	280	1.5	40	no	350	2.0	40	no
L	—	—	—	—	350	2.0	45	no
M	280	1.5	22	yes	350	2.0	21.5	yes
N	280	1.5	22	yes	350	2.0	21.5	yes

Interconnection Spacing

From the previous investigations it is established that the interconnection spacing does not influence the overall capacity, when the spacing is varied in the range 1-2 m. Denser spacing would be too labour-consuming on the construction site; moreover, to restrict distortional buckling in the members, a spacing of below 300 mm must be adopted. Therefore, an alternative in considered in the parametric study. A cover plate is assumed to be bolted in the mid-region of the columns, where DB occurred during the tests. The distance between the fasteners that interconnect the built-up member and the cover plate, along the length of the member, is assumed 150 mm (simulation M) and 90 mm (simulation N). The thickness of the cover plate is taken as equal to the thickness of the Z-profiles.

Results

The results of the parametric study are summarised in Figure 5. The figures presents the normalised compression capacity, $N_{c,ult}$, calculated according to:

$$N_{c,ult} = N_{model} \frac{A_{original}}{A} \frac{f_{yb,original}}{f_{yb}} \quad (1)$$

where N_{model} is the ultimate capacity, predicted by the FE model, A is the cross-section area of the altered built-up member (cover plate included) and f_{yb} is the yield strength of the profile material. The results are drawn in function of the interconnection spacing s, as originally assumed prior to the experiments-namely for 1.0, 1.5 and 2.0 m. The results show, nevertheless, that the effect of the variation of s in this range is negligible.

Increasing the yield strength does not improve the overall member capacity-N_{model} remains unchanged (Figure 5). Due to torsional-flexural buckling, the members retain stresses significantly lower than their yield strength, before they lose their overall stability. Only yield strengths, higher than the original yield strength, $f_{yb,original}$, are considered, because steel grades S280 and S350 are among the mildest steel, used to produce CFS profiles nowadays.

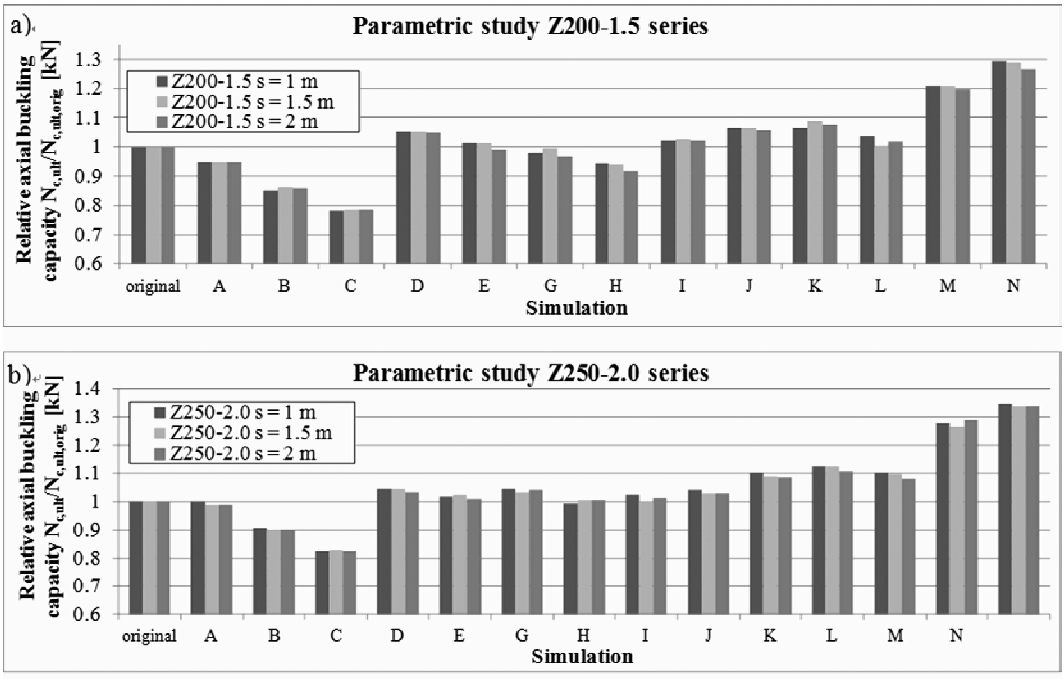

Figure 5 Results from parametric study-relative elastic buckling capacity

The parametric study allows for an optimum thickness of the Z-profiles to be established. For the 2xZ200-1.5 members the optimum thickness is found at 2.0 mm, whereas for the 2xZ250-2.0 members it may be determined in the range of 2.5-3.5 mm.

Lengthening the lip of the edge stiffeners is responsible for a notable improvement in the axial buckling capacity (7%-8 %). There is an overall trend in academics to advice engineers to extend the lip width

c[10], so that the elastic critical stress for both local and distortional buckling can be increased. In the case of double-Z CFS members, increasing the lip width also prevents loss of contact between the 2 Z-profiles when bending occurs.

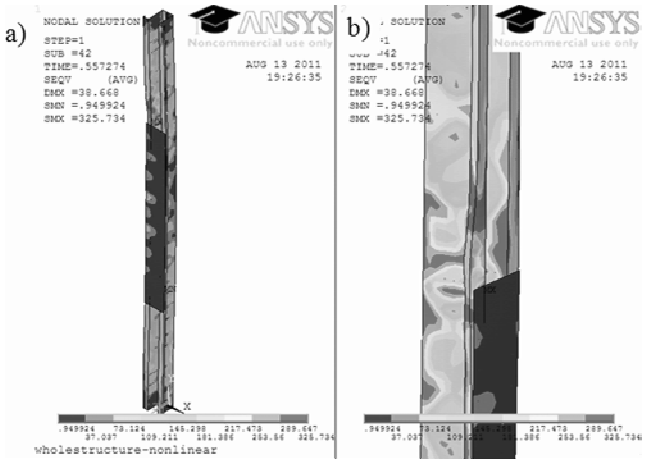

Figure 6 Failure mode-specimen with cover plate: (a) global deformation and stress; (b) yield mechanism

A more efficient way to reduce the effect of distortional buckling is to add a cover plate to connect the two outer flanges of the section (Figure 6a). Such a plate is added in simulations M and N and is assumed to be connected to the double-Z members by bolts with spacing 150 mm for simulation M and 90 mm for simulation N. The plate is added only in the mid-region of the columns (with length 2 m for interconnection spacing 1.0 and 2.0 m, and length 1.5 m for interconnection spacing 1.5 m), where a distortional-yielding mechanism was observed during the tests. The cover plates produced an overall gain of 20%–28% in overall capacity for the fastener spacing of 150 mm, and a gain of 28%–34% for the fastener spacing of 90 mm. This emphasizes the importance of restricting distortional buckling for the investigated type of section on one hand, and of increasing the torsional stiffness, on the other.

CONCLUSIONS

A cross-sectional optimisation for double-Z built-up cold-formed steel columns is performed using FEA. The numerical model is based on previous full-scale experimental studies of the type of member in bending and compression. The parametric study shows that by rational choice of the dimensions of the cross-section parts and the material properties, higher strength-to-weight rations may be obtained. The gain in resistance remains restricted though (<10%).

The investigated slender columns showed almost no improvement in their overall capacity, when higher yield strengths are considered. Due to the low stresses attained by the columns before the onset of overall buckling, the use of higher grade steel is not warranted. An optimal thickness for the Z-profiles can be established from the investigation. Increasing the width of the edge stiffener also showed to increase the overall capacity, due to the major effect distortional buckling (and the prevention of it) has on the overall capacity. Adding an additional cover plate to prevent distortion resulted in a notable improvement in the overall resistance of the members −20%–35%, depending on the fastener spacing.

REFERENCES

[1] Georgieva, I.B., Schueremans, L., Pyl, L. and De Roeck, G., "Experimental investigation of built-up double-Z members in bending and compression", Thin-Walled Structures, 2011, submitted.

[2] Sherman, D.R. and Yura, J.A., "Bolted double angle compression members", Journal of Constructional Steel Research, 1998, 46(1-3), pp.470.

[3] Georgieva, I., Schueremans, L. and Pyl, L., "Composed columns from cold-formed steel Z-profiles. Experiments and code-based predictions of the overall resistance", Engineering Structures, 2012, accepted for publication.

[4] Georgieva, I.B., Schueremans, L., Pyl, L. and De Roeck, G., "Non-linear finite element analysis of built-up members of cold-formed steel profiles", International Conference on Thin-Walled Structures, Timisoara, Romania, 2011, vol. 1, pp.305-312.

[5] Veljkovic, M. and Johansson, B., "Thin-walled steel columns with partially closed cross-section: Tests and computer simulations", Journal of Constructional Steel Research, 2008, 64(7-8), pp.816-821.

[6] Georgieva, I.B., Schueremans, L., Pyl, L. and De, R.G., "Numerical investigation of built-up cold-formed steel columns. Analysis of geometrical imperfections", EUROSTEEL, 2011, vol 1, pp.87-92.

[7] EN10162: 2003-Cold rolled steel sections. Technical delivery conditions. Dimensional and cross-sectional tolerances, ECCS, 2003.

[8] EN 1993-1-3:2006. Eurocode 3: Design of steel structures, Part 1-3: General Rules. Supplementary rules for cold-formed thin gauge members and sheeting, ECCS, 2006.

[9] "North American Specification for the Design of Cold-Formed Steel Structural Members", 2007, American Iron and Steel Institute.

[10] Members, Committee on Specifications for the Design of Cold-formed Steel Structural Members, Direct strength method (DSM)-Design Guide, 2006, 171.

FLEXURAL BEHAVIOUR OF PURLIN-ROOF-SHEETING ASSEMBLIES

* J. Yang, Q. Liu and A. H. C. Chan

School of Civil Engineering, University of Birmingham, Birmingham, B15 2TT, UK
* Email: j.yang.3@bham.ac.uk

KEYWORDS

Sigma purlin, roof sheeting, purling-sheeting interaction, flexural behaviour, downward load, uplift load, flexural stiffness, moment resistance.

ABSTRACT

One of the design aspects of light roof structures is to consider the interactive effect between purlins and roof sheeting. This paper presents an experimental study of the flexural behaviour of simple span cold-formed steel sigma purlins screw-fastened with roof sheeting. A range of 27 sigma purling-sheeting assemblies were subjected to both downward and uplift loading tests, from which their different behaviour in terms of flexural stiffness, failure mode and ultimate load was examined. Five typical failure models have been observed from tests; two for the downward load case and three for the uplift case. It was discovered that the failure modes of sheeted purlins were highly related to their thickness. This work is the first one of this kind that investigates the sheeted sigma purlin with high strength and subjected to both downward and uplift loads. Test results also inform the development of design proposals for sigma purlins that most codes or standards have yet covered.

INTRODUCTION

Modern light roof constructions for industrial or warehouse buildings normally comprise light purlins attached with roof sheeting system. One of the most popular options of purlins is the cold formed steel (CFS) light gauge sections such as Z, C or sigma sections. These purlins are supported on raft beams via brackets and act as a secondary structural system. Due to their small wall thickness, these types of purlins are susceptible to buckling failure[1, 2]. A wide range of light roof sheet systems have emerged recently to accommodate both the structural and thermal design requirements. A simplest and most economical sheeting system is the single layer trapezoidal profiled steel sheets. These profiled sheets are fitted to purlins by using self-drilling screws with rubber bonded washers in order to achieve water tightness. Wind loads can be excreted on roof structures in both positive and negative directions, which will cause different structural behaviour in roof structures. Roof sheets, once installed onto purlins, will provide beneficial effects on their structural performance by introducing a certain degree of restraining effect. Therefore, it is common to consider this interactive behaviour between purlins and sheeting in the modern roof design practice[3].

A series of full scale tests were reported to investigate the load resistance of typical CFS sigma, Z, and Zeta purlin-sheeting systems under the gravity load[4]. Another experimental study was performed to examine the influences of the fastener location and the flange to lip width ratio on the load resistance of C and Z purlin-sheeting systems under the gravity load[5]. Both a full[6] and a simplified FE models[7] have been developed to evaluate the load resistance of CFS purlin-sheeting systems under both gravity or uplift loads. A novel analytical model[8] was developed to calculate the load resistance of CFS purlin-sheeting systems under the gravity or uplift load. In that model, a translational spring was utilized to account for the effect of partial rotational restraint provided by sheeting, and an artificial lateral force was introduced to consider the effect of torsional moment caused by the applied load. This analytical model was later formally adopted by Eurocodes[3] to calculate the load resistances of CFS purlin-sheeting systems. An approach called as *R*-factor method is recommended by North American Specification AISI S100[9] to calculate the load resistance of CFS purlin-sheeting systems. The employment of theR-factor method is rather direct, that is, applying a reduction factor (*R* factor) to the cross-sectional load resistance to obtain the resistance of the purlin-sheeting system. The reduction factors suggested in AISI S100 are currently only available for C and Z sections. Calibration studies were carried out to refine these reduction factors by using the results of a series of C and Z purlin-sheeting system tests performed in the University of Sydney[10]. These calibrated reduction factors was later on adopted by Standards Australia[11].

This paper reports an experimental research investigation into the flexural behaviour of a series of purlin-sheeting assemblies. Each assembly was composed of two single span cold formed steel (CFS) sigma purlins attached with trapezoidal profiled roof sheets. A total of 27 full scale assemblies were subjected to downward and uplift loadings, respectively. Test details and results are reported in this paper together with the discussion of results and observations.

TEST PROGRAMME

In this test programme, purlin-sheeting assemblies, as shown schematically in Figures 1 (a) and (b), were subjected to both downward and uplift loadings representing the actions of positive and negative wind pressure applied on a roof system. They will be respectively referred to as downward and uplift loading tests hereafter. In each assembly, a pair of identical sigma purlins of 6 m length was placed in parallel with opposing faces. The result of such arrangement was to increase the restraint effect on the lateral movement of purlins from the sheeting, through the opposite directions of their torsional movement; therefore, compensating the low in-plane shear stiffness of sheeting due to a limited sheet width. Both purlin members were covered by single layer screw-fastened roof sheets throughout their spans. A six-point loading system was applied through four spreader beams placed on each test assembly.

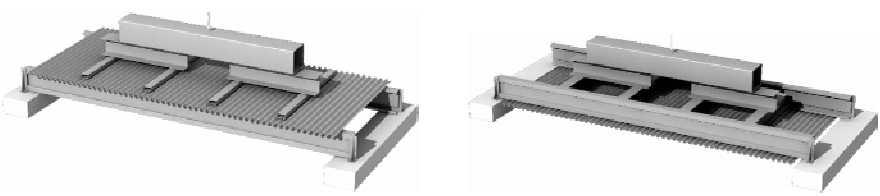

(a) Downward loading test (b) Uplift loading test

Figure 1 Overall view of test assemblies

Nine sigma purlin sections of different depth and thickness were chosen in this test programme. Two duplicated tests were carried out for the downward loading test to demonstrate the repeatability of test results and only one test was for the uplift loading test. A three-part reference system is used to identify each test. For instance, if a test is referred as SD60-20012-1 or SU60-20012-1, the first part "SD60" or "SU60" indicates that it is a single span downward or uplift test with 6m specimen length; the second part "20012" refers to the section dimensions, i.e., 200 mm deep and 1.2 mm thick; and the last part "1" is the number of the duplicated test.

The sigma purlin sections chosen for tests include three depths, i.e., 200, 240 and 300 mm[1]. The Young's Modulus and 0.2% proof stress were measured by following BS EN 10002, and the thickness was measured at points located in the inner web, top flange and bottom flange, respectively. A type of single layer trapezoidal steel roof sheeting system was used to cover these purlins. They were measured 0.69 mm thick and were cut and delivered in 1 m length. The purlin/roofing assembly was supported by two mass concrete blocks that have been crane lifted into pre-marked positions through stiffened angle cleats that were made of mild steel and pre-fixed onto the concrete blocks by using M16 expansion anchor bolts. The connections between cleats and purlins are through Grade 8.8 M12 bolts for section series 200 and 240 and M16 for section series 300. Standard clearance in bolt holes allowed a relative horizontal movement between two bolts and therefore did not provide any significant rotation fixity at supports. The horizontal distance between the outer webs of both purlins was 0.66 mm and the clear span length of all tested assemblies was 5.942 m. Six pieces of 1×1 m roof sheets were placed on the top flanges of purlins, with the corrugation profiles perpendicular to the longitudinal span. Adjacent sheets were overlapped at one cap length of 71 mm (see Figure 2) producing a total covered length 5.66 m. The roof sheets were connected to purlins at every other corrugation trough apart from the overlap joints where screws were applied at every trough.

Continuously increasing displacements at a rate of 0.1 mm per second were applied by a loading jack in the 60T Mand test machine to the SHS beam until passing the ultimate failure point. Between the loading jack and this beam, a load cell was placed to record the value of applied load at a unit sampling frequency. LVDTs were instrumented to measure the vertical and lateral deflections at the mid- and quarter-span points of each purlin.

TEST RESULTS

Table 1 summarizes the recorded ultimate load P_{ult} and the corresponding bending moment in the mid-span point $M_{Rd,t}$. Also presented are the failure modes, i.e., the local and distortional buckling of purlin (type Ⅰ), the local failure of roof sheets together with the distortional buckling of purlin (type Ⅱ), the local and lateral torsional buckling of purlin (type Ⅲ), the lateral torsional buckling of purlin in a symmetric fashion (type Ⅳ) and the lateral torsional buckling of purlins in an asymmetric fashion (type Ⅴ). The detailed information of these failure modes are provided in the following section.

Figure 2 shows the load vs. mid-span deflection curves of selected specimens, in which the deflection is the average value of two parallel purlins. For comparison purpose, corresponding theoretical results calculated based on the linear beam theory are also presented in the same graphs.

TABLE 1 TEST RESULTS

Test ID	P_{ult} (kN)	$M_{Rd,t}$ (kNm)	Failure mode	Test ID	P_{ult} (kN)	$M_{Rd,t}$ (kNm)	Failure mode
SD60-20012-1	9.05	8.0	Type Ⅰ	SU60-20012-1	6.12	5.4	Type Ⅲ
SD60-20012-2	8.55	7.6	Type Ⅰ				
SD60-20016-1	13.03	11.5	Type Ⅰ	SU60-20016-1	8.31	7.4	Type Ⅲ
SD60-20016-2	13.14	11.6	Type Ⅰ				
SD60-20025-1	21.05	18.6	Type Ⅱ	SU60-20025-1	13.67	12.1	Type Ⅴ
SD60-20025-2	20.90	18.5	Type Ⅱ				
SD60-24015-1	16.50	14.6	Type Ⅰ	SU60-24015-1	8.50	7.5	Type Ⅴ
SD60-24015-2	16.24	14.4	Type Ⅰ				
SD60-24023-1	22.43	19.9	Type Ⅱ	SU60-24023-1	14.33	12.7	Type Ⅳ
SD60-24023-2	22.56	20.0	Type Ⅱ				
SD60-24030-1	32.09	28.4	Type Ⅱ	SU60-24030-1	18.98	16.8	Type Ⅳ
SD60-24030-2	32.63	28.9	Type Ⅱ				
SD60-30018-1	23.26	20.6	Type Ⅰ	SU60-30018-1	14.66	13.0	Type Ⅲ
SD60-30018-2	24.00	21.2	Type Ⅰ				
SD60-30025-1	39.50	35.0	Type Ⅱ	SU60-30025-1	19.00	16.8	Type Ⅳ
* SD60-30025-2	43.69	38.7	Type Ⅰ				
SD60-30030-1	40.15	35.5	Type Ⅱ	SU60-30030-1	49.14	21.8	Type Ⅳ
SD60-30030-2	41.83	37.0	Type Ⅱ				

Note: * Self-drilling screws were applied at every trough.

DISCUSSION OF TEST RESULTS

Results from Figure 2 suggest a good agreement between the theoretical and experimental predictions in deflection at the linear behaviour range. It is worth noting that the theoretical calculations only considered the bending effect. The torsional movement caused by the eccentric loads from the shear centre has been ignored. A constant full cross-section was considered in the calculations for the entire loading regime. This explains the discrepancy between the two sets of results in a high loading range, where purlins started to behave nonlinearly. Nerveless, the close agreement in the linear zone suggests the following four observations: (1) the support connections of purlin do not impose any fixity and should be deemed as a simple support condition; (2) the compression flange is fully restrained by roof sheeting so that any lateral movement of purlin cross-section will not take place; (3) the change in cross-section resulted from any local or distortional buckling is insignificant; and (4) the material is still elastic. Apparently, these findings only hold true for low loading level. As applied loads increased, the load versus deflection curves gradually became nonlinear, which may be due to the joint effect of the above four factors being invalid. Some specimens such as SU60-20025 entered the nonlinear stage at a very low loading level, e.g. less that 20% of the ultimate load. As a result, the simple beam theory considering a full cross-section may lead to an unsafe conclusion in the deflection check for the serviceability limit load.

Current codes of practice, such as AISI[9], BSI[3] and Standard Australia[11], suggest that the serviceability check of the CFS members can be based on a simple beam theory. BSI further recommends that the effective cross-section at an actual stress level should be used allowing for the effect of local and distortional buckling. Two examples of tests in the download loading test were used to calculate the deflection by using this method and results are presented in Figure 3. It can be seen that the BSI recommendation provides a safe and satisfactory prediction. However, as revealed by the present test

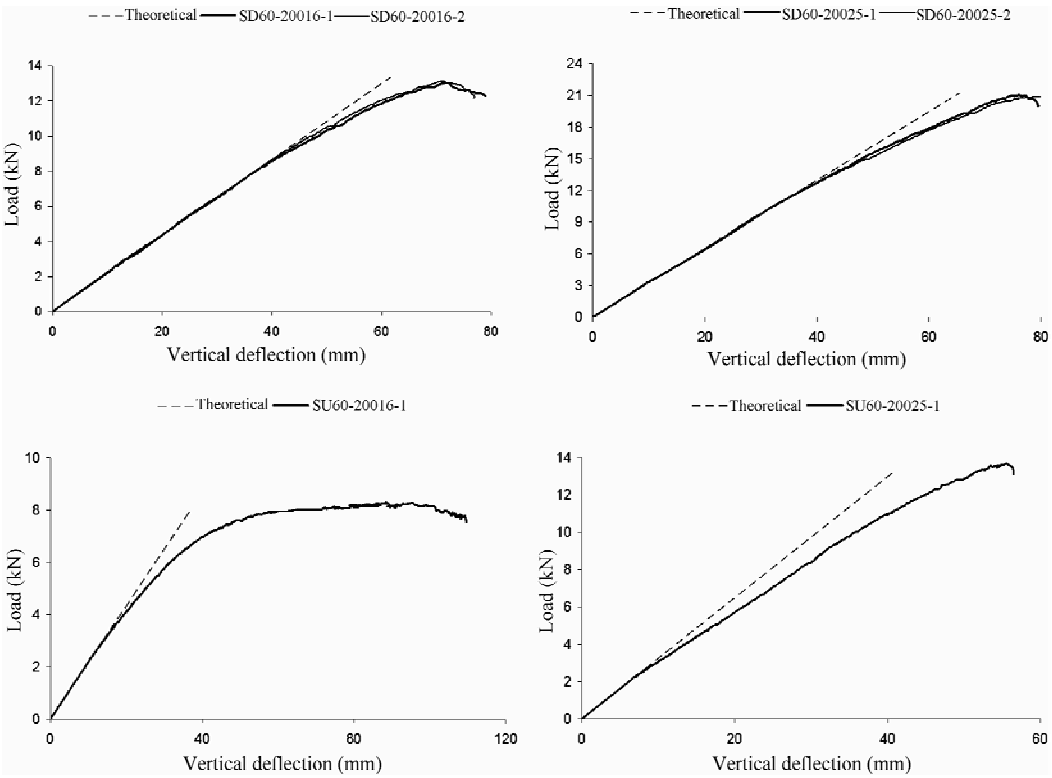

Figure 2 Load versus deflection curves of selected test specimens

results, all the above methods are not applicable for the case of uplift loading.

Failure modes observed in the downward loading tests can be categorized into two types. Figure 4(a) shows type (Ⅰ) failure mode, where a local buckling on the outer web of sigma purlin first appeared at one of the load application points next to the mid-span section. Due to the post-buckling strength of the local buckling mode, the specimen continued carrying loads until distortional buckling occurred at the mid-span point, where the maximum load was reached. The second failure mode is shown in Figure 4(b), where localized failure of sheeting occurred first around the screw connection points. This localized failure was due to a localised couples generated by a tensile force developed in the screw and a reaction along the contact line between the sheeting and one edge of the purlin flange when the purlin section tended to rotate. The localized failure of sheeting did not directly prompt a failure of the purlin specimen. However, it reduced the restraining effect provided by sheeting, encouraged the torsional movement of purlin, and subsequently precipitated the occurrence of failure. In addition, from this type of failure model, significant distortional buckling mode was also observed in the high bending moment zone.

In the uplift loading tests, failures were all caused by the lateral torsional buckling (LTB). A closer examination discovered that the LTB induced failure can be further divided into three categories. Figures 4(c-e) show the types of failure observed in the uplift loading tests. In type Ⅲ failure, one of the purlin experienced a local buckling at the mid-span, which rapidly prompted a LTB failure. It was found that the local buckling always located in the vicinity of the flange and outer web junction, and the unrestrained

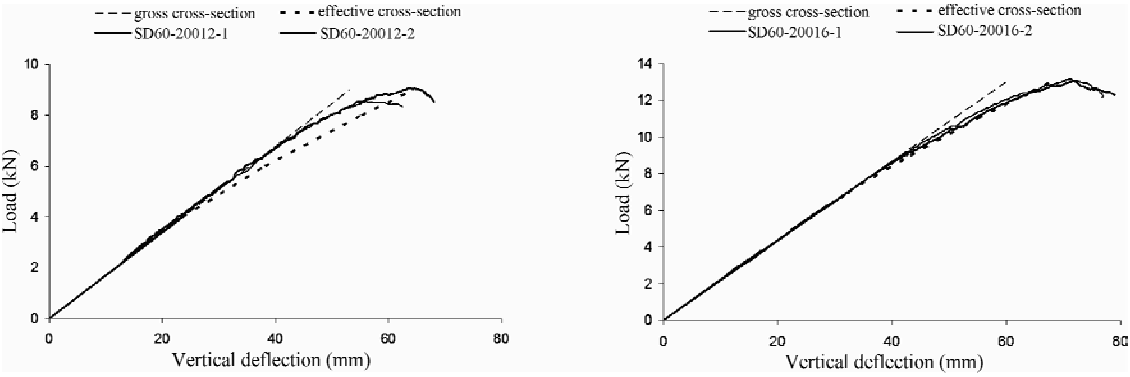

Figure 3 Load versus deflection curves for downward load cases

compression flanges of both purlins moved inwardly when LTB failure occurred as shown in Figure 4(c). In type Ⅳ failure, purlins failed purely because of the LTB, and the unrestrained compression flanges also moved inwardly towards each other (see Figure 4d). In type Ⅴ failure, like type Ⅳ, the sigma purlin failed purely in LTB, but one of the purlins rotated outward in the event of failure (see Figure 4e); moreover, it was noticed that the maximal lateral displacement due to LTB in this type of failure did not occur exactly from the mid-span section, e.g., approximately 200 mm away as shown in Figure 4(e).

(a) Type Ⅰ

(b) Type Ⅱ

(c) Type Ⅲ

(d) Type Ⅳ (e) Type Ⅴ

Figure 4 Typical failure types

CONCLUSIONS

A range of purling-roofing assemblies were subject to both downward and uplift load cases, from which their different behaviours in the flexural stiffness, failure mode and ultimate load were examined. It has been found that the linear beam theory considering a full cross-section only produced satisfactory predictions on the flexural stiffness for the downward load case at a low loading range. Beyond that, purlins would behave in a nonlinear manner mainly because of the occurrence of local and distortional buckling. To address this nonlinearity in the stiffness calculation, varying effective cross-sectional properties with regard to the actual stress level should be employed as suggested by BSI (2006)[3]. For purlins under the uplift load case, the flexural stiffness characteristic was more complex due to the combined action of bending and torsion as well as the occurrence of the lateral torsional buckling. Therefore, a second-order nonlinear analysis considering the effect of roof sheeting should be performed to characterise the flexural stiffness behaviour. It was discovered that the failure modes of sheeted purlins under both loading conditions were highly related to the thickness of the purlins. All test specimens subject to the downward load case exhibited two typical failure modes. Three typical failure modes were observed for the uplift load case, all of which were related to the lateral torsional buckling. It is believed that the eccentric load from the shear centre introduced a torsional moment and it precipitated the occurrence of lateral torsional buckling. Increasing the restraining effect of sheeting such as increasing the screw spacing or the thickness of sheeting will increase the flexural resistance, but a more effective method will be adding anti-sag bars within the purlin span.

REFERENCES

[1] Liu, Q., Yang, J. and Li, L.Y., "Pseudo-plastic moment resistance of continuous beams with cold-formed Sigma sections at internal supports: an experimental study", Engineering Structures, 2011, 33(3), pp.947-957.

[2] Liu, Q., Yang, J., Chan, A.H.C. and Li, L.Y., "Pseudo-plastic moment resistance of continuous beams with cold-formed Sigma sections at internal supports: A numerical study", Thin-Walled Structures, 2011, 49, pp. 1592-1604.

[3] BSI, "Design of steel structures - cold formed structures", BS EN 1993-1-3, 2006.

[4] Moore, D.B. and Sims, P.A.C., "Load tests on full-scale cold formed steel roofs-Part 1: Sigma purlin system; Part 2: Zed purlin system; and Part 3: Zeta purlin system (BRE Report BR124)", Building Research Establishment, 1988.

[5] Willis, C.T. and Wallace, B., "Behaviour of cold-formed steel purlins under gravity loading", Journal of Structural Engineering, 1990, 116 (8), pp.2061 - 2069.

[6] Lucas, R.M., Al-Bermani, F.G.A. and Kitipornchai, S., "Modelling of cold-formed purlin-sheeting systems-

Part 1: Full model", Thin-Walled Structures, 1997, 27(3), pp.223-243.

[7] Lucas, R.M., Al-Bermani, F.G.A. and Kitipornchai, S., "Modelling of cold-formed purlin-sheeting systems-Part 2: Simplified model", Thin-Walled Structures, 1997, 27(4), pp.263-286.

[8] Peköz, T. and Soroushian, P., "Behaviour of C-and Z-purlins under wind uplift", Proceedings of the 6th International Specialty Conference on Cold-formed Steel Structures, St. Louis, MO, USA, 1982, pp.409-429.

[9] AISI, North American Specification for the Design of Cold-Formed Steel Structural Members, AISI S100-2007, 2007.

[10] Johnston, N. and Hancock, G., "Calibration of the AISI R-factor design approach for purlins using Australian test data", Engineering Structures, 1994, 16(5), pp.342-347.

[11] Standard Australia, "Cold-Formed Steel Structures", AS/NZS 4600, 2005, Standards Australia/Standards New Zealand, 2006.